8. FUSION-POWER-CORE ENGINEERING

Clement P. C. Wong
Edward T. Cheng
Steven P. Grotz
Mohammad Z. Hasan
J. Stephen Herring
Tomoaki Kunugi
Rodger C. Martin
Barry W. McQuillan
Farrokh Najmabadi
Elmer E. Reis, Jr.
Dai-Kai Sze
Shiu-Wing Tam
Kenneth R. Schultz
Shahram Sharafat

Contents

8. FUSION-POWER-CORE ENGINEERING

8.1. INTRODUCTION

The ARIES-I design is a conceptual commercial reactor based on modest extrapolation from the present tokamak physics data base. Safety—of the general public, of the operators, and of the investors in a fusion power plant—has been of paramount importance in the ARIES-I design effort. Therefore, in addition to high neutronics and thermal-hydraulic performances, the ARIES-I design team has made low radioactive inventories and the avoidance of toxic materials central to the fusion-power-core design.

During the scoping phase of the ARIES-I study, several different combinations of blanket design options, including choices of coolant, breeder material, structural material, and blanket configuration, were evaluated. These options included: vanadium alloy or SiC composite as the structural material; CO_2 or He at 0.5- to 10-MPa pressure as coolant; and breeder forms of FLiBe molten-salt, gas-carried solid-particulate, or stationary solid breeders. Also considered were different configurations of coolant routing which included forced convective cooling for the FLiBe loop design, and poloidal and radial-plus-toroidal flows for the gas cooled designs. Blanket designs presented in the "Blanket Comparison and Selection Study" (BCSS) [1] and in the TITAN [2] studies were also reviewed. As the blanket evaluation continued, the following four blanket options evolved as potential candidates and were evaluated in more detail:

1. FLiBe loop design with the molten salt, FLiBe, as the coolant and tritium breeder, and V alloy as the structural material [3].

2. Carbon-dioxide (0.5 MPa) and solid-particulate (Li_4SiO_4 or SiC) mixture design carried by the CO_2 gas as the coolant, and Li_4SiO_4 or Li_2O as the solid breeder [4, 5].

3. Helium-cooled (5 MPa) poloidal-flow design with layers of sphere-pac Li_4SiO_4 and Be-metal sphere-pac pellets as, respectively, the stationary solid breeder and neutron multiplier.

4. Helium-cooled (10 MPa) radial-plus-toroidal flow, nested-shell design with a sphere-pac mixture of Li_2ZrO_3 and Be-metal mixture as, respectively, the stationary solid breeder and neutron multiplier.

The FLiBe loop design, shown in Fig. 8.1-1, utilizes forced convective cooling of the first wall. This design was not chosen mainly because of the uncertainty regarding the corrosion behavior between FLiBe and the structural material, the necessary engineering-design complexity for accommodating a high melting-point coolant at 460 °C, and the need for large quantities of Be as part of the constituent of the FLiBe material. The other three options are gas cooled designs, use SiC composite as the structural material, and have the configuration of a poloidal module as shown in Fig 8.1-2.

A limitation of a gas cooled design is that the low-volumetric heat capacity of the gas requires high coolant pressure. When solid particles are mixed into the gas stream, the mixture will have a much higher volumetric heat capacity than pure gas at the same pressure. In comparison, for the same heat-transfer coefficient, the design using a mixture of gas and particulate will need a lower volume flow rate and pumping power than a gas-only design [6, 7]. When a higher density gas like CO_2 is used as the carrier gas, lower coolant pressure (0.5 MPa) can be used while maintaining heat-removal capability similar to that of a higher-pressure (~3 MPa) helium-cooled design.

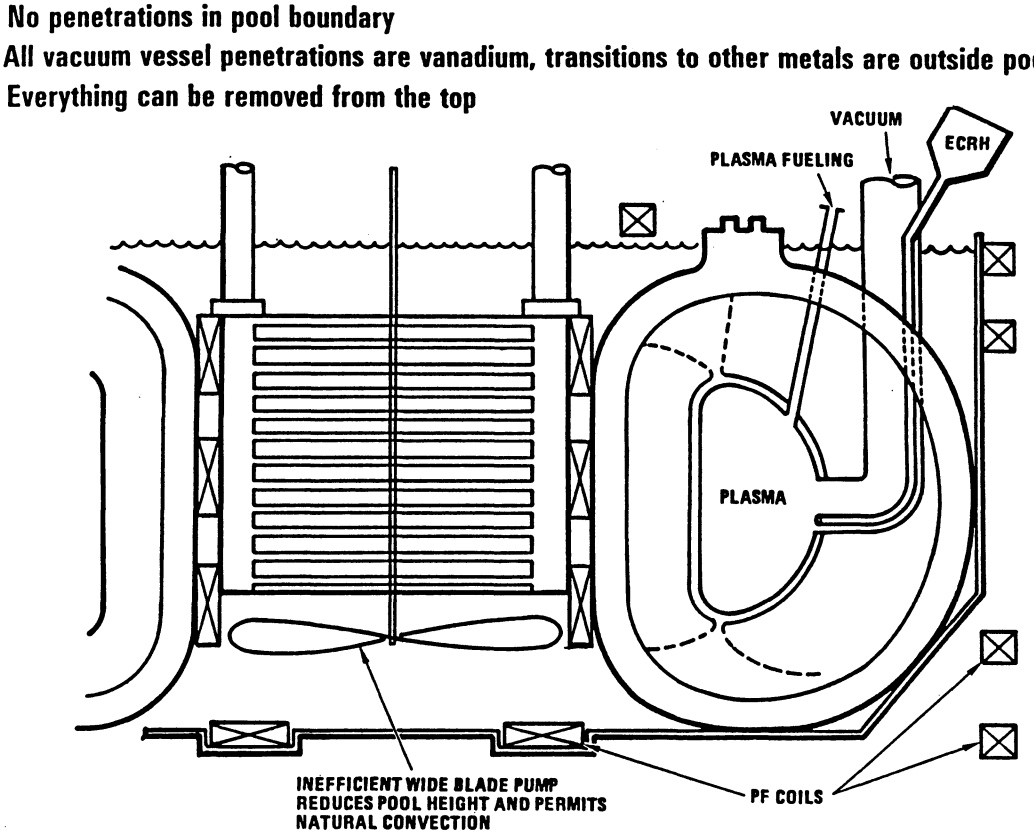

Figure 8.1-1. FLiBe loop design (ASPIRE configuration) [3].

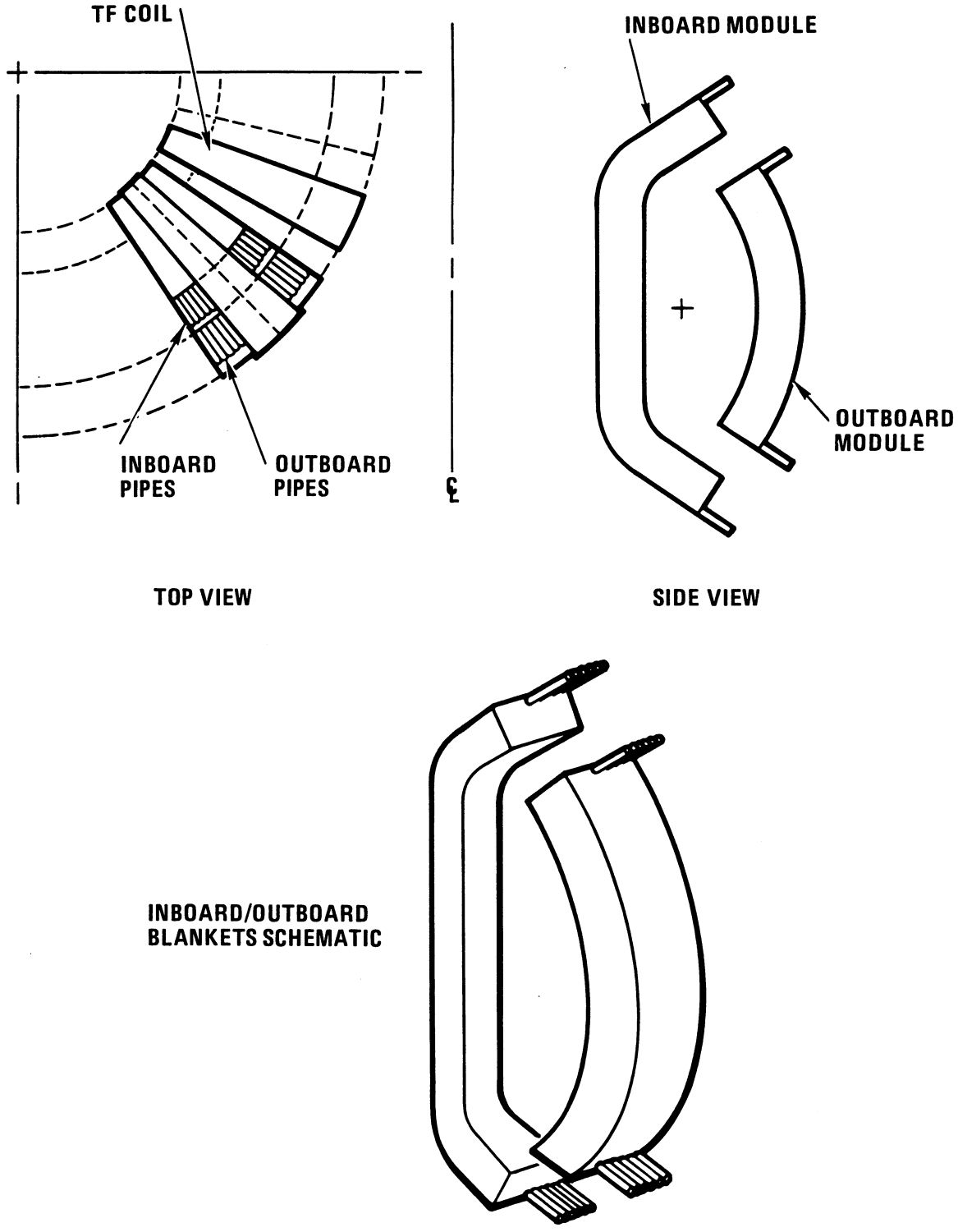

Figure 8.1-2. ARIES-I poloidal module configuration for gas-cooled blanket designs.

For the ARIES-I blanket, designs using Li_4SiO_4 or SiC particulates, both with CO_2 as the carrier gas, were investigated (Fig. 8.1-3). Details of this study are given in Ref. [5]. At a particulate volume fraction of 1.5% and at a CO_2 pressure of 0.5 MPa, adequate control of blanket material temperatures is possible at a very low first-wall and blanket-loop pumping power of a few MW. For fusion reactor application, an additional advantage for using a gas and lithium-compound particulate mixture is that the blanket coolant is also the carrier of the breeder material. This arrangement allows tritium to be extracted outside of the blanket and greatly simplifies the internals of the blanket design when compared to the conventional purge-flow tritium-extraction design [4].

The critical issues for the gas and particulate mixture include: (1) the lack of experimental erosion data for Li_4SiO_4 and for SiC particles on SiC composites, required for evaluating the erosion lifetime of this particulate blanket design; (2) the engineering complexity of designing the circulation system for the gas and particulate mixture; and (3) the possibility of the formation of hot spots if particulates settle in sharp corners and/or in blocked channels. Because of these issues, the low-pressure gas and particulate mixture design was not selected.

Helium gas, because of its chemical inertness and transparency to neutrons, is a natural coolant for fusion reactors [1]. Being a gas, helium has to operate at relatively high pressure to provide good heat transfer and acceptable pumping power. The ARIES team evaluated a 5-MPa helium-cooled pressurized-module design with a poloidal-flow configuration, as shown in Fig. 8.1-4 [4]. In order to optimize the coolant outlet temperature of 650 °C, a re-entrant coolant-flow design was used. This led to high coolant velocities, a high first-wall and blanket pressure drop of 320 kPa, and a correspondingly high blanket-coolant pumping power of 154 MW. Because of the high pressure drop and high pumping power, this concept was not selected.

The reference ARIES-I blanket uses 10-MPa helium as the coolant. A radial-toroidal-flow configuration was chosen over the poloidal-flow design mainly because of the order of magnitude reduction of the blanket-zone pressure drop. The blanket is configured in the form of nested shells (Fig. 8.1-5) because it is perceived to be advantageous to manufacture such a configuration and because of improved reliability. The blanket has a poloidal module geometry in order to match the maintenance scenario of the ARIES-I design. The blanket configuration is segmented toroidally into 32 inboard and 32 outboard poloidal modules, as shown in Fig. 8.1-2. Each poloidal module comprises 17 nested, U-shaped, SiC-composite shells, with a mixture of sphere-pac solid-breeder and Be-metal neutron-multiplier located between the shells (Figs. 8.1-5 and 8.1-6).

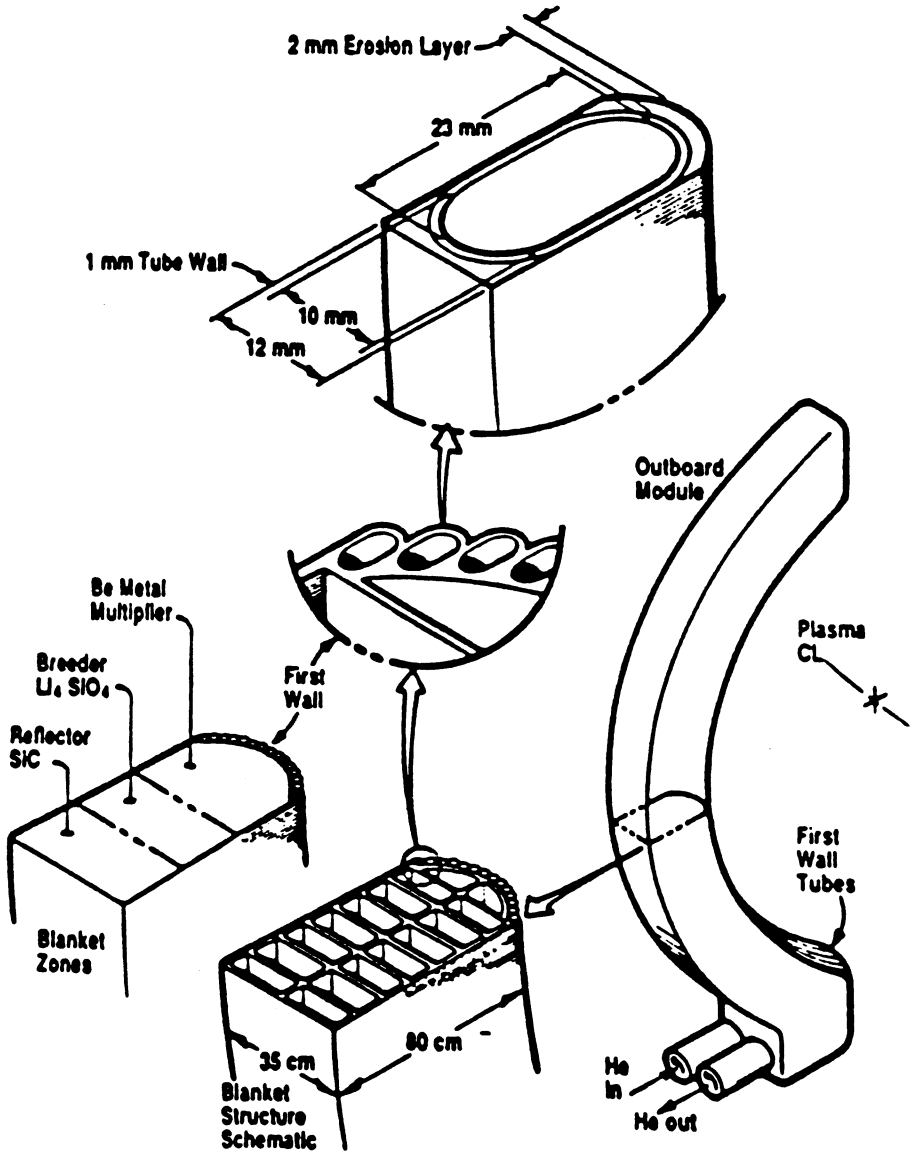

Figure 8.1-3. ARIES-I CO_2-gas and solid-particulate mixture blanket-module design.

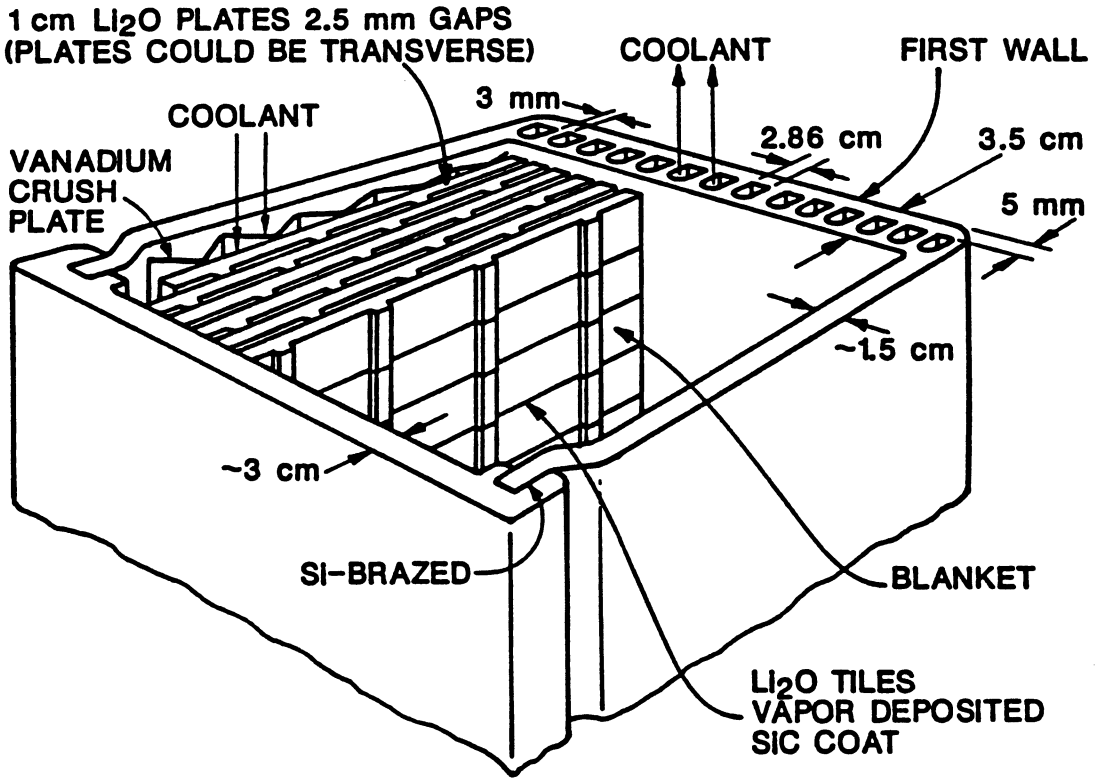

Figure 8.1-4. ARIES-I 5-MPa helium-cooled poloidal-flow blanket-module design.

During the scoping studies of the gas cooled designs, several solid breeders were considered: lithium oxide (Li_2O), lithium orthosilicate (Li_4SiO_4), lithium zirconate (Li_2ZrO_3), and lithium aluminate ($LiA\ell O_2$). Even though Li_4SiO_4 was favored during the scoping phase, it was not selected for the reference design mainly because of the potential concern of irradiation effects. Under neutron irradiation, Li_2SiO_3 will be formed and might result in the formation of a low melting-point eutectic of Li_4SiO_4 and Li_2SiO_3. This potentially can lead to high tritium inventory in the blanket. Also, with the presence of this low melting-point (1024 °C) eutectic, compacting of the breeder particles could occur due to thermal retching, which could limit the lifetime of the blanket. The tritium behavior and material properties of this eutectic are not known at this time, and more experimental results will be needed to address these potential issues.

Lithium zirconate was chosen as the reference solid breeder mainly because of its favorable stability behavior under neutron irradiation [8]. Unfortunately, extensive isotopic tailoring of Zr is needed to reduce activation and afterheat. It should be noted that even after extensive isotopic tailoring, the off-site dose from a severe accident in the ARIES-I reactor is still dominated by Zr. This provides an important incentive to develop low-activation solid breeders such as Li_4SiO_4. Lithium oxide is also a viable

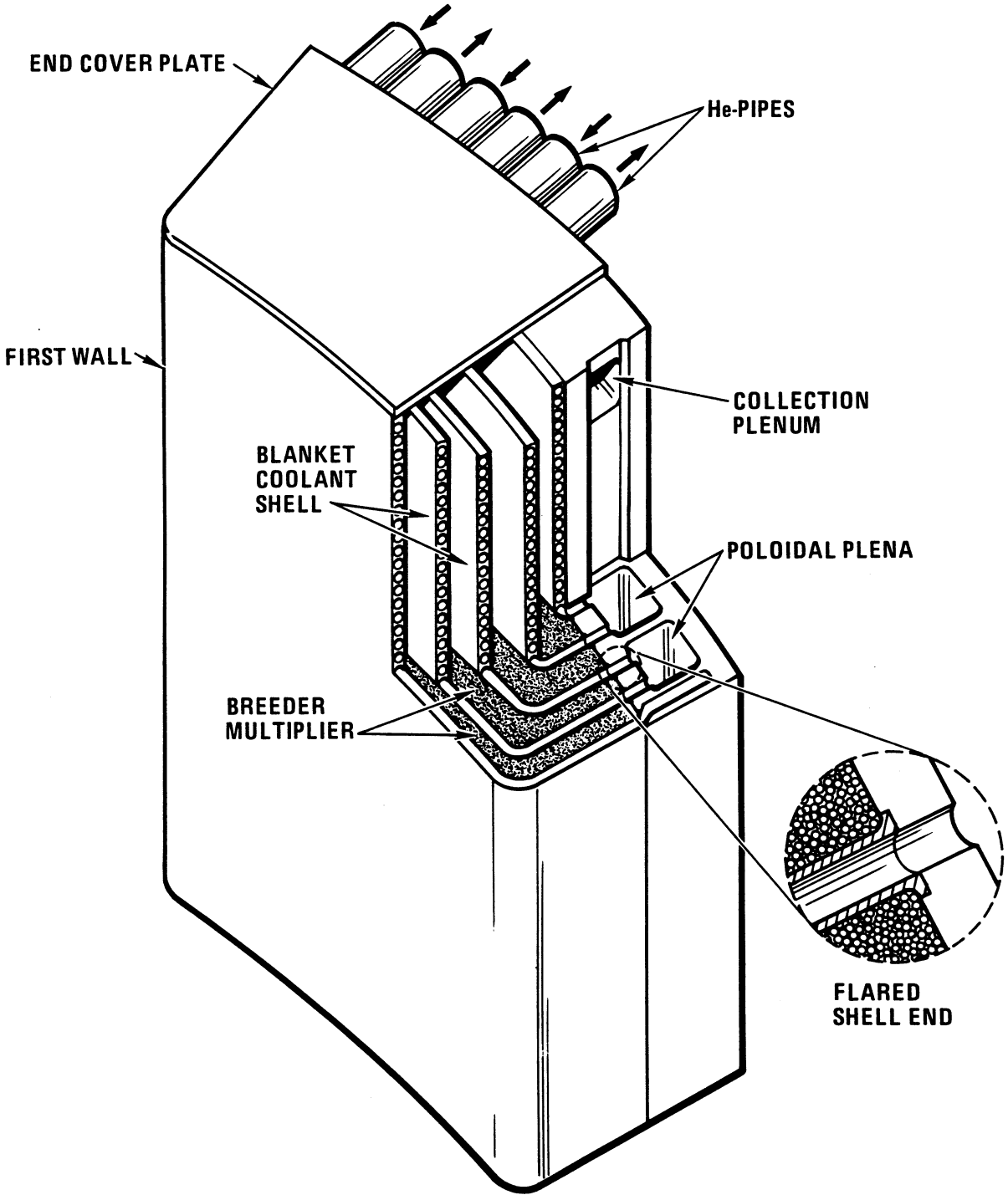

Figure 8.1-5. ARIES-I 10-MPa helium-cooled nested-shell blanket-module design.

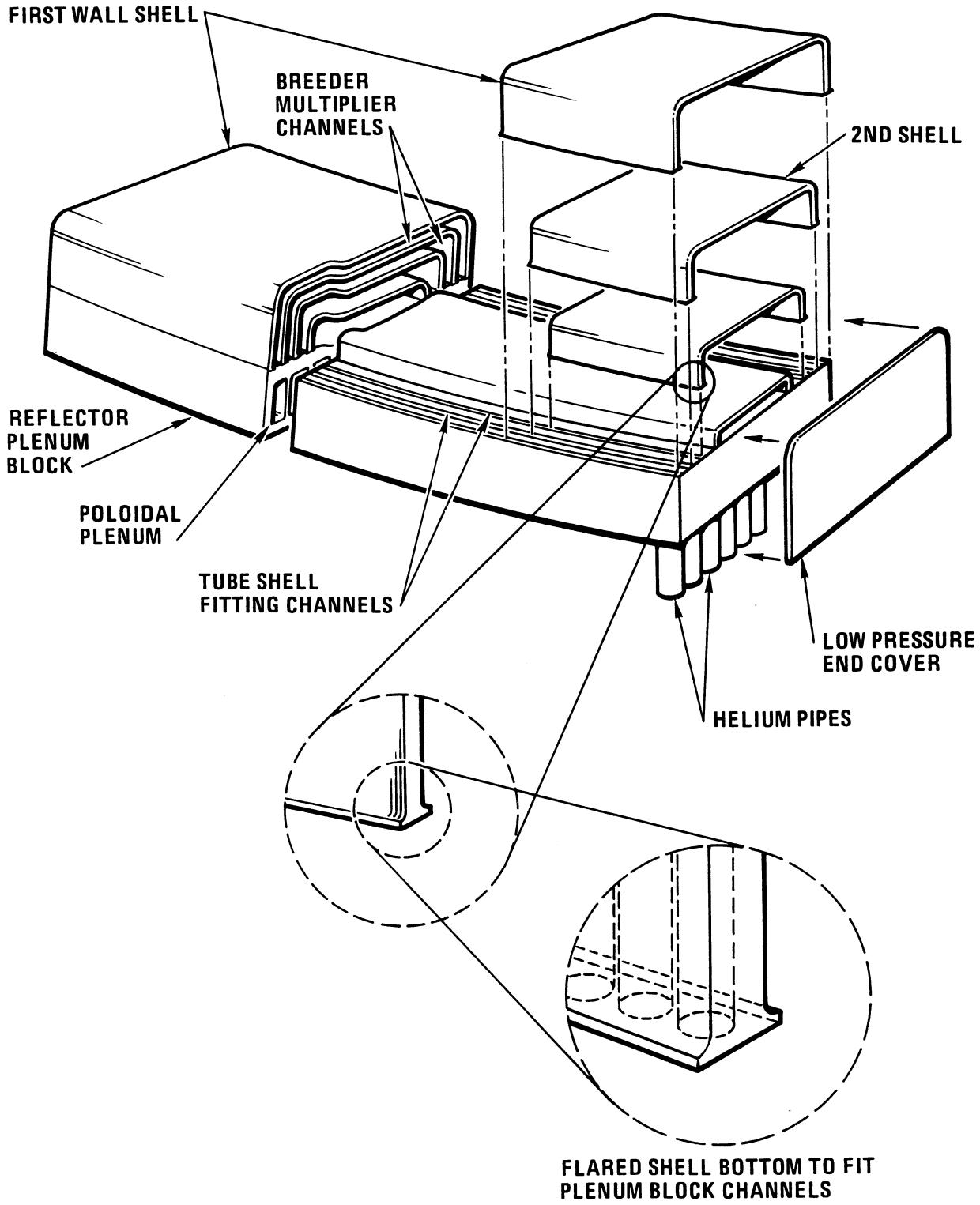

Figure 8.1-6. Assembly procedure for the ARIES-I nested-shell blanket module.

low-activation solid breeder if the generation and migration of LiOT at high temperature ($\sim$1000 °C) can be controlled. Again, this can only be addressed by high-temperature, *in-situ*, tritium-extraction irradiation experiments. In all of the designs considered, including the selected reference nested-shell design, Be neutron-multiplication material will be needed in order to obtain a high blanket-energy multiplication and adequate tritium breeding (it may be possible to achieve an adequate tritium-breeding ratio with Li_2O breeder and SiC structure without any Be multiplier).

The engineering design of the ARIES-I fusion power core has been presented in this section and Table 8.1-I summarizes the ARIES-I reference blanket design. Section 8.2 reviews the material selection process with special emphasis on the ARIES-I SiC-composite structural material. The mechanical design of the fusion power core is given in Sec. 8.3, and the neutronics analysis is presented in Sec. 8.4. Thermal-hydraulic performance of the ARIES-I blanket is reviewed in Sec. 8.5, and the blanket tritium purge-flow design is discussed in Sec. 8.6. Section 8.7 considers heat transfer in plasma-facing components. Summary, conclusions, and critical issues are presented in Sec. 8.8.

8.2. MATERIALS

Silicon-carbide (SiC) ceramic material has been considered previously as candidate structural material for fusion reactors [9]. Silicon carbide has excellent high-temperature capabilities, thermal-shock resistance, chemical stability, and environmental resistance. These characteristics, coupled with very low induced activation and afterheat, make SiC a very promising material for future fusion applications. The ARIES-I reactor uses SiC-fiber-reinforced SiC-matrix composite (hereafter referred to as SiC composite) as the primary structural material. Section 8.2.1 discusses the properties of SiC composite materials. Because of inherent microstructural characteristics, composite materials behave in unexpected and surprising ways when placed in a neutron and ionizing radiation environment. Therefore, the fundamental differences between metals and ceramics are reviewed (Sec. 8.2.1.1). The limited data on the irradiation response of SiC fibers and bulk SiC material are presented, respectively, in Secs. 8.2.1.2 and 8.2.1.3, and are used to estimate the response of SiC composites to irradiation (Sec. 8.2.1.4). These data are then used to estimate the properties of SiC composites operating in the expected conditions of ARIES-I (Sec. 8.2.1.5); a maximum-allowable design-stress criteria has been developed (Sec. 8.2.1.6). Manufacturing techniques for SIC composites are described in Sec. 8.2.1.7 and are used to arrive at a construction scenario for the ARIES-I FPC (Sec. 8.2.1.8). Summary and R&D directions for composites are presented in Sec. 8.2.1.9.

Table 8.1-I.
Summary of the ARIES-I Blanket Design

Material	
Structure material	Silicon-carbide composite
Coolant	Helium at 10 MPa
Breeder/multiplier	Li_2ZrO_3 and Be sphere-pac mixture of 1.0- & 0.1-mm pellets
Configuration	
Structure	17 nested, U-shaped shells form the poloidal modules
Coolant	Poloidal flow in the plena, distributed radially, and cooling the first wall and the blanket toroidally
Breeder/multiplier	Layers of solid-breeder and Be sphere-pac mixture located between the breeder-zone coolant shells
Fabrication	Preformed U-shaped shells to be fitted, one layer after another including internal supports as needed, into the grooves of the reflector/plenum assembly to form the poloidal module; the outer shell is the first wall
Structural analysis	Peak total stress is 77 MPa, well below the 140-MPa design limit
Purge flow design	Areas between coolant shells form the purge channels; helium-purge gas pressure is ~0.4 MPa
Neutronics	Tritium breeding ratio = 1.23 Blanket energy multiplication = 1.30
Thermal hydraulics	Coolant channels embedded in the U-shaped shells; pressure drops and peak material temperatures are acceptable; total first-wall and blanket-loop pumping power is 19 MW; inlet and outlet temperatures are, respectively, 350 and 650 °C
Blanket T inventory	Low, 1 g in the solid breeder, but potentially higher (kg level) in the Be and SiC materials if tritium recoil implantation and retention prove to be a problem

The performance characteristics of the four potential solid-breeder candidates (Li_2O, Li_4SiO_4, Li_2ZrO_3, and $LiA\ell O_2$) under normal (pulsed and steady-state) and off-normal operating conditions were considered (Sec. 8.2.2). The ARIES-I reference breeder material is Li_2ZrO_3 because of its stability under irradiation and temperature and its excellent tritium release characteristics. Unfortunately, Li_2ZrO_3 activation and afterheat are the highest among the four candidates. For the ARIES-I design, extensive isotopic tailoring of Zr has been used to reduce activation and afterheat concerns. Lithium orthosilicate is an attractive, low-activation alternative but chemical stability and tritium inventory of this breeder under high lithium burnup is uncertain. This uncertainty should be resolved by the breeder-material development program.

Beryllium is chosen as the neutron multiplier material for the ARIES-I reactor design mainly because of low activation. It also combines the highest thermal conductivity with the lowest density of all candidate neutron-multiplier materials. Concerns associated with Be are toxicity, resource limitation, and radiation damage. Beryllium properties are discussed in Sec. 8.2.3, with special emphasis on swelling.

Advantages and disadvantages of helium coolant are discussed in Sec. 8.2.4. Material cost estimates for the ARIES-I fusion power core, based on discussions with various SiC-composite manufacturers, are reviewed in Sec. 8.2.5.

8.2.1. Structural Material

Silicon-carbide (SiC) ceramics have been considered previously as candidate structural materials for fusion reactors [9]. Silicon carbide has excellent high-temperature capabilities, thermal-shock resistance, chemical stability, and environmental resistance. These characteristics, coupled with very low induced activation and afterheat, make SiC a very promising material for future fusion-reactor applications. However, monolithic ceramics display two major problems: (1) a high sensitivity to flaws, either internal (generated during processing) or external (occurring during component use); and (2) brittle catastrophic failure. Thus, monolithic ceramics have low toughness and a statistical spread in strength that result in low reliability and, therefore, have limited applications. Nevertheless, favorable physical and chemical properties of SiC have led to large-scale R&D efforts in the U.S. [10] and Japan [11, 12] for aircraft parts (especially the leading edge of wings) and for advanced heat engines, which will require structural reliability at temperatures as high as possible (up to 1500 °C).

The large-scale industrial effort to develop SiC materials is motivated by the two important characteristics of SiC: high resistance to oxidation and excellent thermal-shock

resistance. The resistance to oxidation is due to the surface formation of a self-healing coating of silicon dioxide (silica). Silica coatings, which are effective oxidation barriers, have been suggested for various metallic alloys [13]. Thermal shock resistance is a measure of the ability of a material to withstand sudden thermal-loading stresses. Thermal shock resistance, M, is defined as

$$M = \frac{k\,\sigma\,(1-\nu)}{E\,\alpha}, \tag{8.2-1}$$

where k is the thermal conductivity, σ is the failure strength, ν is the Poisson ratio, E is Young's modulus, and α is the thermal expansion coefficient. Of the candidate carbide ceramic materials (SiC, B_4C, TiC), SiC has the highest thermal-shock resistance ($M = 3471$ W/m for SiC; $M = 2912$ W/m for B_4C; $M = 1551$ W/m for TiC) [14]. Although some nitrides ($A\ell N$, BN, Si_3N_4) have higher thermal-shock resistance than carbides, their applications are limited because of their relatively high equilibrium vapor pressures ($< 10^3$ Pa) as compared with carbides ($< 10^{10}$ Pa). Oxide-based ceramics ($A\ell_2O_3$, BeO, MgO) are generally not considered for structural applications because of their low thermal-shock resistance, which is due to relatively low thermal conductivity and relatively high expansion coefficient of oxides.

Two different approaches are being pursued to enhance toughness and to prevent the catastrophic failure mode of ceramics: (1) developing high-performance monolithic ceramics, and (2) developing reinforced ceramic composites. The first approach concentrates on enhancing the properties of so-called high-performance ceramics by various techniques including: (1) controlling ceramic material purity, (2) developing manufacturing processes aimed at reducing fabrication-induced flaws, (3) minimizing volume changes that occur during manufacturing, (4) developing near net-shape processing techniques, (5) improving sintering aids, and (6) developing transformation and particle-toughened ceramics [12]. Remarkable improvements in ceramic properties have been achieved over the past decade; however, the use of high-performance ceramics is primarily limited to small-size components and slow manufacturing processes.

The second approach used to enhance performance characteristics of ceramics involves reinforcing the ceramic matrix with a second phase material. Reinforcement of ceramics is accomplished with an orderly dispersion of short or continuous fibers in the matrix. Although fibers are generally made from the same material as the matrix, for certain applications different materials are chosen. Strength of ceramic materials is increased by transferring the load from the matrix to the fibers, which takes advantage of their superior tensile strength. Fracture-toughness values for ceramic matrix composites (CMCs) are very high because energy is absorbed as fibers are pulled out of the matrix causing crack

deflection, arrest, or blunting. Figure 8.2-1 compares the typical stress-strain curves for monolithic SiC and unidirectionally reinforced SiC-composite materials. The fracture toughness of a material is directly proportional to the area under the stress-strain curve and it represents the energy required to fracture a material. The figure clearly shows the large improvement in fracture toughness of composites over monolithic SiC. The strain tolerances of SiC composites greatly exceed those of monolithic ceramics. Strain values above 2.5% are routinely measured for such composites [15], whereas monolithic SiC exhibits strain values of less than 0.1% at initiation of fracture (Fig. 8.2-1).

Catastrophic failure of monolithic ceramics is due to rapid and uninhibited propagation of cracks through the ceramic. With proper tailoring of the interface between fibers and matrix, cracks moving through the matrix have to propagate around the fibers. As more stress is applied, more and more macrocracks appear in the matrix until finally the tensile load is applied to the fibers alone. Finally, as stress and strain are increased, the material ultimately fails because of cumulative fiber fracture. By proper microstructural design of ceramic composite materials, an ideal stress-strain curve behavior, *i.e.*, a metal-

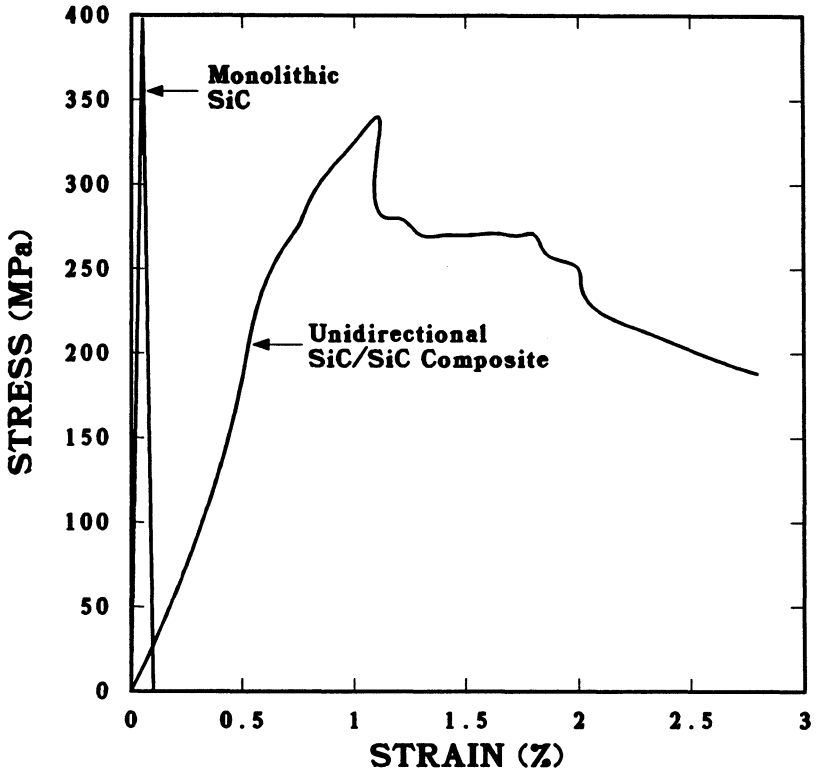

Figure 8.2-1. Stress-strain curve of a 2-D, flat (unidirectional), SiC-fiber-reinforced SiC-matrix composite [15].

like stress-strain behavior, ultimately can be achieved. Such ideal stress-strain curves for SiC composites have been observed by various researchers [15, 16] (see Fig. 8.2-1).

Silicon-carbide fibers are generally used to reinforce SiC matrix ceramics. Silicon-carbide fibers have excellent strength (between 2 and 3 GPa tensile) and provide near perfect material compatability with the host bulk material, *i.e.*, expansion coefficient. Silicon-carbide fibers are stronger than oxide fibers at room temperature and retain more of their strength at high temperatures [17], whereas oxide fibers are stiffer at room temperature but lose their stiffness advantage above about 1100 °C. Silicon-carbon fibers are manufactured by using the chemical-vapor-deposition (CVD) process to deposit SiC onto an ~5-μm-diam substrate filament made of C or W, or by baking a multifilament polycarbosilane (PCS) yarn to form an SiC fiber. The CVD fibers have diameters in the range of 140 μm while PCS fiber diameters are in the 10- to 20-μm range. Both are manufactured as endless fibers.

Table 8.2-I lists some typical properties of SiC fibers. Currently efforts are underway to improve the stochiometry of SiC fibers, *i.e.*, reduce excess oxygen and/or nitrogen found in most commercially available SiC fibers. Rovings, or yarns, of SiC contain about 500 to 1000 fibers. These yarns are used primarily for weaving or braiding composite preforms. The properties of yarn are different from those of individual fibers (Sec. 8.2.1.5).

8.2.1.1. Fundamental differences between metals and ceramics

Bonding. The fundamental difference between metals and ceramics is bonding type. Metallic-type bonds are a result of communal ownership of valence electrons. In ceramics, sharing and/or exchange of electrons occurs chiefly between close neighbors because chemical (ionic or covalent) bonds predominate. The configuration of dissimilar atoms in ionic or covalent bonds dictates and, therefore, affects the stability and properties of ceramics on a localized basis. In metallic alloys, on the other hand, the stability and properties depend in large measure on the average, rather than local, distribution and position of dissimilar atoms (alloying of metals to achieve desired properties is based on this principle). Therefore, while small changes in constituent concentrations of metallic alloys can significantly affect properties throughout the metal, local changes in ceramic constituents are generally reflected in localized property changes. The covalent bond between Si and C, in SiC, is seen to lead to a local order and coordination (on an atomistic level) that are as characteristic of ceramics as the orderly arrangement of atoms throughout the whole crystal is of metallic alloys (microscopic level). This means that the same local order and coordination are often preserved in spite of the various polymorphic and

Table 8.2-I.
Mechanical and Physical Properties of SiC Fibers [18]

Property	PCS SiC[a]	CVD SiC[b]
Diameter (μm)	9 – 15	100 – 140
Length	Endless	Endless
Tensile strength (GPa)	1.9 – 3.0	2.5 – 3.7
Young's modulus (GPa)	180 – 200	380 – 420
Density (10^3 kg/m^3)	2.55 – 2.58	3.4 – 3.5
Thermal expansion coefficient (10^{-6} K^{-1})	3.1	4.2 – 4.5

[a]Polycarbosilane-derived fibers.

[b]Chemical vapor deposition of fibers.

polyphase transformations that ceramics undergo during processing. (Polymorphism is when a material occurs in different forms, such as carbon existing with crystal structures of graphite or diamond.) Past and present uses of ceramics are largely dependent on this local invariance.

Contrary to metals, ceramics consist of two or more anion and cation lattices embedded into each other (SiC, BN, TiC, WC, $A\ell_2O_3$, $MgA\ell_2O_4$, $Y_3A\ell_5O_{12}$). The existence of multiple lattices, coupled with a high degree of directionality in ceramic crystals, will significantly affect the response of ceramics to neutron irradiation. For example, to form a complete and stable SiC vacancy, both a silicon atom and a neighboring carbon atom have to be displaced permanently from their positions. As a result, radiation damage in ceramics will lead to a non-stoichiometric ratio of displacements (atomic masses and displacement energies are different for each chemical species constituent). In addition, the multiple anion and cation lattices will affect the various charge states in which different point defects can exist. Because of these fundamental differences between metals and ceramics, neutron irradiation of ceramics generally results in the formation of higher numbers of unstable defects than in metals. Thus, ceramics may have a higher tolerance to displacive radiation than metals have. In this section, ceramic irradiation data that

validate this point to some extent are reviewed. However, far more research is needed to understand many of the unknown fundamental phenomena of ceramic response to irradiation.

Fracture mechanisms. Metals also differ from ceramics in that they are capable of plastic deformation resulting in ductile fracture (*i.e.*, significant deformation before failure). Ductile fracture is associated with plastic behavior of metals. Plastic deformation consists of a slip, or glide, of one part of the body over the other and is mostly determined by the nature and stability of the crystal structure. At the onset of plastic deformation, a single metal crystal, subjected to axial pull, splits into several parts which glide over each other. In covalent or ionic bonded crystals, the initial splitting of the crystal requires more energy and, thus, crack initiation in ceramics requires more energy than in metals. However, crack propagation is more difficult in metallic solids than in ceramics because of the energy absorbed during plastic deformation around the crack tip in metals.

Ceramics are subject to brittle failure (*i.e.*, elastic deformation up to the breaking point). The inability to plastically deform (*i.e.*, breakup of the crystal followed by sliding) is the primary characteristic of the brittle response of ceramics. In ceramics, it is the presence of cracks having sizes larger than a critical value that results in uninhibited crack propagation (catastrophic failure). In all circumstances it is the largest crack that constitutes the weakest link in brittle fracture and the crack concentration per unit volume is rather immaterial. Statistically, there is a greater probability of finding large cracks in a large body than in a small one. Therefore, as a rule, large samples of bulk brittle material fracture at a lower stress than small ones. It should be noted that the primary advantage of composites over bulk ceramics lies in the ability to obstruct matric crack propagation. The fracture toughness of composites does not rely on the toughness of the matrix but on the interaction of matrix cracks with the fibers, or any other reinforcing network.

8.2.1.2. Irradiation effects on bulk ceramics

Solids exposed to neutron irradiation will undergo displacement damage, the effect of which is defect generation (*e.g.*, dislocations, vacancies, depleted zones, voids, transmutation products, formation of precipitates, and bubbles). Since the properties of metals depend mostly on the average distribution of atoms, relatively small changes in constituent concentrations can have significant effects on the overall mechanical properties

of the alloy. Thus, a small percentage of "burnup" can have drastic effects on global properties. In ceramics, however, burnup will primarily affect mechanical properties more on a local scale. Therefore, ceramics should in general be more tolerant than metals to burnup.

The effect of defect formation on mechanical properties is due primarily to an increase in the population of slip and glide barriers, resulting in irradiation hardening of the material. The yield and tensile strength of the exposed material increases, while the ductility decreases. In metals, the primary cause of irradiation hardening is due to the formation of obstacles to slip bands. In ceramics, it is believed that defect formation slows crack propagation. Significant losses in metal ductility may occur because of neutron exposure, while ceramics, not being ductile to begin with, mostly exhibit some increase in strength as a result of displacement damage.

In examining the effects of elevated-temperature neutron irradiation on fracture toughness of ceramics, Clinard *et al.* [19] made measurements on spinel ($MgA\ell_2O_4$), $Y_3A\ell_5O_{12}$, and $A\ell_2O_3$ crystals exposed to neutron fluences of $1 - 2 \times 10^{26}$ n/m^2 at 925 and 1100 K (this fluence was estimated to be equivalent to a full power year of exposure at the first wall of a 2-MW/m^2 fusion reactor). A slight increase in toughness of $MgA\ell_2O_4$ was observed and attributed to interaction of cracks with strain fields around dislocation loops. No significant change was noted for $Y_3A\ell_5O_{12}$, despite the presence of a high concentration of unresolved defect clusters. Fracture toughness of $A\ell_2O_3$ was markedly increased, with the enhancement apparently attributable in large part to impedance of crack propagation by interaction with the irradiation-induced void lattice. Irradiation hardening of $A\ell_2O_3$ was on the order of 2.1 times that of unirradiated sample strengths. The irradiation-induced toughening of spinel resembled the increased toughening of coherent-precipitate-strengthened spinel [20] and of dispersed phase-toughened glass. In all cases, the damage microstructure was characterized by a high concentration of aligned small voids [19]. Crack morphology clearly demonstrated that before irradiation, the cracks were featureless and straight; whereas in the irradiated material, cracks underwent void intersection, changes in direction, jogging, and branching. In studies of crack/pore interaction in glass, attraction of cracks to pores, crack impedance, segmentation, and change are the fundamental processes that cause toughening of glasses [21]. In summary, several possible mechanisms have been proposed to explain toughening of ceramics: void-arrested-crack mechanism [22], crack deflection mechanism [23, 24], and a mechanism associated with the mismatch of expansion coefficients or elastic modulus with second phase particles [25, 26]. Neutron irradiation can induce a combination of these toughening mechanisms in ceramic materials.

Impact of manufacturing process. Certain ceramic manufacturing techniques use sintering aides that remain as second phase solutes in the matrix. Since the existence of finely dispersed solutes clearly affects the microstructural response, the effects of irradiation on SiC may vary substantially depending on which SiC ceramic is used. Therefore, the interpretation of data from SiC irradiation studies must take into account the manufacturing process and the selected sintering aids.

The effects of neutron irradiation on several differently prepared SiC materials have been reported [27–32]. Mechanical properties such as flexural strength and Young's modulus of single-phase pyrolytic SiC were not significantly changed after exposure to a neutron fluence of 1.2×10^{26} n/m^2 and irradiation temperatures of 1020 °C [27, 28]. However, reaction-bonded SiC shows about a 50% reduction in fracture strength after exposure to 10 to 30×10^{24} n/m^2 at 450 and 650 °C. The strength of reaction-bonded SiC initially drops rapidly when first exposed to neutron irradiation, after which the loss of strength levels off and even recovers slightly when the fluence reaches 6×10^{25} n/m^2. A similar drop followed by recovery was also measured for the Young's modulus [28, 29]. Self-bonded SiC shows a 25% decrease in fracture strength when irradiated to 2×10^{24} n/m^2 at temperatures below 400 °C, while at 1200 °C the decrease is only about 10% [30]. The strength distribution of CVD high-density β-SiC was virtually unchanged by irradiation at between 540 and 740 °C after exposure to about 2×10^{26} n/m^2 [33]. In comparison, sintered SiC showed a reduction of 34% in mean strength, and reaction-bonded SiC suffered a 58% reduction.

More recently, the effects of three different sintering aids on mechanical properties of neutron-irradiated SiC was investigated [32]: reaction-bonded SiC containing about 9% free Si; pressureless-sintered SiC with about 1% each B and C; and hot-pressed SiC having about 1% BeO. Irradiation temperatures were between 280 and 600 °C and the maximum fluence was about 6×10^{24} n/m^2. Regardless of SiC type, the amount of increase in length of the irradiated samples decreased as the irradiation temperatures increased. Annealing of all irradiated samples to temperatures as high as 1000 °C showed drastic reductions of the neutron-irradiation-induced length changes. Regardless of the amount and kind of sintering aid used, the temperature at which annealing-induced length reduction begins is the same. This indicates clearly, as pointed out in earlier years by Matthews [29], that the dimensional changes in neutron-irradiated SiC are primarily due to interstitial vacancy interaction and not the presence of helium. Boron, C, and BeO generate far more helium in the irradiated samples than is generated in SiC that contains excess Si. If helium bubbles had formed, they would have drastically affected the annealing temperature limits for recovery of neutron-induced length changes. Of the

three samples, only the BeO-containing SiC showed a 10% increase in strength, while the other two samples suffered decreases. Helium transmutation production in SiC is discussed in more detail later.

Dimensional changes. It is well-known that the swelling of SiC saturates at fluences of about 2×10^{24} n/m^2 and that it depends on the irradiation temperature up to about 1000 °C [34, 35]. Consistent with earlier reported data [36], Price [27] showed that radiation-induced expansion of SiC saturates and becomes independent of exposure after about $1 - 3 \times 10^{24}$ n/m^2 for temperatures below 1000 °C. Both of these findings, the saturation of expansion and the decrease in expansion with rising irradiation temperature, are typical of other isotropic or near-isotropic ceramic materials such as BeO, $A\ell_2O_3$, and MgO [37]. Irradiation of SiC at temperatures above about 1250 °C resulted in void formation and did not saturate up to a fluence of 1×10^{26} n/m^2 [27, 38]. Production of thermal vacancies has been suggested as the primary mechanism for the increase in swelling above 1250 °C [39].

Behavior of helium in SiC. The primary effect of helium generation is the formation of helium-filled bubbles inside the matrix material. In metals this leads to a drastic reduction of ductility known as helium embrittlement. Because boron was used extensively as a sintering aid in manufacturing reaction-sintered SiC and because boron has a high (n,α) cross section, some data on the effects of transmutated helium on the microstructure of neutron-irradiated SiC is available [31,32,39-42]. However, the amount of helium generation was not measured directly in any of the studies. There is no evidence of voids or helium bubbles in any of these experiments, even after helium-ion irradiation at 1000 °C with 30-keV He-ion beams [43]. Only after heat treating the irradiated samples to well above 1500 °C does the formation of voids and/or bubbles becomes apparent. The absence of helium bubbles at lower irradiation temperatures (< 1000 °C) has been attributed to the presence of neutron-irradiation-created helium sinks inside SiC [41] and lack of mobility of vacancies at low temperatures [41]. The helium sinks were identified as dislocation loops, which do not anneal even at temperatures that melt one of the bonding phases [41]. A stable neutron-irradiation-induced dislocation network most likely causes the absence of voids and/or helium-filled bubbles at temperatures below about 1000 °C.

A study aimed at understanding the effects of helium transmutation products in SiC was conducted by Hojou [43]. Electron microscopic observations were performed on defect structures in polycrystalline SiC irradiated to 300 and 1000 K with 30-keV He ions to fluences from 10^{18} to 10^{21} ions/m^2 (which corresponds to $\sim$0.14 to 14 dpa). At low

temperatures, aligned planar defects (not voids or bubbles) were observed, and above 1 dpa, damage amorphatized regions were detected. At 1000 K irradiation temperature, no amorphatization was seen; however, extensive recrystallization was observed. It is speculated that at high damage doses and elevated temperatures, the amorphous structure first forms but is consequently annealed out through the rearrangement of atoms by thermal agitation. This may have been the cause for the formation of recrystallized regions which tend to be relatively crack free. This would mean that a certain level of reconstruction of damaged zones can be anticipated. In particular, several SiC neutron-irradiation experiments [28, 29, 40] indicate various degrees of recrystallization (self-healing).

As pointed out, boron is used frequently as a sintering aid during the manufacture of SiC. Boron has a high helium-generation cross section and, therefore, is used to simulate anticipated helium-generation rates at low neutron fluences. However, the major drawback of B doping is that B tends to cluster (*i.e.*, segregate at or near the grain boundaries [42]), which can have a major effect on mechanical properties of SiC. Boron clustering causes misfit strains between SiC and B [29, 32] and results in the formation of microcracks at grain boundaries. Therefore, caution must be exercised in future experiments that utilize high B concentrations in SiC.

High helium-generation rates. High helium-generation rates in a fusion-reactor SiC-composite first wall (about 2000 appm per MWy/m^2-neutron wall loading) will cause the formation of helium bubbles even at low irradiation temperatures ($< 1000\,^\circ$C). The following is a discussion of the anticipated behavior of helium in SiC and the effects of possible helium bubbles on SiC properties. Because the large (n,α) cross section of B could initiate the formation of helium bubbles at relatively low fluences, results from boron carbide (B_4C) experiments are drawn upon. One study of helium bubble formation in B_4C [44] substantiates some of these claims. After the transmutation to about 1.6 at. % helium content (irradiation temperature at 800 °C), the following general conclusions were drawn [44] :

1. Point defects did not agglomerate in clusters but are accepted in large numbers and in stable form in the structure.

2. Helium agglomerates in a plate-like geometry (unlike metals where mostly spherical bubbles form).

3. The plate-like helium-filled geometries are the only visible form of irradiation-induced damage.

4. Alignment of these helium plates along strings, coupled with strong strain fields around the plates, generated transgranular microcracking (crack/pore interaction; note that microcracking of ceramics does not necessarily constitute failure).

5. Intergranular microcracking occurred although no helium was found between grain boundaries.

6. Point defects, when present at sufficient concentrations, can interact with and cause stress relaxation around the helium plates.

Although not fully conclusive, the above results clearly indicate two points: (1) ceramic materials may be more radiation-damage resistant than metals, and (2) the creation of helium-filled plates (the number density of which saturates at a specific material and temperature-dependant value) can result in an increased fracture toughness of ceramics. The possibility of developing ceramic materials that are highly resistant to radiation damage was demonstrated by Parker *et al.* [45]. Polycrystalline aluminum oxynitride (ALON) spinel, $A\ell N(A\ell_2O_3)_2$, was irradiated with 0.8- and 1-MeV electrons in a high-voltage electron microscope over a temperature range of 300 to 1100 K for up to 2 hours. No defect aggregation was observed at any temperature, through either thick or thin sections. The lack of any dislocation loops was attributed to the existence of a high density of recombination centers. No one has ever reported dislocations in ALON [45]. However, the investigation of irradiation effects combined with high helium generation is an essential R&D requirement for developing ceramic materials for fusion applications, particularly since most of the available data has been accumulated from "off-the-shelf" ceramic materials. Because no special tailoring of ceramics for fusion applications has been done, comparing the irradiation response of today's ceramic materials to those of metallic alloys can be misleading. It is important to remember that many of the favorable characteristics of today's nuclear metallic alloys were developed over several decades of relatively intense R&D efforts.

8.2.1.3. Irradiation effects on SiC fibers

Although effects of high-fluence neutron irradiation on bulk SiC have been reported, only low-fluence neutron-irradiation experiments on SiC fibers have been made [47]. Two types of SiC fibers were irradiated at temperatures below 300 °C to fluences of 2×10^{23} n/m^2 with $E > 1$ MeV in JMTR and 7×10^{21} n/m^2 with $E = 14$ MeV in RTNS-II. The SiC fibers differed only in their heat treatment prior to irradiation. The fibers

were obtained by heating polycarbosilane precursor fibers at 1000 and 1300 °C forming, respectively, amorphous and microcrystalline β-SiC fibers. Tensile strength and X-ray radial-distribution analyses were made on the SiC fibers to determine the neutron irradiation effects. Radial distribution functions of unirradiated and RTNS-II-irradiated SiC fibers were nearly the same, while those irradiated by JMTR differed only slightly from unirradiated ones. The tensile strengths and Young's moduli of both amorphous and microcrystalline fibers were not changed when irradiated with 14-MeV neutrons in RTNS-II. However, the two fibers behaved differently when exposed to the fast neutron spectrum of JMTR. The mechanical properties of the amorphous fibers were hardly affected, except for a rise in the tensile strength at the highest fluence. The tensile strength and Young's modulus of the microcrystalline fibers tend to increase with neutron fluence. Scanning-electron-microscopic investigations showed no change in the surface morphology. In addition, fibers irradiated in air did not show any indication of radiation-enhanced oxidation, a phenomena thought to be responsible for loss of strength in various air-irradiated carbon fibers.

Measurements of properties of irradiated SiC fibers after removal from SiC-fiber/Aℓ-matrix composites have also been reported [46]. The fibers were exposed to 1×10^{25} n/m^2 fluence of fast neutrons at 723 K. The average tensile strength of the fibers increased from $\sim$2.1 to $\sim$3.9 GPa. Exposure to a mixed-neutron-energy spectrum increased the ductility of fibers by about 30%, while fast-neutron-exposed fibers showed a small ductility decrease. The Young's modulus of the mixed-spectrum-exposed fibers changed little but that of the fast-neutron-exposed fibers increased by about 31%. The authors concluded that the SiC fibers showed excellent stability under neutron irradiation.

Although the neutron-irradiation data base is extremely small, SiC fibers do not show any inherent or drastically adverse response to neutron-irradiation damage.

8.2.1.4. Irradiation effects on ceramic matrix composites

It is important to state that the primary advantage of ceramic-matrix composite (CMC) materials over bulk ceramics lies in the ability to obstruct matrix crack propagation. The fracture toughness of CMCs does not rely on the toughness of the matrix but on the interaction of matrix cracks with fibers, or any other reinforcing network. The effect of possible microcracking of the matrix due to formation of helium-filled plates or bubbles does not constitute failure of CMCs. Note, for example, that the graphite matrix of high-strength C/C composites is for the most part entirely microcracked. Matrix microcracking is caused by large residual stresses generated during the cool-down phase of

manufacturing. Thus, even though the matrix is microcracked, the C/C composites exhibit strength and fracture toughness far superior to those of SiC composites (the matrix of SiC composites is not entirely microcracked but contains about 5% to 10% porosity).

In summary, the response of CMCs such as SiC composites to neutron irradiation is not known at present. Based on a limited number of neutron irradiation experiments on bulk SiC and on SiC fibers, the following observations can be made:

- The presence of a second lattice, and the additional stoichiometric point-defect constraints, distinguish the radiation-damage response of ceramics from that of metals. Both the lattice and stoichiometry effects are likely to mitigate radiation damage in ceramics.
- Dimensional changes in SiC saturate around 3×10^{24} n/m^2 for irradiation temperatures below 1200 °C.
- Voids and helium bubbles have not been reported in neutron-irradiated SiC for temperatures below 1200 °C.
- Irradiation-produced dislocations inside the SiC matrix seem to be the primary trap sites for other irradiation-produced defects (including helium atoms), thus formation of voids or bubbles is impeded.
- Silicon carbide will probably withstand a much higher burnup than metallic alloys because of the polycrystalline nature of ceramics.
- In the event that high helium-generation rates lead to the formation of helium-filled bubbles, these bubbles will have a pronounced effect on crack behavior. Crack/pore interactions in glasses and other ceramics have been shown to increase the fracture toughness of these materials.
- Amorphatization followed by a rearrangement of atoms at high irradiation temperatures (900 °C) can cause recrystallization. Recrystallization generally causes loss of strength in metallic alloys but "heals" cracks in ceramics, which enhances strength.
- SiC fibers have shown irradiation-hardening behavior when exposed to a mixed-neutron-energy spectrum, while low-fluence 14-MeV exposure has not produced any measurable changes in mechanical properties.

- The fundamental characteristic of CMCs is the interaction of matrix cracks with the reinforcement network. Furthermore, radiation damage effects of ceramics have shown low-fluence saturation levels that are dependent on ceramic type and temperature. Therefore, radiation damage in CMC materials is not expected to drastically affect the mechanical properties. It is believed that, following radiation damage, a certain degree of fracture toughness improvement can be expected in CMCs.

These observations indicate that it is not unreasonable to postulate that CMCs might out-perform metallic alloys when it comes to fundamental radiation-damage effects. However, bulk-ceramic-material test results do not fully describe the response of mechanical properties of CMC materials to neutron irradiation. Therefore, it is obvious that neutron irradiation experiments on SiC composites (and other CMCs) are necessary in order to understand the response of this material to neutron irradiation.

Lifetime of SiC composites Based on the above discussion, it is argued that SiC composites may be able to withstand a damage dosage well above the tolerable levels of metallic alloys. However, the ARIES-I team has opted to use the same approximate lifetime criterion as is commonly suggested for metallic alloys, namely about 200 dpa. No experimental data exist for the displacement-damage threshold energy of neutrons in SiC. Estimated correlations between neutron fluences and dpa have been reported [41]. A fluence of 1×10^{26} n/m^2 with neutron energies above 1 MeV results in approximately 2.6 dpa, while at energies of 0.18 MeV, fluences of 7.3 to 8.1×10^{26} n/m^2 result in 17 to 20 dpa in SiC. The SiC displacement-damage energy was calculated to be 25 eV [48]. Based on this displacement damage energy, a dpa rate of 11 per MWy/m^2 was calculated for an SiC-composite first wall, resulting in a lifetime of about 18 MWy/m^2.

8.2.1.5. Properties

Ceramic composite materials are still in their developmental infancy (5 to 10 years) and, consequently, thermomechanical data are still limited. Typical thermomechanical properties of 2-D, flat, SiC composite are given in Tables 8.2-II and 8.2-III. Silicon-carbide composite materials exhibit good mechanical strength at the high temperatures (>1000 °C) associated with a high strain-to-failure value. These composites are resistant to high-temperature thermal shock and thermal cycling. They need very high energies for crack propagation, with increasing values when damaged regions extend. Thus, SiC composites are potentially damage-tolerant ceramics that do not suffer from catastrophic failure behavior.

Table 8.2-II.
Laminated SiC-Composite Properties[a]

Property	Temperature (°C)		
	23	1,000	1,400
Fiber content	40%	40%	40%
Specific gravity	2.5	2.5	2.5
Porosity	10%	10%	41%
Tensile strength (MPa)	200	200	150
Elongation, tensile	0.3%	0.4%	0.5%
Young's modulus, tensile (GPa)	230	200	170
Poisson's ratio			
V12	0.05	NA	NA
V13	0.18	NA	NA
Flexural strength (MPa)	300	400	280
Compressive strength (MPa)			
In plane	580	480	300
Through the thickness	420	380	250
Interlaminar shear strength (MPa)	40	35	25
Thermal expansion coefficient (10^{-6}/K)			
In plane	3.0	3.0	NA
Through the thickness	1.7	3.4	NA
Thermal conductivity (W/K-m)			
In plane	19	15.2	NA
Through the thickness	9.5	5.7	NA
Fracture toughness (MPa-$m^{1/2}$)	30	30	30
Specific heat (J/K-kg)	650	1,200	NA
Total emissivity	0.8	0.8	0.8

[a]SiC composite laminates made with 0/90 balanced NICALON fabric; coupons were tested both in atmosphere and in air for short exposure time [49].

Table 8.2-III.
Two-Dimensional, Flat, SiC-Composite Properties [16]

Density (kg/m^3)	2,400
Tensile strength (MPa)	250
Strain at failure (%)	8
Bending strength (MPa)	
27 °C	320
500 °C	350
1000 °C	380
Thermal conductivity (W/K-m)	
27 °C	25
500 °C	19
1000 °C	18
Fracture toughness ($MPa\text{-}m^{1/2}$)	
27 °C	26
500 °C	27
1000 °C	27
Thermal shock resistance[a] (MPa)	
27 °C	320
500 °C	300
1000 °C	280

[a]Sample is heated to indicated temperature then dropped into cold water; the remaining bending strength is measured at room temperature.

Most 3-D, reinforced SiC composites are either products of classified developments or are proprietary of an industry. Therefore, because of the lack of public data, thermomechanical properties of these composites have to be estimated using micromechanical design equations. These equations are based primarily on the rule of mixtures. The input to the equations consists of constituent material (*i.e.*, matrix and fiber) properties. A unified set of composite micromechanical equations of simple form is now available [50]. These equations can be used to predict tensile, compressive, and flexural strength, and impact resistance, fracture toughness, and thermal properties.

Mechanical properties. The composites industry has developed numerical codes to estimate thermomechanical properties of composites as functions of composite characteristics (*i.e.*, fiber volume fraction, matrix void fraction, and fiber orientation). The code, CLASS, used for ARIES-I was developed by Materials Sciences Corp. [51]. To avoid an overestimation of SiC composite properties, the constituent (*i.e.*, fiber and matrix) properties were chosen very conservatively. Furthermore, no allowance was made for probable future improvements in matrix densities above 90%. Also, to reflect the effects of neutron irradiation, fiber and matrix neutron-irradiation data were reviewed and used.

Neutron irradiation effects on the strength of SiC matrix were incorporated by using the truncated and irradiated Weibull distribution function for the tensile strength of CVD SiC with a near-zero probability of failure [33]. Samples of CVD SiC were first proof-tested and then irradiated up to 10^{26} n/m^2 with fast neutrons ($E_n > 0.1$ MeV). This fluence corresponds to about 21 dpa [41, 52]. Some samples showed close to 700-MPa flexural strength but had a high failure probability. Samples with an average flexural strength of about 435 MPa were shown to have a near 100% survival probability. Noting that at 1000 °C many of the irradiation-induced dimensional changes in SiC saturate at low fluences of ~0.2 dpa [53, 54] and estimating the tensile strength to be ~80% of the flexural strength value, a tensile strength of about 350 MPa is chosen for neutron-irradiated SiC-matrix material. The effect of temperature on the strength of SiC bulk material depends on the manufacturing process and environment. However, up to about 1300 °C, silicon-based carbides show insignificant levels of loss of strength [55]. Thus, 350 MPa can be taken as a conservative estimate for the high-temperature (1000 °C) tensile strength of neutron-irradiated CVD SiC-matrix material.

The superior high-temperature strength of SiC fibers is well documented. In particular, the effects of various environments have been studied [18]. In vacuum, SiC fibers retain their strength (~1500 MPa) when heated up to 1200 °C [17]. Silicon-carbide fibers exposed to air lose strength above ~1200 °C, mainly because of fiber surface-oxidation

processes. Therefore, care must be taken during manufacturing of SiC composites to minimize the amount of trapped oxygen before the CVI process begins. The maximum operating temperature for SiC composites in ARIES-I has been set at 1100 °C. Below this temperature, no degradation effects resulting from high temperature operation are expected.

The effects of neutron irradiation on PCS SiC (NICALON) fibers was investigated in Japan as part of the national R&D program aimed at developing SiC composites. Both 14-MeV neutrons, from the RTNS-II facility in the U.S., and fission reactor neutrons were used [46, 47]. Samples were irradiated to fluences of 7×10^{21} n/m^2 (14 MeV) and 1×10^{25} n/m^2 (fission spectrum). No significant change in the average tensile strength (2.7 MPa) or the average flexural strength (1.3 GPa) was measured for irradiation up to about 1×10^{24} n/m^2. At 1×10^{25} n/m^2, the tensile strength rises to about 3.2 GPa and the flexural strength increases to about 1.5 GPa. However, the average Young's modulus rises steadily from an unirradiated-fiber value of 160 GPa to about 215 GPa at 1×10^{25} n/m^2 with a corresponding drop in elongation from 1.8% to 1.6%. These preliminary results indicate that SiC fibers have excellent stability under neutron irradiation. Therefore, for SiC fiber properties, neutron irradiation effects are disregarded until a more extensive data base has been developed.

To use conservative properties of SiC fibers, strength degradation of SiC fibers during weaving or braiding processes has to be incorporated. This degradation is caused by an increase in surface flaws and also by fiber breakage during preform fabrication. To account for this effect, the Weibull distribution of tensile strength of SiC yarns is used. Yarns or tows contain between 500 and 1000 monofilament fibers. The strength of SiC yarn is about 2 to 4 times less than that of individual fibers. The average tensile strength of SiC yarn made from NICALON was measured to be ~1400 MPa, while individual SiC fibers have average strengths of above 2400 MPa [56]. Using yarn properties instead of the superior fiber properties, a tensile strength of 750 MPa is chosen. This value was taken from a near-zero probability-of-failure data set compiled by testing over 2000 samples [56]. However, aside from strength degradation, SiC fibers and yarns are frequently broken during manufacturing of the preform. To account for this, a conservative correction coefficient has been formulated [57]. Assuming that 1 out of about every 7 fibers (~17%) break during fabrication, a numerical value of 0.5 is estimated as a correction factor for the tensile strength of SiC fibers. This factor reduces the effective strength of the SiC yarns from 750 MPa to a highly conservative value of 375 MPa.

Thermal conductivity. Neutron irradiation can change the thermal conductivity of materials. The temperature dependence (25 to 1000 °C) of thermal conductivity for various SiC bulk materials exposed to neutron fluences of to 7.7×10^{26} n/m^2 was studied [52]. At 900 °C, unirradiated samples had a thermal conductivity of 62 W/K-m. However, irradiated SiC samples showed a decrease in conductivity to about 37 W/K-m after irradiation to a fluence of 8×10^{24} n/m^2, and to 20 W/K-m after exposure to a fluence of about 8×10^{26} n/m^2 [46, 58]. The drop in thermal conductivity is due to enhanced phonon scattering caused by radiation-induced defects. The thermal conductivity of unirradiated samples decreases with increasing temperature, while that of the irradiated samples is much less temperature dependent. Therefore, above 900 °C, SiC shows a thermal conductivity value approaching that of unirradiated SiC [52, 58]. Thus, although irradiated SiC experiences a drastic drop in thermal conductivity at low temperatures, at high temperatures radiation-induced microstructural changes become less significant when compared to thermally induced phonon scattering.

Since the decrease in both thermal conductivity and swelling are due to similar irradiation-induced microstructural changes, it is not too speculative to assume that the decrease in thermal conductivity will behave like swelling (*i.e.*, saturate at a fluence of around 10^{24} n/m^2). The experiments on thermal conductivity were performed with highly dense, bulk-SiC materials. To evaluate the effective thermal conductivity of SiC composites, micromechanical equations are used [50]. The thermal conductivity is evaluated as a function of the void and fiber-volume fractions in the transverse and longitudinal directions of laminated composites. For lack of an analytical approach to 3-D composites, the laminated composite equations are used. For the matrix, neutron-irradiated (7.7×10^{26} n/m^2 with $E_n > 0.1$ MeV) SiC thermal conductivity of 20 W/K-m was used [58]. The thermal conductivity of SiC fibers at 300 °C was measured to be 25 W/K-m and 21.8 W/K-m, respectively, parallel and perpendicular to the fibers [59]. Neutron-irradiated SiC-fiber thermal-conductivity values are not available. As an approximation, two-thirds of the unirradiated-fiber thermal-conductivity values were chosen. The effective thermal conductivity of an SiC composite material with 10% void fraction and 60% fiber fraction is estimated to be about 15 W/K-m and 10 W/K-m, respectively, in the longitudinal and transverse directions. However, since the design equations were developed for laminated composites, a small increase in the transverse thermal conductivity value to 12 W/K-m can be assumed.

Experimental data on thermal conductivity of 2-D, SiC-fiber-reinforced CVI silicon carbide have been published [60]. The conductivity was found to depend on the degree of densification, and on thermal history. The perpendicular- and parallel-to-fiber orienta-

tions of thermal conductivity values differed by a factor of about 3 at low temperatures, while at temperatures above 1000 °C, the directional dependence drops to within a factor of 2 or less. The measurements show the thermal conductivity value of the SiC composite to be around 19 W/K-m at 1000 °C. Our design equation estimate (~15 W/K-m) compares well with measured values.

Swelling. Neutron irradiation induces atomic displacements that can result ultimately in expansion (swelling) of most materials. Aside from changing dimensions, irradiation-induced swelling can significantly influence physical properties. Neutron-irradiation-induced swelling of bulk SiC material has been investigated since the late 1960s [38, 61]. Swelling of SiC saturates at low fluence levels of less than 2×10^{24} n/m^2 for temperatures below 1200 °C without the formation of visible voids [35, 38, 61]. The saturation value of linear expansion is highest at low temperatures (~0.8% at 200 °C) and falls steadily as the temperature rises (~0.05% at 1100 °C). Above ~1200 °C, swelling increases with no apparent saturation value. It is believed that above 1200 °C, thermal-vacancy generation rates are high enough to enhance the swelling process [39]. By and large, bulk SiC materials show a minimum swelling of less than 1% when exposed to neutron fluences of about 10^{26} n/m^2 [9].

Swelling measurements of SiC fibers have been undertaken recently in Japan [47]. Dimensional changes are deduced from density change measurements. Results show that swelling of SiC fibers is sensitive to fiber choice. For example, although some β-SiC fibers showed no change in density, various amorphous fibers had density changes as high as 5.4% at a fluence of 4.2×10^{25} n/m^2. These measurements, however, do not reflect the effects of expected high helium-generation rate inside SiC during neutron irradiation.

Neutron irradiation generates gaseous transmutation products such as helium and hydrogen. In solids, helium generation is generally associated with swelling because helium tends to agglomerate and form bubbles inside the solid. However, the microstructure of SiC composite materials differs from solids in that it contains up to 10% porosity and a vast network of interconnecting channels along intertwining SiC fibers. The presence of interconnecting pathways may provide escape paths for helium atoms that are generated in the proximity of the channels. Furthermore, the porosity of the SiC matrix material provides pre-existing pores that can absorb helium gases. Alpha-beam irradiation of SiC composite coupons has recently been undertaken [62]. Preliminary investigations have shown no trace of helium inside the composite, lending some support to the suggested effects of composite microstructure on neutron-generated helium behavior. Furthermore, it is speculated here that above 900 °C, the mobility will be sufficiently high for helium

atoms to reach the abundant interconnecting network of cracks and open porosity. Consequently, helium trapping and, therefore, swelling due to helium-atom agglomeration would be minimized.

In summary, SiC composites promise low swelling rates below 1200 °C. However, because there is no data base on the effects of large helium generation in SiC on swelling, it is difficult to go beyond speculative assumptions. Clearly, R&D efforts in this area are most necessary.

Light ion erosion. Plasma-facing material must be able to withstand both physical and chemical sputtering. At temperatures between 900 and 1100 K, graphite has high chemical sputtering yields when exposed to hydrogen ions. In this temperature range, the chemical sputtering yield of graphite is about one order of magnitude higher than the physical sputtering yield [63]. Silicon carbide shows practically no dependency in sputtering yield as a function of temperature [64]. In fact, the use of SiC has been suggested as a protective material for graphite tiles to avoid chemical sputtering. Figure 8.2-2 indicates the sputtering yield of SiC with H, D, ^{4}He, and T. These measurements were made at fluences well above 10^{23} particles/m^2 at temperatures ranging from 20 to 1100 °C [64]. This indicates that chemical sputtering is not a problem for SiC materials [65].

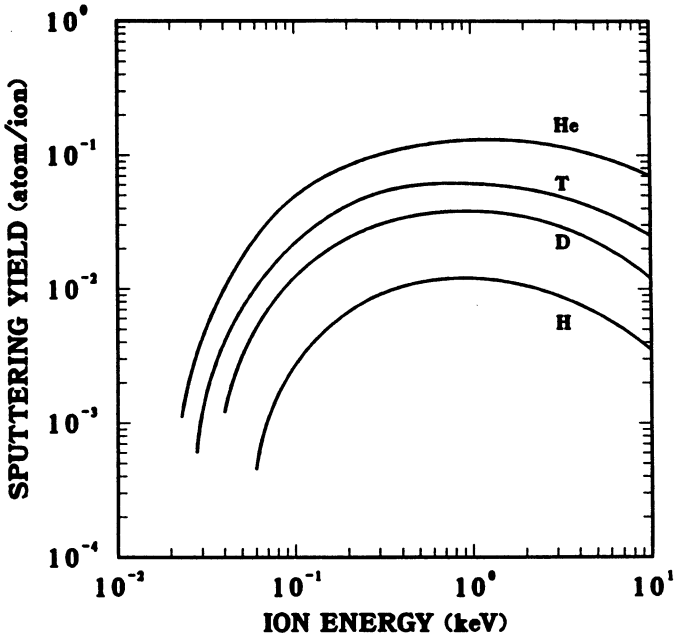

Figure 8.2-2. Energy dependence of the sputtering yield of SiC with H, D, ^{4}He, and T (estimated) [64].

Blistering and flaking. Blistering is a concern for surfaces exposed to helium bombardment. First, helium atoms are implanted into the surface. Then the helium atoms migrate to trapping sites and eventually cause bubble formation underneath the surface, leading ultimately to blistering and flaking of the surface. Although blistering and flaking is a major concern for many metallic alloys, the few experimental results with SiC indicate that it can be avoided entirely in this material [66, 67].

To study the implantation profiles of low-energy helium in SiC, samples were implanted with helium ions ranging in energies from 1 keV to 20 keV [66]. After implantation, the trapped helium concentration was measured by sputtering off surface layers. The experiments indicate that the majority of implanted helium diffuses from its initial profile back to the surface. At high fluences (above $\sim 2.6 \times 10^{21}$ ions/m^2), most of the implanted helium is found to escape from the surface. This avoids the accumulation of implanted helium and, thus, erosion loss of surface layers due to blistering and flaking drops drastically.

In a similar experiment it was shown that flaking of CVD SiC is completely avoided when the target is pre-bombarded with a continuous energy distribution of helium ions ($\sim 10^{23}$ ions/m^2 at 600 °C) [67]. However, when bombarding the samples with monoenergetic helium at room temperature, the SiC surface becomes highly porous and can be removed easily. This implies that irradiation of CVD SiC at elevated temperatures with helium ions having a continuous energy distribution produces pathways for gas release. Experiments using a Maxwellian distribution with an average energy of 3-keV helium ions also resulted in no blistering and flaking of the CVD SiC.

Although the experiments performed used helium ions in the keV energy range, the results are encouraging. At lower energies, the implantation depths will be smaller and the mean distance for helium atoms to reach an open surface will be shorter. These experiments indicate that the 2-mm-thick CVD SiC layer on the ARIES-I first wall will have ample resistance to erosion caused by helium bombardment.

Hydrogen retention. The ARIES-I first wall is exposed to H, D, and T bombardment from the plasma. Experiments were performed to measure the retention of H and D implanted into SiC crystals [68]. Hydrogen was implanted at 13 keV and deuterium at 10 keV, with implantation fluences up to $\sim 10^{22}$ ions/m^2 at room temperature. For 10-keV D^+, the depth profile peaked around 1000 Å. Following implantation, the crystal was annealed at different temperatures. After annealing the sample at 700 °C for 10 minutes, little deuterium was released. Above 700 °C, the amount of retained deuterium

drops sharply. While up to 700 °C almost all of the implanted deuterium is trapped, at 1200 °C all of the deuterium is released. The ARIES-I first-wall surface temperature is 1000 °C. At these temperatures it is assumed that implanted deuterium or tritium ions will be mobile enough to avoid long-term trapping inside the surface layer. Furthermore, escape paths are continuously produced by helium bombardment [68] and neutron irradiation. These pathways will further enable the release of implanted gaseous ions.

8.2.1.6. Maximum-allowable design-stress criteria

The CLASS code [51] was used to estimate the tensile strength of SiC composites with a ply orientation pattern of -45°/0°/45°/90° as a function of fiber volume fraction and matrix void fraction (a ply is a layer of parallel-oriented fibers). Figure 8.2-3 shows estimated longitudinal strengths of such a composite. Although the strength of the composite increases with increasing fiber-volume fraction, a maximum value of 60% is generally suggested to ensure adequate flow-path area during CVI of the matrix material. Using a safety factor of 2/3, the maximum-allowable primary stress for such an SiC

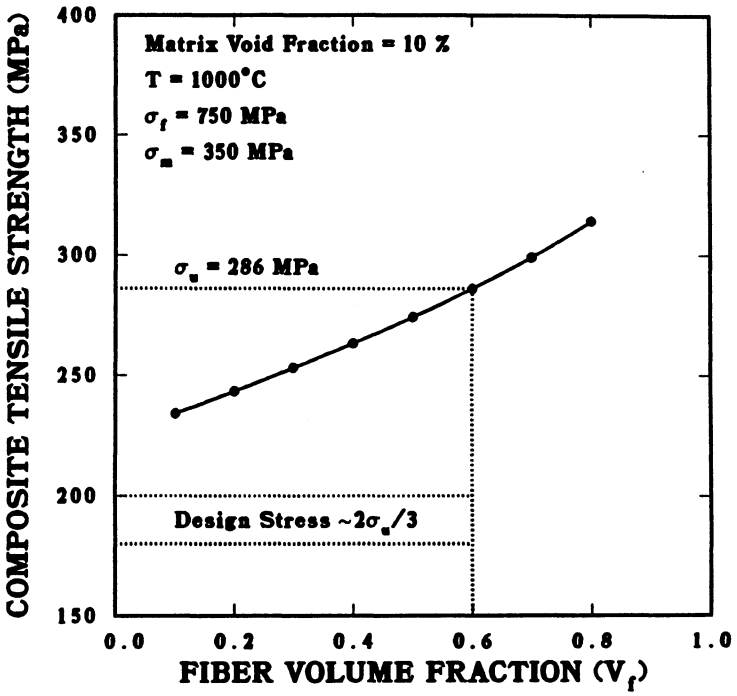

Figure 8.2-3. Longitudinal SiC-composite tensile strength estimated from micromechanical design equations (σ_f is the SiC-fiber tensile strength; σ_m is the SiC-matrix tensile strength).

composite having 10% porosity would be around 190 MPa at 1000 °C. The choice of a safety factor is still arbitrary at present, since there are no firm guidelines for determining maximum allowable stresses for ceramic-matrix composite (CMC) materials. Even within the commercial sector of the CMC industry, differences of opinion exist.

Some members of the CMC industry suggest following the ASME Boiler and Pressure Vessel Code, which states that the maximum allowable stress for time-dependent loads is the lowest value of 2/3 of the minimum stress to cause rupture, or 80% of minimum stress to cause tertiary creep, or the minimum stress to produce 1% strain (all in time, t) [69]. For lack of any defined standards for ceramic composites, the 2/3 safety factor can be adopted as a crude measure for maximum-allowable primary stresses. Other CMC manufacturers, such as Amercom [70], suggest that the maximum-allowable primary stress for CMC materials (*i.e.,* about 140 MPa for SiC composites) should be taken as the stress that causes the onset of micro-cracks in the matrix. NASA/Lewis research laboratories also suggest that matrix failure, not composite failure, should be chosen as a guideline for establishing a maximum-allowable stress criteria [10]. The reason given by NASA is that for many of their applications (such as high-temperature gas-turbine components), oxygen ingression has to be minimized to prevent oxidation and consequent weakening of the fiber/matrix interfaces and of the fibers themselves. Based on these discussions, the ARIES-I team has adopted 140 MPa as the maximum-allowable design stress for primary stresses.

For lack of any well-defined allowable thermal (secondary) stress criteria, the thermal shock resistance of SiC composites is used as a guideline. When heated with a gas flame to 1100 °C, SiC composite tubes can withstand a continuous jet of cold water without damage [71]. Comparable tests of monolithic SiC tubes immediately result in complete shattering of the tubes. Based on the excellent thermal-shock resistance of SiC composites, a highly conservative maximum-allowable secondary-stress limit of 190 MPa is chosen (*i.e.,* 2/3 the longitudinal ultimate strength).

Design criteria also involve a maximum allowable temperature based on swelling of SiC and strength degradation of the fibers. Bulk SiC material exhibits a minimum of swelling at around 1100 °C. Structurally, today's SiC-fiber strength degradation becomes significant above 1200 °C because of excess oxygen or nitrogen remaining from the manufacturing process. Recent developments by the HITCO Company have resulted in the manufacturing of near-stoichiometric SiC fibers that ultimately should show very little strength degradation above 1200 °C [72]. Thus, a maximum operating temperature of 1100 °C has been chosen. Properties of the SiC composites used in the ARIES-I design are given in Table 8.2-IV.

Table 8.2-IV.
Properties of the SiC Composites Used in the ARIES-I Design

Property	Composite[a]	CVD Layer
Density (kg/m^3)	2,500	3,100
Young's modulus, E (GPa)		
E_x	364	320
E_y	360	320
Poisson's ratio, ν	0.16	0.17
Thermal-expansion coefficient, α (10^{-6}/K)		
α_x	4.4	4.5
α_y	4.3	4.5
Thermal conductivity, k (W/K-m)		
k_x	15	15
k_y	12	15
Allowable stress (MPa)		
Primary	140	140
Secondary	190	140

[a]Properties were calculated using the CLASS code [51] with a ply orientation pattern of -45°/0°/45°/90°, a fiber volume fraction of 60%, and a void fraction of 10%.

8.2.1.7. Manufacturing ceramic composites

The manufacture of fiber-reinforced ceramic composites starts with taking uniform arrays of fibers or yarns, putting them in a weave, cloth, or braid to form a fiber *preform*, and then infiltrating it with ceramic matrix precursors. These precursors could be solids, powders in slurries, or liquids (such as polymers), which are then converted to ceramics. The other more widely used method of synthesizing ceramic-matrix material is chemical vapor infiltration (CVI). Chemical vapor infiltration is performed inside a resistance-heated CVI reactor. By decomposing methyltrichlorosilane ($CH_3SiC\ell_3$) gas on the surface of the SiC fibers at temperatures around 1000 °C, $HC\ell$ gas escapes leaving behind SiC matrix. Previously, infiltration times on the order of weeks were necessary to produce millimeter-thick SiC-composite materials. However, processes developed by General Atomics and by the Oak Ridge National Laboratory reduce infiltration times from weeks to about 24 hours [15]. These new CVI techniques form the SiC matrix by a comparatively low-stress low-temperature process, avoiding many of the problems associated with conventional processes for ceramics manufacturing.

Mechanical working (*e.g.,* grinding, drilling, or milling) of ceramics initiates surface flaws, resulting in a reduction of strength and toughness of a component. A major advantage of the ceramic-composite manufacturing techniques mentioned above is that the result is a near net-shape component that requires only minimal finishing touches. Another advantage of composites over bulk ceramics is the ability to create large irregular solid or hollow shapes. Attachment holes and flanges can be integrated during preform weaving without severing fibers, which reduces or eliminates subsequent brazing or bonding between component sections. Complex components for missiles, aircraft structures, integral hub and blade marine propellers, and liquid-propulsion thrust chambers are now routinely manufactured for government or private industry clients [54].

Two-dimensional (2-D) composites are manufactured by sandwiching sheets of reinforced composite layers with a resin material that, upon curing, binds the layers together. A major problem encountered in many 2-D composites is interlaminar crack growth leading to delamination, which occurs primarily between layers of such resin-based composites. Three-dimensional weaving followed by CVI of ceramic matrix material eliminates the delamination problem. Recent innovations in braiding and filament winding techniques enable high degrees of accuracy. Currently, 3-D seamless patterns can be formed by continuous intertwining of fibers, resulting in damage-tolerant preforms that are resistant to interlaminar crack growth and delamination. Computer-aided filament-winding machines are capable of controlling individual fiber placement within one thousandth of an inch [54]. This automated, high-speed, filament-winding technique is embodied in

a four-axis microprocessor-controlled machine that produces parts that are up to two meters in diameter and seven meters in length.

At present, the shape and size of components is more limited by CVI furnace size than by weaving machine capabilities. However, over the past few years, furnace sizes have been increased from a few 10s of cm in diameter to about 1.5 m in diameter. In these reactors, corrugated SiC-composite heat-exchanger panels with dimensions of 1 m $\times$ 1 m $\times$ 1 cm are now routinely manufactured [71].

Matrix formation techniques are still under development. The primary goal is to enhance matrix densities. Currently, SiC composites with matrix densities as high as 90% theoretical density are routinely manufactured. Recent developments by the private sector have resulted in manufacturing nearly 100%-dense SiC composites by using SILCOMP as matrix material [73]. SILCOMP is the trade name for SiC that has been reaction-bonded by using fine graphite particles dispersed in pure Si metal. When silicon is heated to its melting temperature (1412 °C), it readily reacts with graphite to form SiC. The end product of this process is SiC that contains about 8% to 12% free Si.

8.2.1.8. Manufacturing the ARIES-I Fusion Power Core

The first-wall and blanket interior of the ARIES-I reactor lends itself quite uniquely to current SiC-composite technology. Recent developments by private industry have resulted in the manufacture of an SiC-composite heat-exchanger panel that resembles the ARIES-I first-wall and blanket configuration [74]. The heat exchanger panel consists of a tube-sheet with channels having 6-mm inner diameter and 8 mm outer diamater. The weaving machine is programmed to weave an entire sheet of tubes by serpentining SiC fibers from tube to tube. Thus, the tube-sheet is woven as a unit, eliminating the need to manufacture and assemble individual tubes to form a panel, which also eliminates brazing and the weak points it creates. Furthermore, since flat plates are integrally woven to one or both faces of the tube-sheet, later attachment of such plates is unnecessary. It should be noted that such a composite tube-sheet is structurally quite different from conventional metallic tube banks because welding metallic tubes together changes the microstructure of the tube wall in the vicinity of the weld and weakens the individual tubes.

The ARIES-I blanket consists of 17 nested shells, resembling the arrangement of conventional tube-sheet metallic heat exchangers. Discussions with General Atomics [75] resulted in the following blanket-module construction scenario (Fig. 8.1-6):

- The first wall and all interior blanket shells, with embedded cooling channels, the back panels (consisting of inlet and outlet plenum), and the top and bottom panels for the blanket-module are manufactured and readied for assembly.
- The shells are nested into each other starting with the largest (*i.e.,* the first wall) followed by the blanket shells. Spacers are used to ensure proper distances between the tube-sheets and for alignment when the tube-sheets are fitted into the back panel slots.
- The back panels of the blanket, comprising the inlet and outlet plena, are lowered with the tube-sheets into the slots provided. Prior to installation, the endings of the tube-sheets are pasted with brazing material. When heated to about 1400 °C, the brazing materials transform into SiC (by reaction bonding), resulting in a braze that has properties very similar to those of the base material (*e.g.,* the same melting temperature as the structure). To minimize the areas heated during brazing, electron beams are being considered as the heat source.
- Flat sheets of SiC composite are brazed to the top and bottom of the module.
- The breeding and multiplying materials (pebbles) are poured into the spaces between the shells through holes in the back panel and are then vibration packed. These holes are closed afterwards by simple plugs.

Reviewing the ARIES-I FPC design, the Amercom [70] company has confidence that, given present technology, a prototype of a blanket module can be manufactured and tested. Amercom suggests that the first wall can be integrally woven to a plenum in back of it, thus eliminating the need to braze the tube-sheet to the plenum. However, after completion, the top and bottom lids of the blanket would still have to be brazed on.

8.2.1.9. Summary and R&D directions

Silicon-carbide (SiC) ceramic materials have been considered previously as candidate structural materials for fusion reactors [9]. Silicon carbide has excellent high-temperature capabilities, thermal-shock resistance, chemical stability, and environmental resistance. These characteristics, coupled with very low induced activation and afterheat, make SiC a very promising material for future fusion applications.

The primary difference between metals and ceramics is bonding type (Sec. 8.2.1.1). As a result, in metallic alloys, the stability and properties depend in large measure on the

average, rather than local, distribution and position of dissimilar atoms. In ceramics, it is the local distribution of dissimilar atoms that determines its properties. Thus, ceramics may have a higher tolerance to displacive radiation than metals. In addition, metals have the ability to plastically deform before failure (ductile failure), whereas ceramics do not show plasticity (brittle failure).

The ARIES-I reactor uses SiC-fiber-reinforced SiC-matrix composites (SiC composites) as the primary structural material. The primary advantage of ceramic matrix composites (CMCs) over bulk ceramics lies in the ability to obstruct matrix crack propagation. The fracture toughness of CMCs does not rely on the toughness of the matrix but on the interaction of matrix cracks with fibers, or any other reinforcing network.

Aspects of the response of CMCs to neutron irradiation have been discussed. Irradiation experience with bulk SiC was briefly reviewed, followed by an account of the available SiC-fiber irradiation data (Sec. 8.2.1.1 through 8.2.1.5). Depending on the manufacturing process, bulk SiC shows good resistance to neutron irradiation, with no evidence of voids or helium bubbles when irradiated up to 20 dpa and at temperatures below 1250 °C. Amorphous and crystalline fibers both show good radiation-damage resistance when exposed to 14-MeV neutrons (low fluences); however, some irradiation hardening was observed when exposed to fast fission spectrums. Experiments with boron-doped SiC and low irradiation temperatures ($< 1000\,^{\circ}C$) show no evidence of helium bubbles. The effects of high helium-generation rates still need to be investigated. The primary questions are whether helium bubbles will form, given a large pool of helium atoms, and whether SiC composites will release or retain large numbers of helium atoms without forming bubbles. Based on the nature of polycrystalline materials, indications are that the effects of high burnup would not be as serious as they would be for metallic alloys.

The composite materials industry has developed numerical codes to estimate thermomechanical properties of composites as a function of composite characteristics (*i.e.*, fiber volume fraction, matrix void fraction, and fiber orientation). The code, CLASS, used for ARIES-I was developed by Materials Sciences Corp. [51]. The properties used for ARIES-I design are discussed in Sec. 8.2.1.6 and summarized in Table 8.2-IV.

Manufacturing techniques for SiC composites were reviewed in Sec. 8.2.1.7, and cost estimates for SiC composites are discussed later in Sec. 8.2.5. Although the engineering data base for SiC composites is very small, this material was identified as the most promising composite because of excellent high-temperature capabilities and its favorable neutronics characteristics. However, since CMCs have been under development for only the past 5 to 10 years, many engineering issues will require intense R&D efforts before SiC composites reach levels of reliability similar to that of metallic alloys.

The research and development efforts required can be divided into four categories: (1) understanding fundamental material performance, (2) developing manufacturing techniques that result in standardized and economical production processes, (3) developing radiation-damage-tolerant composite materials, and (4) studying light-ion interaction.

Understanding fundamentals. Fundamental processes that need extensive research are those that lead to crack initiation and absorption of energy during crack propagation. The goal is to develop a ceramic matrix material that does not show a spread in failure strength but has predictable failure criteria. This research requires an understanding of the basic factors responsible for ceramic failure and, as such, will require support from the international material science community.

Manufacturing techniques. The composite materials industry, now enjoying strong growth, is working to find solutions to critical issues, including manufacturing cost reductions. Automobiles still appear to be nearly all steel, but in fact about 8% of their weight consists of composites (*e.g.,* bumpers, doors, body panels, turbochargers, *etc.*). For example, the turbochargers available in high performance automobiles are made of ceramic blades that are joined to a metallic shaft. Thus, a reliable and workable solution has been demonstrated for joining ceramics to metallic alloys. The sports equipment industry has always been a front-runner in the commercial use of composites (*e.g.,* bicycle frames, tennis rackets, golf clubs, fiberglass pleasure boats, *etc.*) Currently, the aerospace industry is the biggest market for composites (Beech Aircraft's Starship uses composites extensively). The largest user of advanced composites is the military with well over 80% of market share. The most sophisticated utilization of composites is probably in the Stealth bomber. Other military uses of advanced composites are for missiles and future high-performance jet engines.

The examples cited above amply demonstrate that a dedicated fusion composite-materials R&D program does not have to burden itself with developing solutions to the basic problems and issues of composite manufacturing techniques. The main thrust of such a fusion program can be directed at finding solutions to fusion-specific manufacturing issues, such as: (1) manufacturing large-scale components, (2) gas leak tightness, (3) brazing and joining processes, and (4) joining to other materials. The SiC-composite commercial sector of the industry has developed dedicated solutions to all of the above issues. However, most efforts to date have only demonstrated solutions for small component sizes with emphasis on one or two of the problems at a time. It is generally

recognized that there is a need to develop and demonstrate the ability to incorporate these solutions into one all-encompassing manufacturing technique.

Development of radiation-damage-tolerant CMCs. For fusion applications, the critical issue that needs to be addressed is the response of CMCs to neutron and ionizing radiation so that appropriate materials can be developed. This is an issue not being pursued by the CMC industry. For use in fusion applications the fusion-specific R&D needs for CMCs are:

- **Understanding fundamental processes.** The understanding of fundamental neutron-irradiation effects on ceramics and, in particular, on CMCs is by no means as advanced as it is for metallic alloys. Ceramics behave differently from metallic alloys when exposed to damage-inducing radiation, because in ceramics a second lattice (superimposed on the host lattice) exists. Thus, there is the additional constraint of stochiometric point-defect interactions. Experiments need to be set up to understand these fundamental processes.
- **Understanding the effects of irradiation on a composite microstructure.** Because of the fiber/matrix interface and the presence of matrix voids, the behavior of transmutation products (helium and hydrogen) will differ from those in solid bulk material. These microstructural characteristics, specific to CMCs, will affect the swelling behavior. Understanding these phenomena is crucial to the development of fusion-relevant composite materials.
- **Investigating the effects of ionizing radiation on the thermal and electrical conductivities of CMCs.** The effects of ionizing radiation on CMCs can be used to tailor composite materials to desired levels of thermal and electrical conductivities. It is well-known that SiC is a semiconductor, and small additions of Aℓ, Be, or Fe can vary the electrical conductivity of SiC to bridge the conductivity range from an insulator to a fair conductor.

Light-ion interaction. The effects of H, D, T, and ^{4}He bombardment on SiC have been investigated in recent years. Indications are that SiC has good resistance to erosion caused by helium implantation. Trapping of H, D, or T has also been studied. It appears that at elevated temperatures, the hydrogenous ions can overcome the high trapping energies and migrate back to the surface. However, in order to confirm that SiC can withstand nominal scrape-off layer environments, many topics need to be investigated.

One of these is the synergistic effects of hydrogen and helium bombardment on surface morphology during irradiation in a neutron environment.

In summary, because of inherent microstructural characteristics, composite materials behave in unexpected and surprising ways when placed in a neutron and ionizing radiation environment. Understanding these behaviors will enable the development of future radiation-damage-tolerant materials. The R&D program for fusion-dedicated composites will be able to concentrate on fusion-specific problems because other engineering issues are already being addressed by the composite-materials manufacturing industries.

8.2.2. Solid-Breeder Material

The operating conditions of ARIES-I are very different from those of ITER [76]. ARIES-I operates at a much higher temperature, requires a much longer wall lifetime at a higher wall loading, and requires a much higher tritium-breeding ratio to ensure tritium self-sufficiency. The ARIES team is also studying the feasibility of a low-activation and low-afterheat blanket design. Therefore, the material selection criteria of ARIES-I are also very different from those of ITER.

For the ITER design, Li_2O is most attractive because of its lithium atom density, thermal conductivity, thermal response time, and tritium lattice diffusivity. It also ranks very high in terms of activation and afterheat considerations. However, at the conditions required by ARIES-I, the problems associated with Li_2O (*e.g.*, lithium mass transport, chemical interaction with structural material, and thermal expansion and swelling) become much more severe than they are under the ITER operating conditions. The ARIES-I team, therefore, made a complete evaluation of candidate solid-breeder materials for the high-temperature, high-fluence operating conditions of the ARIES-I blanket.

The performance characteristics of the four potential solid-breeder candidates (Li_2O, Li_4SiO_4, Li_2ZrO_3, and $LiA\ell O_2$) under normal (pulsed and steady-state) and off-normal operating conditions were considered in this evaluation. The primary performance parameters for normal operation are those for tritium breeding, lithium burnup, thermal transport, tritium transport, thermal and in-reactor volume change, chemical stability with cladding materials, lithium mass transport, and activation. Secondary parameters for normal operation include mechanical properties and grain growth. Additional properties considered for off-normal and accident conditions include decay heat rate, latent heat of melting, volume changes from high-temperature phase melting, and chemical compatibility with moisture and beryllium. This comparison was carried out for ITER

activities and extended to ARIES-I. The similarities and dissimilarities between ITER and ARIES-I will be documented here.

Table 8.2-V is a summary for evaluating the four solid-breeder candidates. Rather than presenting a complete picture of the data base for each breeder material, the table is designed to show the strongest and the weakest characteristics. In most of the categories, Li_2O performs very well relative to other breeder ceramics, particularly in the area of lithium atom density, thermal conductivity, tritium transport (expressed as the minimum temperature for a one-day average residency time for the tritium in the ceramic), and activation. Its volume change due to thermal expansion and helium-induced swelling may be a problem and has to be included in the design considerations. Lithium oxide also has a higher potential for problems than other breeders with regard to chemical compatibility with structural material, Be, and moisture. Lithium mass transport may also be a problem at high temperatures. While these issues may not be critical for ITER, they may seriously limit the upper temperature of Li_2O that will be required for ARIES-I.

Lithium orthosilicate properties appear to lie between those of Li_2O and the other two ceramics. It is better than Li_2O in terms of in-reactor volume change, compatibility, and lithium mass transport. It has very low activation. Since ARIES-I is investigating the feasibility of a very low-activation blanket, Li_4SiO_4 was considered as the first candidate. The major reason that Li_4SiO_4 was not selected as the primary candidate for ITER was due to concern about a possible tritium-release problem at higher burnup as Li_4SiO_4 is converted to Li_2SiO_3, which has poor tritium-release characteristics. For the ARIES-I blanket, the problem might be more severe because of the higher burnup and the higher breeder-material temperature. Figure 8.2-4 shows a phase diagram of the Li_2O and SiO_2 chemicals [77]. As the burnup occurs, the chemistry of the compound moves in the direction of the SiO_2. It appears that there is a chemical form of Li-Si-O compound that has a melting temperature of 1040 °C. The ARIES-I blanket design has a maximum breeder-material temperature of 950 °C. As the material temperature approaches the melting temperature, radiation-enhanced sintering will occur and grain growth will be important. This problem may not be severe for ITER because of its relatively low operating temperature. However, the burnup may have two effects on Li_4SiO_4 in the ARIES-I blanket. The first is the change of chemical composition toward Li_2SiO_3, which has poor tritium release characteristics. The second is the lower melting point of the compound between Li_4SiO_4 and Li_2SiO_3 which, together with the anticipated high blanket temperature, may cause sintering problems. Because of these effects, the tritium inventory in the blanket can not be estimated.

Table 8.2-V.
Thermophysical Properties of Candidate Breeder Materials
(at 80% density and 80% enrichment)

Property	Li_2O	Li_4SiO_4	Li_2ZrO_3	$LiA\ell O_2$
^{6}Li density (kg/m^3)[a]	744	432	264	224
Melting temperature, T_{melt} (°C)	1,432	1,255	1,616	1,610
Phase-change temperature (°C)	None	655	1,100	None
Volume change due to phase change (%)	None	0	13	None
Thermal conductivity[b] (W/K-m)	3.54	1.73	1.43	1.92
Thermal diffusivity[b] (%)	0.857	0.419	0.319	0.679
Minimum temperature (°C) for one-day T residency time	320	400 (±25)	320	525(±25)
In-reactor volume change[c]	High	Intermediate	Low	Low
Incompatibility and Li mass transport[c]	High	Intermediate	Low	Low
Activation[c]	Zero	Low	High	Intermediate
Afterheat[c]	Zero	Low	High	High

[a]For 100% dense material.

[b]At 600 °C.

[c]Relative ranking.

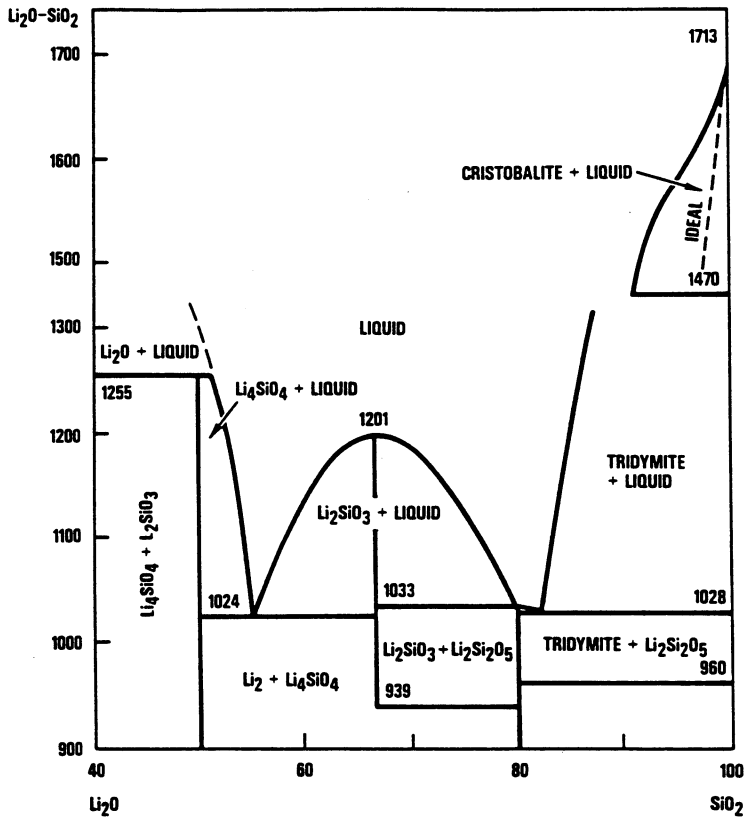

Figure 8.2-4. Phase diagram of SiO_2-2 Li_2O × SiO_2 system.

It appears from the phase diagram (Fig. 8.2-4) that adding Li_2O to the Li_4SiO_4 may prevent formation of Li_2SiO_3 and of the low-melting-point Li-Si-O compounds. The chemical thermodynamics favor conversion of Li_2SiO_3 and Li_2O to Li_4SiO_4 so as lithium is converted to tritium and extracted from the blanket, only Li_2O would be depleted. The kinetics of this process, however, would rely on diffusion of lithium from the Li_2O fast enough to replace lithium lost from Li_4SiO_4. Since these kinetics are unknown, there is a high degree of uncertainty regarding the chemical stability of Li_4SiO_4 under irradiation.

Lithium zirconate has excellent tritium-release characteristics. It is very stable to the effects of temperature and irradiation but its activation and afterheat are the highest among the four breeders (although they may be reduced by isotopic tailoring, as discussed in Sec. 10). Lithium zirconate has a low thermal conductivity, however this problem can be corrected by mixing the breeder material with Be.

Lithium aluminate is stable at high temperatures. It was not selected, however, because of its waste disposal problem due to the production of $^{26}A\ell$ from $^{27}A\ell$(n,2n) reactions. Isotopic enrichment will not alleviate this problem.

Table 8.2-VI summarizes the comparison of the ceramic compounds for the ARIES-I application. On the basis of this comparison, isotopically tailored Li_2ZrO_3 is selected as the breeder material for ARIES-I. It should be noted that even after extensive isotopic tailoring, the off-site dose after a severe accident in the ARIES-I reactor is still dominated by Zr (Sec. 10). This provides a strong incentive to develop an alternate, low-activation solid-breeder material. The second choice is Li_4SiO_4. This material exhibits very low activation and afterheat without the need for isotopic enrichment. It would permit thermal design conditions comparable to those of Li_2ZrO_3. Considerable uncertainty exists, however, regarding the chemical stability and tritium inventory of Li_4SiO_4 under high lithium burnup. This uncertainty should be resolved by the breeder-material development program. If the results of these experiments prove to be positive for Li_4SiO_4, it could be substituted for Li_2ZrO_3 in the ARIES-I design with virtually no design changes. The third choice is Li_2O, which would have zero afterheat and induced radioactivity, but would require a lower operating temperature than Li_2ZrO_3 or Li_4SiO_4. The last choice is $LiA\ell O_2$ because of its unavoidably high levels of induced activity and afterheat.

8.2.3. Neutron Multiplier Material

Beryllium is chosen as the neutron multiplier material for the ARIES-I reactor design mainly because of low activation. It also combines the highest thermal conductivity with the lowest density of all candidate neutron-multiplier materials. Concerns associated with Be are toxicity, resource limitation, and radiation damage. Recently the toxicity of Be has received a lot of attention. Indications are that beryllosis is contracted only by a small percentage of those of the general public who are sensitive to beryllium oxide (BeO). Furthermore, solid beryllium, whether it be the pure metal, ceramic oxide, or any type of alloy, does not present any health risks unless finely divided into dusts or fumes. Only particle sizes of 5 μm or less are capable of entering the alveolar spaces and becoming engulfed by macrophages [78]. This means that both conditions, being sensitive and being exposed to a particular size of BeO particles, must be met before beryllium poses any threat to the general public. Issues regarding resource limitation are reported in detail in Ref. [79]. Below, the properties of beryllium are presented briefly and the issue of swelling of Be is discussed.

8.2.3.1. Properties

Selected properties of beryllium are given in Table 8.2-VII. The ARIES-I reference blanket uses a mixed sphere-packed beryllium and breeder (Li_2ZrO_3) material. The

Table 8.2-VI.
Comparison of Ternary Ceramics

- Activation and Afterheat

  $Li_2O$and Li_4SiO_4 are good, Li_2ZrO_3 and $LiA\ell O_2$ are bad.

  To alleviate activation and afterheat, Li_2ZrO_3 can be isotopically tailored.

- Phase Change

  Li_2ZrO_3 has a phase change with 13% volume increase at 1100 °C;

  operation with $T_{max} < 1000\,°C$ is reasonable.

  Li_2O, Li_4SiO_4, and $LiA\ell O_2$ have no phase change concerns.

- Tritium Transport

  Li_2ZrO_3 and Li_2O are superior to Li_4SiO_4 and $LiA\ell O_2$.

- Thermal Transport

  $LiA\ell O_2$ is better than Li_4SiO_4 or Li_2ZrO_3 at $T < 700\,°C$.

  All three are comparable for $T > 700\,°C$.

  Thermally induced transport of Li_2O is a concern.

- Mechanical Integrity

  Li_2ZrO_3 and $LiA\ell O_2$ are superior to Li_4SiO_4 and Li_2O.

- Chemical and In-Reactor Stability

  Li_2ZrO_3 and $LiA\ell O_2$ are superior to Li_4SiO_4 which is superior to Li_2O.

Be sphere sizes chosen are 1- and 0.1-mm in diameter. The theoretical density achievable with these two sizes is about 80% [1]. The breeder/multiplier sphere-pac thermal conductivity was estimated to be 4.6 W/K-m with a heat transfer coefficient of about 6649 W/K-m^2 (Sec. 8.5.2). Beryllium has a melting temperature of 1283 °C. Therefore, mechanical properties degrade rapidly above 700 °C. At 25 °C, the ultimate tensile strength of Be is about 260 MPa, while at 1050 °C it is only 25 MPa [80]. In the ARIES-I reactor, however, the breeder/multiplier material does not have to carry any loads, except for its own weight. Thus, no analysis was done for the mechanical response of the multiplier.

8.2.3.2. Swelling

In a fusion environment, irradiation-induced swelling is a major concern associated with beryllium. Under neutron irradiation, swelling is mostly caused by helium gas generation from (n,α) reactions. Helium atoms are insoluble in metals and, consequently, they rapidly diffuse through the metal until they reach open surfaces and escape or become immobilized at trap sites (*i.e.*, thermodynamically and irradiation-produced dislocations, cavities, and grain boundaries). The latter phenomenon is responsible for the nucleation and growth of bubbles. At elevated temperatures, bubbles migrate through the matrix or along grain boundaries and coalesce to form bigger bubbles (increased swelling).

The threshold temperature, below which swelling of beryllium is insignificant, was determined in early post-irradiation experiments [81–84]. For fluences resulting in a few atomic parts per million (appm) of helium-atom concentration in Be, the threshold temperature is around 700 °C, while for fluences creating more than 50 appm of helium, the swelling threshold temperature drops to about 500 °C. Beryllium located behind the first wall of the ARIES-I reactor will have a helium generation rate of about 20,000 helium appm per full power year. The maximum ARIES-I breeder/multiplier temperature in the first zone behind the first wall is about 800 °C. Thus, conditions of high helium-generation rate and operation above the swelling threshold temperature, are both present in the ARIES-I reactor.

High-temperature (1000 °C), post-irradiation anneal experiments showed a maximum swelling of 30% for highly dense Be [85]. The maximum swelling value was attributed to interconnecting bubbles that release trapped helium from the bulk. The minimum swelling necessary to produce an interconnecting network of helium bubbles for gas venting was theoretically determined to be between 5% and 10% [86]. To enhance helium mobility, a fine-grain Be morphology (large number of grain boundaries) is desired. Thus,

Table 8.2-VII.
Selected Properties of Beryllium[a] [80]

Density (kg/m^3)	1,850
Melting temperature (°C)	1,283
Heat capacity (J/kg-°C)	
500 °C	2,250
1000 °C	2,920
1500 °C	3,590
Coefficient of thermal expansion (10^{-6}/K)	
25 – 100 °C	11.6
25 – 500 °C	15.9
25 – 1000 °C	18.4
Thermal conductivity (W/K-m)	
50 °C	150
300 °C	125
600 °C	90
Bulk modulus (GPa)	115.8
Shear modulus (GPa)	157.7
Young's modulus (GPa)	278.5
Poisson ratio	0.085
Ductility	Poor
Ultimate tensile strength (MPa)	
500 °C	260
700 °C	170
900 °C	120
Yield strength (MPa)	
500 °C	140
700 °C	100
900 °C	80

[a]Properties may vary considerably from product to product, depending on impurity content, density, and preferred orientation.

Be exposed to high levels of fast neutron irradiation will swell a minimum of about 10% and a maximum of 30% at temperatures above 750 °C. Based on these results, there is a minimum and a maximum swelling level that depends on helium generation rate, operating temperature, and morphology.

In general, structural integrity of a component is the primary design requirement. Given the low ductility, microcracking of Be is difficult to prevent. This is mostly because the multiplying material experiences loading stresses from thermal expansion, irradiation-caused differential swelling, and from external forces. For the ARIES-I reactor, however, the goal is to allow these loading stresses to cause crack nucleation and propagation. The reason is that microcracks generated in this fashion would provide escape channels for helium and ensure open porosity even at high temperatures.

To this end, a sphere-packed breeder/multiplier mixture was chosen. Depending on the packing fractions of different sizes of pebbles, an open porosity between 15% and 30% can be designed into the multiplier material. The open porosity in the multiplying material is capable of venting helium, providing the helium reaches these sites. Based on the self-diffusion equation of Be [87], a helium atom can travel a typical distance between open pores of 10 μm in about 0.05 s at 700 °C. However, it should be noted that the open porosity is maintained only if the maximum Be temperature does not exceed 660 °C. Above this temperature, sintering rates increase drastically, which eventually results in pore closure [88]. The maximum Be temperature in the ARIES-I reactor is estimated around 800 °C. At this temperature, the sintering rate is rapid, resulting in closure of open pores. However, because swelling rates in Be increase drastically at high temperatures, the sintered Be material will swell locally to extremely high values. The high differential-swelling rates within the beryllium microspheres will result in large stresses, which are relieved by crack formation and crack propagation. Upon cracking, an escape path becomes available and swelling resulting from helium entrapment is locally and temporarily relieved. The cycle continues because, after helium release, the differential stresses are relieved and the material starts sintering again until pore closure occurs.

The alternating cycles of swelling and microcracking may ultimately lead to a quasi-equilibrium helium-venting rate resulting in a low maximum-overall swelling value. Although no experimental work has been undertaken to confirm this process, data on the plastic strain-at-failure indicates that such a process is likely to occur in high porosity Be [89]. The data show that as the porosity of Be increases from 5% to 26%, the plastic strain-to-failure decreases from $\sim$1% to $\sim$0.08%, indicating a significant decrease in ductility. Furthermore, when exposed to neutron irradiation, Be will also undergo significant irradiation hardening. Irradiation hardening in Be is caused by matrix hardening

due to bubble pinning of dislocations and by grain boundary weakening due to helium accumulation at the boundary. Thus, high porosity Be exposed to high fluences at high operating temperatures could exhibit a cyclic behavior of swelling, microcracking, and sintering. It is anticipated that with such a self-regulating mechanism, the maximum swelling of Be may stay well below ~10%.

8.2.3.3. Summary

Toxicity considerations of Be are presently being addressed and may ultimately result in a Be technology that meets full public acceptance. The issue of resource is still under debate with no definite answer as to whether the issue is one of absolute resource limitations, cost, or reprocessing. The effects of high operating temperatures (>600 °C) on gas-driven swelling is not clear at all. Although at high temperatures large swelling rates are anticipated (based on annealing experiments), radiation-induced hardening processes coupled with differential swelling stresses may result in a swelling-rate-limiting microcracking-sintering phenomena. If, however, such a process proves to be less significant than suggested here, a maximum swelling of about 10% is anticipated because of the formation of an interconnecting network of helium bubbles, provided a fine-grained Be material is used [86].

8.2.4. Coolant

Gas-cooled reactor technology has been pursued since the very early days of the nuclear reactor program. It is one of only two technologies, the other being water cooling, that has successfully been developed to commercial status. Gas cooling was originally pursued most vigorously in Europe with the development of the CO_2-cooled MAGNOX reactors. These led to the CO_2-cooled Advanced Gas Reactor program and the helium-cooled High-Temperature Gas-Cooled Reactor (HTGR) program. General Atomics designed and built the 40-MWe prototype Peach Bottom HTGR, which operated successfully for over five years, and also the 330-MWe demonstration HTGR at Fort St. Vrain. Currently, the modular high-temperature gas-cooled reactor (MHTGR) is being developed as a component of the U.S. fission reactor program.

A wide variety of gases have been proposed for use in gas cooled reactors. The technical aspects of gas cooling are reviewed in Ref. [90] and the application of gas cooled technology to fusion power systems is discussed in Ref. [91]. Because of its high heat capacity and thermal conductivity, high sonic speed, and chemical and neutronics inertness, helium has generally been the coolant of choice for gas cooled systems.

8.2.4.1. Advantages of helium

Helium is the most inert of all proposed coolants. It has very small nuclear-interaction cross sections and is virtually transparent to neutrons, allowing excellent neutron economy and fuel breeding performance to be achieved. Because helium is chemically inert, reactions with the fuel, cladding, and environment are not of concern. These properties are very favorable for low-activation blanket designs. Because helium is a gas, no phase changes are possible at the recommended operating conditions, thus the heat transfer regime is stable both in normal, pressurized operation and in the event of depressurization. There is no inherent limit on coolant temperature, which means that high thermal efficiency is possible. At present, the maximum coolant temperature is limited by the structural-material temperature limit.

For magnetically confined fusion systems, the fact that helium is nonmagnetic and nonconductive electrically is an advantage. Because of the low density, gravitational effects are quite small.

Because of the large worldwide gas-cooled reactor program and commercial deployment, gas cooling enjoys a developed technology. The heat transfer and thermal-hydraulic correlations are understood and power conversion equipment (steam generators, circulators, *etc.*) are developed. Helium purification systems have been successfully developed and include the capability for tritium recovery from the helium stream.

From the point of view of reactor maintenance, helium cooling has several advantages. It is optically transparent and does not activate, air can be allowed into the helium system ducting during maintenance, and no special isolation is needed.

8.2.4.2. Disadvantages of helium

The principal disadvantage of all gas coolants is their low volumetric heat capacity. To achieve adequate heat-removal capacity with acceptable coolant pumping-power requirements, pressures in the range of 40 to 100 atm are needed, requiring relatively expensive coolant ductings. The heat transfer coefficient that may be obtained at reasonable flow velocities in a helium cooled system is generally smaller than that found in liquid cooled systems and, hence, the temperature differential is larger, leading to higher fuel and clad temperatures. The power required to operate the helium circulator can be high. With the pressure drops encountered with a steam-cycle power-conversion system, the pumping power is on the order of 2% to 5% of the reactor thermal power.

Because of the low volumetric heat capacity of helium, natural convection cooling is difficult to achieve. Although natural convection can provide some shutdown afterheat cooling when the coolant loop is pressurized, it cannot be depended on in the depressurized state.

8.2.5. Material Cost Estimates

8.2.5.1. SiC composites

To estimate the cost of ARIES-I fusion-power-core (FPC) materials, several leading SiC-composite manufacturers were contacted: Amercom (California)[70], Nipon Carbon (Japan) [92], Dow Corning (Michigan) [93], Lanxide/Du Pont (Delaware) [94], and BP-Chemical/HITCO (California) [72]. All of the companies agreed on several points regarding the cost of SiC composites, the following being the most relevant:

- Manufacturing technology for SiC-composite materials is clearly in its infancy. Currently, the SiC-composite manufacturing industry is very capital and labor intensive.
- Cost projections for SiC composites are very difficult. On a time frame of 20 to 30 years however, a reduction of 40% to 60% from today's prices is very realistic, provided the demand for SiC composites increases.
- Commercially available SiC-composite components are made as special one-of-a-kind orders. Prototypical costs reflect matrix void fraction, matrix stochiometry, fiber volume fraction, fiber grade, component-specific material development (such as fiber coatings), design and implementation of hardware and software for numerically controlled weaving and braiding machines, furnace manufacturing, design and construction of machining equipment, and a waste stream of reject components.
- Industry representatives refused to quote a price for SiC composites on a \$/kg basis. The consensus is that one can only quote \$/component after careful examination of component complexity. Tube-sheets, such as those used in ARIES-I, are not considered to be highly complex. Similar tube-sheets, including flanges and joining holes, have already been manufactured by several companies for heat exchanger technology [70, 94].

- High quality fibers (NICALON, Japan) have dropped in price from \$1500–\$2500/kg in 1987 to about \$650–\$850/kg in 1990 [92]. As competition mounts, more price reduction is expected. Various companies are currently developing new fiber-manufacturing technologies, which may result in a sharp price reduction for SiC fibers. Even if no manufacturing breakthroughs are achieved, Nipon Carbon has projected a 30% to 50% drop in the price of NICALON within the next 10 years [93].

- Currently several major composite-manufacturing companies are developing alternative methods to the costly CVI technique for ceramic matrix formation [92, 94]. One of the methods being pursued uses organic precursors for SiC matrix formation and promises several advantages: (1) Precursors can be in liquid form, which can be pressure driven to infiltrate the preform; and (2) Near-net shape manufacturing techniques can be utilized, which eliminates costly machining and grinding of finished components. The other method, which is further advanced, develops a matrix material by introducing alloys of metals (currently Aℓ and Si) and oxidizing, nitriding, or carbonizing it to form the desired matrix. This manufacturing technique is an extension of the DIMOX (directed metal oxidation) process. One commercial product that is available is SiC-fiber-reinforced alumina (A_2O_3). This material promises a high degree of "self-healing" capability because of the manufacturing technique. Silicon carbide, Si_3N_4, and AℓN matrix composites have been made but are not yet available commercially. Developing cheaper infiltration techniques, may lead to major reduction in price in 20 to 30 years.

- Currently, the largest panels of SiC composite (1 m $\times$ 1 m) are manufactured by two companies, France's SEP and Japan's Nipon. For developing and manufacturing a prototypical component with these dimensions, Nipon [92] charges about \$15,000 for a 2-mm-thick SiC-composite panel, which translates to about \$2500/kg or about \$15,000/m^2. Once a prototype component has been developed, volume production will significantly reduce the price.

Based on these discussions, the general consensus is that, pending an increase in demand for SiC-composite materials, price reductions on the order of 40% to 60% are very likely within a timetable of 20 to 30 years. Given an average cost of about \$1000/kg for small samples, the price projection leads to a value of about \$400/kg (for the ARIES-I design, unit cost in \$/m^2 is used, which is preferred by the industry to \$/kg basis). These projected costs are based on unique conditions for present SiC-composite manufacturing techniques:

1. The price is based entirely on prototypical components because, to date, manufactured SiC-composite materials have been entirely custom tailored as one-of-a-kind components.

2. Because SiC-composite materials are in their developmental infancy (around 5 years), today's component costs include the R&D effort that goes into manufacturing a specific SiC-composite component. In many cases, this involves developing an application-dependent fiber coating, designing and implementing software and hardware for numerically controlled weaving, designing and constructing chemical-vapor-infiltration (CVI) furnaces, and optimizing infiltration techniques.

3. The price does not allow for any reduction based on future technological breakthroughs in the manufacturing process, such as alternatives to expensive and time-consuming CVI process.

In short, because manufacturing SiC-composite components is a highly capital- and labor-intensive venture (raw material cost is very small), the cost issue cannot be fully resolved. The future prices strongly depends on future manufacturing techniques. It should be noted that the growing need for advanced materials in non-fusion related applications, especially ceramic matrix composites (*e.g.*, SiC, Si_3N_4, $A\ell_2O_3$, C), has resulted in increased R&D efforts in Europe, the U.S. [10], and Japan [11, 12]. The interest in SiC is particularly high because of its good oxidation resistance compared to C/C composites which require protective oxidation layers.

8.2.5.2. Cost of ARIES-I components

To estimate the cost of the ARIES-I reactor SiC-composite components, the following assumptions are made:

1. The entire first-wall area is about 600 m^2.

2. There are 17 first-wall-equivalent tube-sheet panels made of SiC composite for a total of 9000 m^2. (Breeding, reflecting, and shielding materials, in the form of a sphere-pac, are poured into the gaps between the 17 SiC-composite shells.)

3. The price used here is the $\$/m^2$ of a prototypical SiC-composite panel, which is about \$15,000 today.

Based on the above assumptions, the total cost for the SiC-composite material in ARIES-I is estimated to be around \$135 M. The CVI process simplifies impurity-level control because the matrix precursors are gases. Assuming that the final cost of an SiC-composite component will double due to the required impurity-content requirements ($\leq$ 1 ppm), the cost of the SiC composites for ARIES-I is estimated to be about \$270 M.

Of the 17 high-quality SiC-composite shells, four are used to cool the shield in ARIES-I. Between these shells is a low-quality SiC/B_4C material with a total volume of about 250 m^3 ($\sim$400 tonne SiC plus $\sim$313 tonne B_4C). The cost of bulk SiC raw material for the shield is currently about \$60/kg (Ceramic Co., U.S. [95]). The SiC powder is sintered at about 2000 °C at ambient pressure to form the ceramic. This is a low-cost process (\$120/kg) that is highly volume driven and can be estimated at about twice the raw material cost. For impurity level control of the shielding material, the assumption is made that the final cost will double to \$240/kg. Thus, the SiC for the shield would cost about \$96 M.

The raw material cost for B_4C is about \$160/kg today [96]. Shaping the B_4C into a desired end product can result in a cost of well over \$2000/kg, depending on the complexity of the component and the density requirements. It should be noted, however, that at the present time, only two major B_4C manufacturers exist (in the U.S. and Japan) and an increase in competition and demand may have drastic effects on the price. Medium density, simple brick-shaped B_4C is significantly cheaper at nominal costs of around \$200 to \$250/kg, based on a large volume order. To reflect the cost of impurity level control for ARIES-I, the cost of the B_4C is estimated to be around \$300/kg for finished monolithic blocks. The cost of B_4C in the shield is therefore about \$94 M. Thus, the total shield-material cost, including the SiC, is estimated to be around \$190 M.

The ARIES-I breeder material consists of 35 tonnes of Zr and 25 tonnes of Li at a cost of about \$50/kg each [97]. Therefore, the total cost of raw metal for the breeder is about \$3 M. (Drastic savings can be realized if electronic quality ZrO_2 and LiOH, which sell at, respectively, about \$7/kg and \$4/kg, are chosen.) The cost of the breeder material is driven by the isotopic tailoring of Zr at a cost of about \$2100/kg. The cost of the breeder material is estimated, therefore, to be about \$80 M.

Table 8.2-VIII summarizes the unit costs for FPC materials used in ARIES-I. Based on today's prices, the total cost of the first wall, blanket, and shield is estimated to be about \$595 M (including the cost of Be neutron multiplier). The systems code result, based on future costs, arrives at a total cost of about \$336 M, which is about 44% less than today's material costs.

Table 8.2-VIII.
Material Unit Costs for the ARIES-I Fusion Power Core

Material	Today's Costs[a] ($/kg)	Projected Costs[b] ($/kg)
SiC composite	1,000[c]	400[d]
C/C composite	200[e]	120
SiC monolithic	120[f]	70[g]
B_4C monolithic	250[h]	200[i]
Zr metal	50[j]	50
Li metal	50[k]	50

[a] Today's price reflects an average quote for small samples.

[b] Projected costs are based solely on increased demand.

[c] Maximum price quoted for large heat-exchanger-type shells is $2500/kg.

[d] Based on a 60% decrease in price within 20 – 30 y.

[e] Today's prices for C/C composites range from $100 to $1000/kg.

[f] SiC raw-material cost is $30/kg; shaping and forming costs are reflected in the $120/kg price.

[g] Based on a 60% reduction over 20 – 30 y. Because of an abundance of material, further reductions based on demand and volume are very likely.

[h] B_4C raw-material cost is around $160/kg; shaping and forming expenses can vary significantly.

[i] Based on an increase in demand and volume.

[j] Cost for pure Zr metal; electronic quality ZrO_2 costs $7/kg.
Unit cost of $2100/kg is used for isotopically tailored Zr (Sec. 10).

[k] Cost for pure Li metal; electronic quality LiOH costs are $4/kg.

8.2.5.3. External piping costs

Given the scope of the ARIES-I study, a detailed design of the external piping between the FPC and the heat exchanger (HX) was not drawn up. However, it should be noted that external piping (away from the neutron environment) will most likely be made from much cheaper, and possibly stronger, ceramic-composite materials. The most likely candidate for carrying the helium from the FPC to the HX and back will be C/C composite. This material surpasses SiC composite in strength, operating temperature, and commercial availability. Away from a neutron environment, the primary problem for C/C composites is oxidation. Helium as a coolant will not react with C/C composites; however, oxidation-resistant coatings will be needed on the outside of the pipes. For the relatively low helium temperature of 650 °C, finding a suitable coating is not an issue and, since it will be on the outside of the coolant pipes, simple high-temperature paint could suffice. The issue of helium-gas leak tightness, however, needs to be addressed since composites are inherently porous structures. A 1- to 2-mm-thick CVD carbon layer on the inside and/or outside of the coolant-carrying pipes wil be required.

The primary incentive for using C/C composites is the low cost. Commercial manufacturers of C/C composites [98] have quoted prices ranging from \$100 to \$1000/kg, depending on the complexity of the weave. For pipes, inexpensive 3-D braiding techniques are fully developed. The length required is assumed to be 32 modules $\times$ the periphery of the tokamak + 1000 m to and from the HX, for a total pipe length of about 3000 m. Taking the average diameter to be 0.4 m and a wall thickness of about 0.02 m to carry helium at 10-MPa pressure (designing to a hoop stress of about 100 MPa), the total amount of C/C composite piping required is about 137 tonne. At \$200/kg, this would result in a cost of about \$27 M for external piping.

8.3. MECHANICAL DESIGN

In this section, the configuration of the ARIES-I fusion power core (Sec. 8.3.1) and thermostructural analyses of the first wall and blanket (Secs. 8.3.2 and 8.3.3, respectively) are described.

8.3.1. Configuration

Configuration selection is a critical task in any tokamak blanket design since it directly impacts the blanket neutronics, thermal-hydraulic performance, structural design, and

maintenance. This task is even more difficult when the structural material is an SiC composite (high-temperature capability but poor thermal conductivity) and the coolant is high pressure helium (poor volumetric heat capacity). When metallic structure is used, the conventional design configurations of a helium cooled blanket are those of a poloidal, pressurized module with either toroidal or poloidal coolant flow [99]. Because of its design simplicity, such a poloidal flow design (Fig. 8.1-4) was investigated for ARIES-I. In order to optimize the coolant outlet temperature of 650 °C, a re-entrant coolant-flow design was used. This led to high coolant velocities, high first-wall and blanket pressure drop of 320 kPa, and a correspondingly high blanket-coolant pumping power of 154 MW. Because of the high pressure drop and high pumping power, this configuration was not selected. Instead, the coolant pressure was raised to 10 MPa and a radial/toroidal flow configuration was adopted, resulting in an order of magnitude reduction in the blanket pumping power.

The selected ARIES-I blanket design uses SiC composite as the structural material, 10-MPa helium as the coolant, Li_2ZrO_3 as the solid tritium breeder, and beryllium-metal sphere-pac pellets as the neutron multiplier. The blanket is segmented toroidally into 32 inboard and 32 outboard poloidal modules, as shown in Fig. 8.1-2. Each poloidal module comprises 17 nested, U-shaped, SiC-composite shells with solid-breeder and Be neutron-multiplier mixture (sphere pac) located between the shells (Figs. 8.1-5 and 8.1-6). The cylindrical helium-coolant channels are embedded in each of the 17 SiC-composite shells. Because the coolant is contained in small diameter (0.5 to 0.8 cm) tubes, high coolant pressure (10 MPa) can be used with thin walled tubes. As shown in Fig. 8.1-5, the helium coolant enters the blanket from the inlet plena, which are located in the shield behind the blanket and reflector. It then flows radially inward through the shells. It cools the shells while flowing in the toroidal direction before it turns and flows radially back into the coolant outlet plena. This routing configuration was selected to provide adequate cooling of the blanket materials and to minimize the blanket pressure drop. The maximum blanket pressure drop of 22 kPa is at the first wall. The corresponding total blanket internal- and external-loop pumping power is 19 MW.

Layers of solid-breeder and Be sphere-pac mixture are located right behind the first wall to give the best design for neutronics and heat transfer. This arrangement allows a decrease in volumetric power generation and an increase in effective thermal conductivity over pure solid breeder. Subsequently, a minimum breeder-zone thickness of 1.1 cm is possible, while at the same time providing an adequate tritium breeding ratio of 1.23. Neutronics and thermal-hydraulic designs are presented in detail in Secs. 8.4 and 8.5, respectively.

The blanket is configured in the form of nested shells because it is perceived to be advantageous to manufacture such a configuration and because of improved reliability. Figure 8.1-6 shows that preformed U-shaped shells can be fitted, one layer after another including internal supports as needed, into the grooves of the reflector and plenum assembly to form the poloidal module. The outer shell is the first wall. Thermal and structural analyses of the first wall and blanket were performed. It was found that the peak combined thermal-plus-pressure stress is 77 MPa, which is well below the 140 MPa design limit (Sec. 8.3.2).

Based on neutronics, thermal-hydraulic, and structural analyses, and the relative simplicity of fabrication, this nested-shell design is found to be a suitable configuration for the ARIES-I helium-cooled, SiC-composite, solid-breeder design.

8.3.2. First-Wall Thermal and Structural Analyses

In order to achieve the desired performance, the ARIES-I first wall must operate below maximum-allowable design criteria, as described in Sec. 8.2.1.6 (*i.e.*, a primary stress of 140 MPa, a secondary stress of 190 MPa, and a temperature of $\sim$1100 °C). The steady-state temperatures and stresses in the first wall were calculated using ANSYS [100], a widely used finite-element code. Because of the toroidal geometry of the first wall, a complete finite-element model is costly to construct, so an approximate 2-D model was used to study the response of the first wall to maximum loading conditions. The critical location for the first wall would be at the mid-plane where, because of peaking, the maximum surface heat flux is expected to occur. The peak heat flux at this location is 0.55 MW/m^2. (In the final design, the peak heat flux is 0.61 MW/m^2, which will not impact the conclusions reached in this section.) This portion of the first wall was analysed by modeling three tubes in order to study the effects of neighboring channels. The model, shown in Fig. 8.3-1(A), consists of 636 quadrilateral elements. The material properties that are used in the analysis are given in Table 8.2-IV.

The first-wall coolant channels run radially from the back of the outboard blanket module towards the center of the tokamak, turn and run toroidally for about 1.7 m, and then return towards the back of the blanket (see Fig. 8.1-5). The ARIES-I first-wall coolant-channel wall thickness is 1 mm with an additional 2-mm-thick CVD layer of SiC facing the plasma. This layer provides a highly dense barrier to coolant leaks; it also serves as a sacrificial layer for first-wall sputtering. The 1.7-m-long toroidal run of the coolant channel constitutes the first wall of a blanket module. Since the bulk coolant temperature and the internal coolant pressure change toroidally, mechanical and

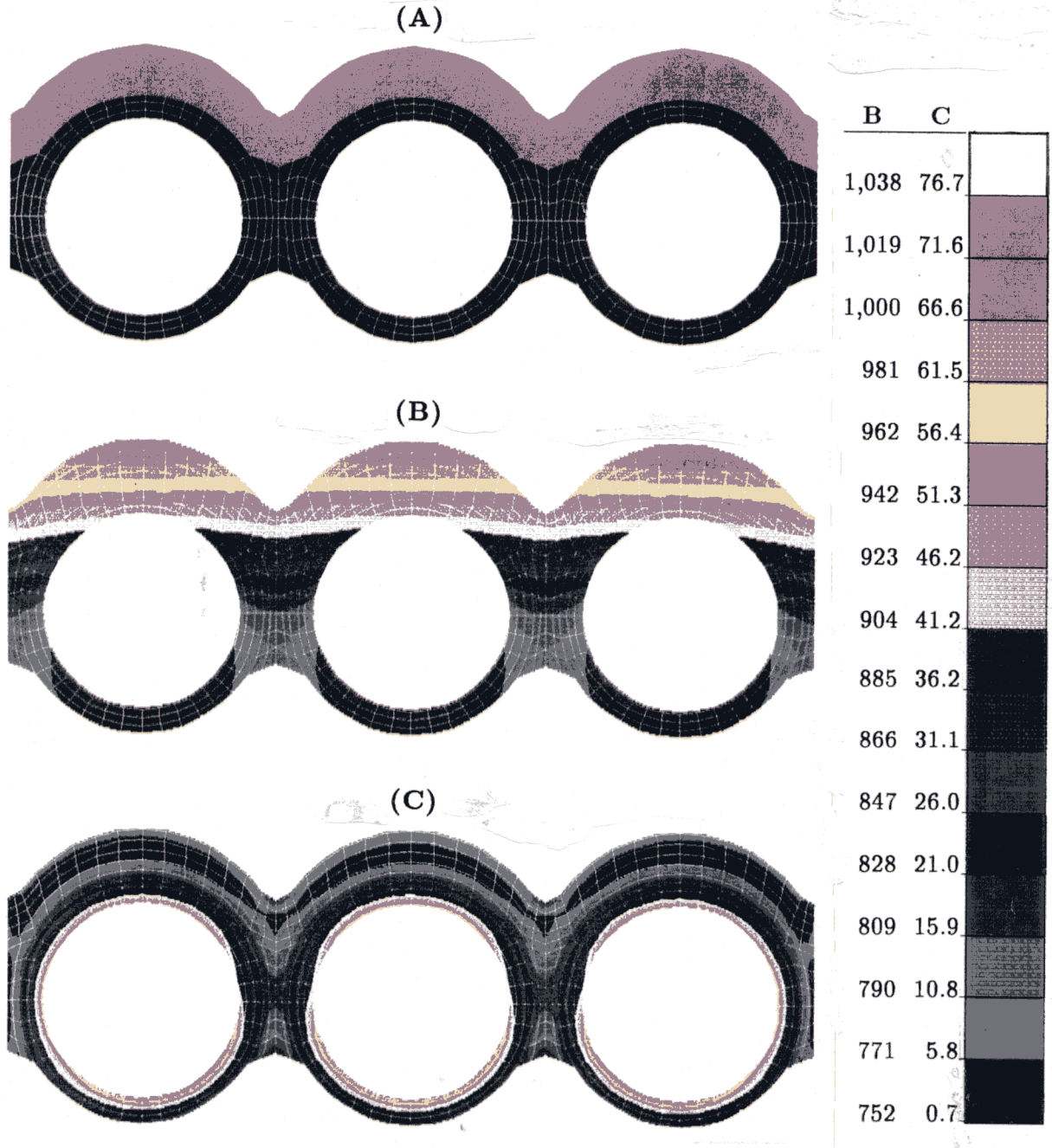

Figure 8.3-1. (A) Finite-element model for thermostructural analysis of the ARIES-I first wall (red is CVD SiC; black is SiC composite); (B) Temperature contours (°C) in the SiC-composite first wall for a surface heat flux of 0.55 MW/m^2 at beginning of life; and (C) Combined thermal-plus-pressure stress contours (MPa) in the SiC-composite first-wall section for a surface heat flux of 0.55 MW/m^2 and coolant pressure of 10 MPa at beginning of life. (A 2-mm-thick CVD sacrificial sputtering layer faces the plasma.)

thermal fields caused by the loading conditions have small gradients in the poloidal and toroidal directions. However, the thermomechanical effect of this dependence on the first wall is small. Therefore, stresses perpendicular to the plane of the cross section will not change significantly in the toroidal direction and, therefore, a 2-D model at the location of maximum loading conditions is adequate.

8.3.2.1. Thermal analysis

The heat flux on the first wall was assumed to be constant at 0.55 MW/m^2. Heat transfer into the coolant was modeled assuming a constant heat-transfer coefficient of 2.2 $kW/K\text{-}m^2$ inside the first-wall channels. On the blanket side of the first wall, a constant heat-transfer coefficient of 0.6 $kW/K\text{-}m^2$ was assumed and all other surfaces were assumed to be adiabatic. The coolant-channel bulk-coolant temperature at this point is $\sim$650 °C. A surface heat load of 0.17 MW/m^2 was used on the blanket side of the first-wall coolant channels to allow for the back flow of heat from the blanket into the first wall. A constant volumetric heating rate of 23 MW/m^3 was assumed for all of the elements in the model.

Figure 8.3-1(B) shows the temperature contours for this model. The temperature distribution in the CVD SiC layer facing the plasma is approximately one dimensional and little conduction to the rear of the tube is observed. The peak temperatures are 1040 °C in the CVD layer and $\sim$960 °C in the SiC composite structure. Each of these values is below the allowable limit of 1100 °C.

8.3.2.2. Thermal and pressure stresses

Because relevant uniaxial stress measures are not yet available for composites, the von Mises stress is used to indicate equivalent thermal-stress levels. The peak thermal stress of $\sim$44 MPa is located towards the blanket side of the first wall. This is due primarily to the asymmetric heating of the first-wall coolant channels, and is further underlined by the presence of the relatively thick CVD layer in front of the first wall. The peak thermal stress of 44 MPa is well below the estimated maximum-allowable secondary stress of 190 MPa. The combined thermal-plus-pressure stress contours induced by the 10-MPa coolant are shown in Fig. 8.3-1(C). Note that the pressure stress calculations are conservative because the pressure will be significantly lower than 10 MPa at that location of the first wall. Nevertheless, the combined thermal-plus-pressure stress peak of 77 MPa is well below the maximum-allowable pressure-stress limit of 140 MPa.

8.3.2.3. Global deformation

Using the finite-element model, deformations of the order of 0.04 mm in the poloidal direction were calculated. This deformation assumes that the first wall is free to expand poloidally. If the entire first wall were to be exposed to the same surface heat flux as the modeled section, the global deformation would be on the order of ~2.5 cm in the poloidal direction for the entire first wall. Such deformations are readily absorbed by properly designed floating headers. Note that these results are only meant to indicate the severity of thermal deformations. An accurate deformation profile would require modeling the first wall in its entirety in both the toroidal and poloidal directions and would include the effects of variable thermal and pressure loads.

8.3.2.4. Thermomechanical analysis at end of life

To estimate thermomechanical response of the first wall at the end of life (EOL), geometric and material property changes need to be included. For ARIES-I, EOL is defined as ~18 MWy/m^2 of neutron exposure. From a structural point of view, the 2-mm-thick CVD SiC layer facing the plasma has been sputtered away at EOL. The first-wall EOL geometry assumes a complete removal of the 2-mm-thick CVD SiC layer, thus exposing the SiC composite material directly to the plasma. The degradation of properties was incorporated by choosing conservatively low values for thermal conductivity, matrix and fiber strengths, and a 10% matrix-void fraction for the SiC composite. Although these properties may not adequately reflect EOL characteristics of SiC composites, lack of a data base prohibits further extrapolations. Using the finite-element analysis outlined above, the EOL analysis shows a maximum SiC-composite temperature of about 960 °C, and a maximum thermal stress of about 25 MPa. Maximum thermal-plus-pressure stress is about 69 MPa. The above analysis indicates that even with the loss of the 2-mm-thick CVD layer, the thermomechanical response of the first wall stays well below the allowable design limits.

It should be noted that the CVD layer provides a leakage barrier. During the course of the ARIES-I design study, several options for a renewable layer were investigated briefly. For SiC, the most likely method would be to plasma spray the inside of the vacuum chamber by remote control. Although automated plasma spraying of ceramics has been demonstrated successfully, the resultant structure may not have adequate gas leak tightness.

8.3.3. Blanket Structural Analysis

The blanket module consists of 17 nested layers of channel walls (Sec. 8.3). Of concern are the major bending stresses on the outer blanket module shell (*i.e.*, the first wall). The inside of the blanket is pressurized with a 0.4-MPa helium-purge stream and the first-wall dimensions are approximately 1.7 m $\times$ 6 m. Thus, the bending moments on an unsupported first wall will be unacceptably high. In order to lower the bending stresses on the first wall to acceptable levels, the choice was made to use tie rods to connect the first wall to the back of the blanket module.

The tie rods are SiC composite with (mostly) axially running SiC fibers. With the majority of the fibers running parallel to the load direction, 1-mm-diameter rods are sufficiently strong, given that degraded SiC-yarn tensile strengths are estimated to be around 370 MPa. To model the approximate pitch between tie rods, simple bending-stress equations were used to estimate the minimum square pitch that would be necessary for the support rods. With 10 cm between tie rods, the maximum bending stress on the first wall is about 55 MPa. However, reducing the distance to 5 cm decreases the bending stress to 14 MPa so this spacing is chosen. Although the bending stress is added to the local stresses in the first wall, the maximum thermal-plus-pressure stress is not more than 77 MPa so an additional 14 MPa will not surpass the maximum-allowable design stress limit of 140 MPa. In case of a tie-rod failure, the maximum bending stress could increase to about 55 MPa, which is still below the maximum-allowable design stress limit when combined with the 77-MPa maximum-allowable stress in the first wall. These simple calculations are intended only to scope the feasibility of using SiC composites as structural material for the ARIES-I reactor. A full-scale thermomechanical calculation of the first-wall and blanket module would require a 3-D model analysis, which is beyond the scope of this study.

8.4. NEUTRONICS AND ACTIVATION

The level of activation (and specific radioactive isotopes) in the first wall and blanket depends entirely on material selection, which can cause differences of many orders of magnitude. The goals of the ARIES-I reactor design study are to maximize the safety attributes and to minimize the environmental impact of the reactor. As such, the ARIES-I team has paid particular attention to the following:

- **Safety**. Safety, the most important concern in developing a reactor concept, is generally related to the radioactive inventories and the potential for their release.

The design approach for the ARIES-I blanket is to minimize the production of radiologically hazardous materials and decay afterheat, which is the main source of energy driving the first wall and blanket above their melting temperatures during accidents.

- **Normal operation and decommissioning.** During normal operation and under accident conditions, the protection of working personnel from radiation exposure is very important. Minimizing the radioactive inventory in the ARIES-I design will help achieve the goal of "as low as reasonably achievable" exposure during normal operation and decommissioning.

- **Nuclear waste disposal and reuse of materials.** Shallow-land burial (10CFR61, Class C or better) waste disposal is desirable for fusion reactors. In some cases, recycling resource-limited materials should also be made possible. These goals are achievable if the long-lived radioactive inventory is minimized.

A comparative neutronics study of blanket concepts was performed for the ARIES-I reactor. The tritium breeders considered in the gas cooled systems included Li_2O, $LiA\ell O_2$, Li_4SiO_4, and Li_2ZrO_3. Lithium aluminate was rejected because it produces a high level of long-lived radionuclide, $^{26}A\ell$ (half-life of 7.2×10^5 y), which requires handling of high-level radioactive waste for disposal. We found that SiC, Be, and Li_4SiO_4 is a suitable combination that is capable of achieving the low-activation goals of the ARIES-I reactor design and also results in a blanket with a high nuclear performance [101, 102]. However, because of the lack of experimental data base for Li_4SiO_4 and the potential concern of radiation effects, Li_2ZrO_3 is chosen as the reference solid breeder for the ARIES-I design. Unfortunately, the activation level and waste disposal concerns will increase because of its use (Sec. 10).

Using a neutron-multiplier material increases the nuclear performance of the blanket, a desirable improvement for any fusion reactor. Neutron-multiplier material is also needed to achieve an adequate tritium breeding ratio (TBR) in almost all solid-breeder blanket configurations (a combination of SiC structure and Li_2O breeder is an exception). The only low-activation neutron-multiplier material is beryllium. Lead is the other possible non-fissionable neutron multiplier. However, the radiological hazard potential for lead in a fusion reactor is at least four orders of magnitude higher than for SiC or Be.

The best approach for effective utilization of the beryllium neutron multiplier is to locate the Be immediately behind the first wall and to maximize the Be fraction in this zone. To enhance the nuclear energy multiplication in the ARIES-I blanket, we

also allow the excess neutrons to be absorbed in silicon ($Q = 8.5$ MeV), the constituent element in the SiC structural material. On the other hand, for the solid-breeder designs, the power density in the breeder zone should not be so high that the maximum operating temperature in the breeder exceeds the design limit. For these reasons, the ARIES-I reference design places a Be neutron-multiplying zone immediately behind the first wall and the tritium solid breeder is uniformly mixed with Be to reduce the operating power density. However, high ^{6}Li enrichment in the solid-breeder compound will be needed because of high ^{6}Li burnup in the blanket.

Table 8.4-I shows the zones and the material composition of the ARIES-I blanket and shield. The neutronics model used in the calculation assumes a 1-cm-thick first wall composed of 67% SiC and 33% helium (in this section fractions are all by volume). In front of the first wall, there is a 2-mm-thick SiC sacrificial layer (to account for particle erosion). The breeding zone is located immediately behind the first wall, is 20 cm thick, and comprises 25% SiC, 70% breeder/multiplier mixture, and 5% helium. The composition of the breeder/multiplier is 20% solid breeder and 80% Be. Both the solid breeder and the Be have 90% of their respective theoretical densities. The packing fraction of the breeder and Be in this zone is 80% using two particle sizes. Figure 8.4-1 displays the TBR, the blanket energy multiplication, M, and the ^{9}Be (n,2n) reaction rate as functions of breeder/multiplier zone thickness. The 0.2-m breeder/multiplier zone thickness was chosen based on the considerations of adequate breeding (1.2 in 1-D calculation) and minimum Be inventory.

Two reflector zones are located behind the breeder/multiplier zones. The front reflector zone is 0.1-m thick and comprises 25% SiC, 70% Be, and 5% He. The use of Be in this reflecting zone is primarily to enhance the blanket energy multiplication ($\sim$3% in ARIES-I). The rear reflecting zone comprises 25% SiC (structure), 50% SiC (particles), and 25% He. The thickness of this SiC reflector zone in the inboard location is 0.07 m, otherwise it is 0.37 m. Note that the nonstructural material in the reflector zones, either Be or SiC, is 90% dense and is with 80% packing fraction using two particle sizes. Figure 8.4-2 displays TBR and M as functions of the packing fraction of the Li_2ZrO_3/Be particles. Note that the corresponding TBR will change by about 7% when the packing fraction of these breeder/multiplier particles varies by 10%, as shown in the figure. The blanket energy multiplication, however, is affected by only about 2%.

The SiC reflector zone is followed by a 0.3-m-thick gas plenum composed of 75% SiC and 25% He. For the neutronics analysis, a 10-mm-thick vacuum vessel, which is made of low-activation aluminum alloy, is assumed to be located outside of the gas plenum. In the final design, the vacuum vessel is located outside the shield, and 40 1-mm-thick Aℓ

Table 8.4-I.
The ARIES-I Reference Blanket

Zone	Thickness (cm)	Composition
First wall		
Sacrificial layer	0.2	100% SiC
Structural wall	1	67% SiC + 33% He
Breeding zone[a,b]	20	25% SiC + 70% breeder/multiplier + 5% He
Reflector 1[b]	10	25% SiC + 70% Be + 5% He
Reflector 2[b]		
Outboard	37	75% SiC + 20% void + 5% He
Inboard	7	75% SiC + 20% void + 5% He
Plenum	30	75% SiC + 25% He
Vacuum vessel[c]	1	Aℓ alloy
Shield 1		
Outboard	40	66.5% SiC + 28.5% B_4C + 5% He
Inboard	40	56.0% SiC + 24.0% B_4C + 20% He
Shield 2		
Outboard	40	66.5% SiC + 28.5% B_4C + 5% He
Inboard	30	66.5% SiC + 28.5% B_4C + 5% He

[a] Breeder/multiplier mixture is 20% breeder and 80% Be; the reference breeder is Li_2ZrO_3.

[b] Breeder and Be have 90% of theoretical density and a packing factor of 80% (density factor of 72%).

[c] In the final blanket design, the vacuum vessel is located outside the shields.

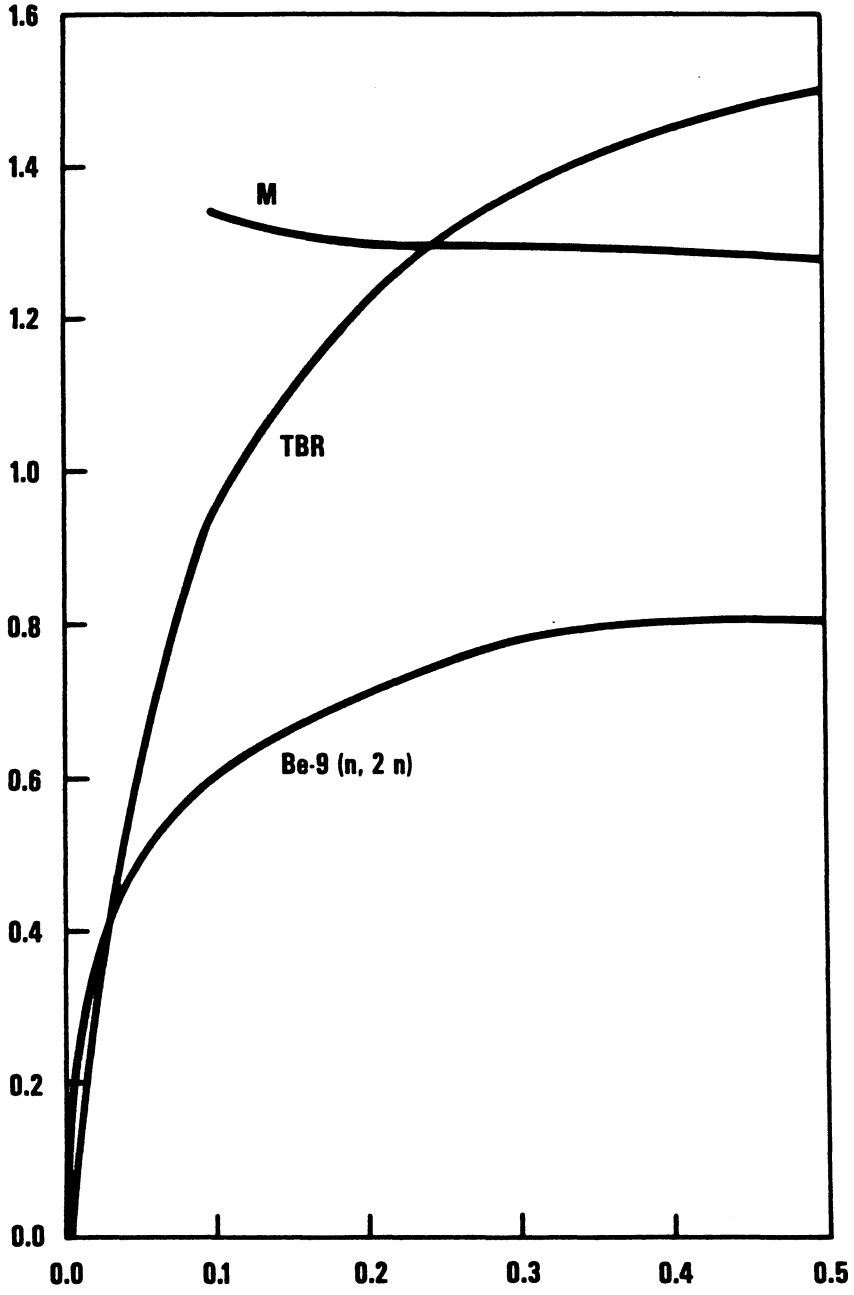

J-456(2)
3-21-90

Figure 8.4-1. Tritium breeding ratio (TBR), blanket energy multiplication, M, and Be (n,2n) reaction rate as functions of breeder (Li_2ZrO_3)/multiplier (Be) zone thickness in ARIES-I reference blanket.

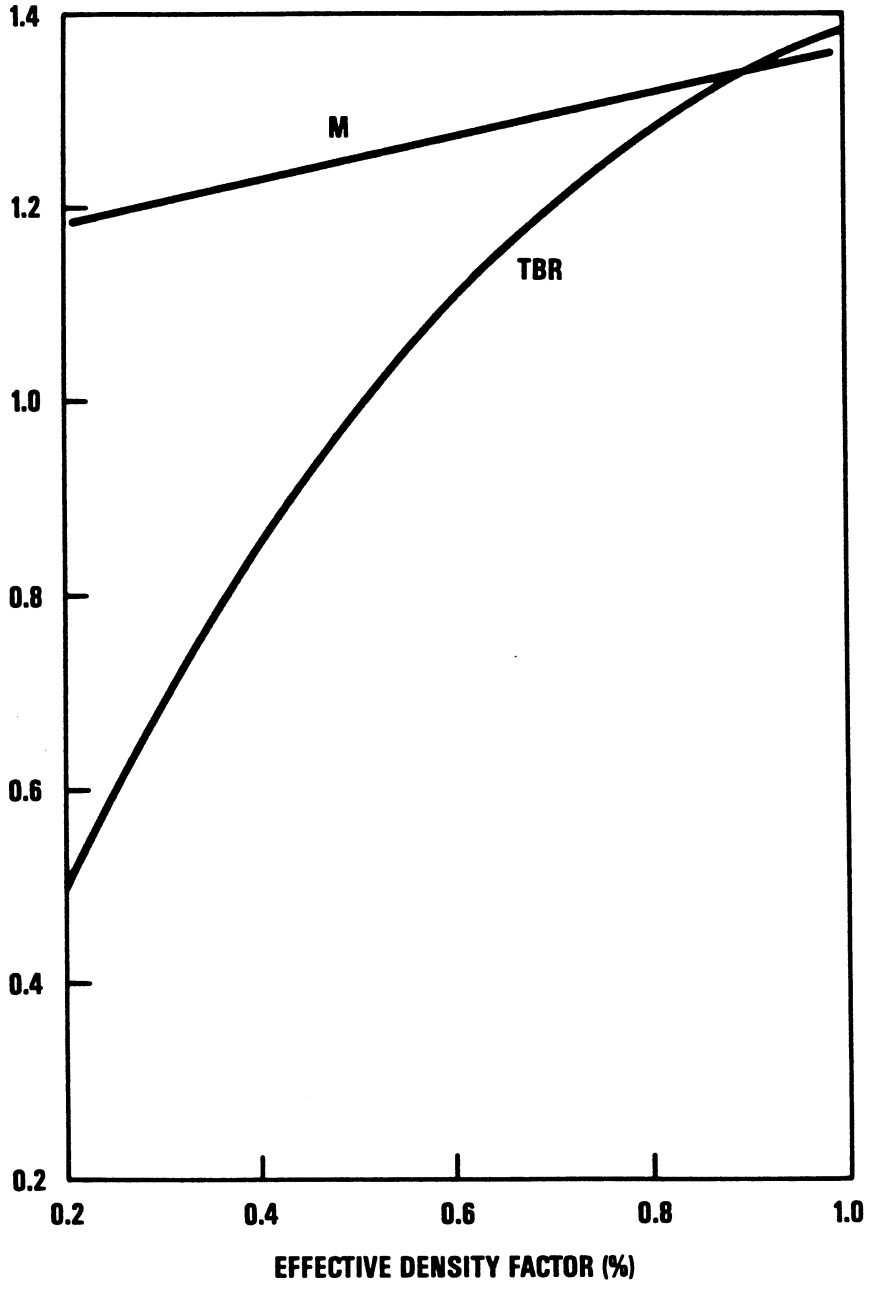

J-456(3)
3-21-90

Figure 8.4-2. Tritium breeding ratio (TBR) and blanket energy multiplication, M, as functions of packing fraction of breeder (Li_2ZrO_3)/multiplier (Be) particles in the ARIES-I blanket.

sheets are sandwiched between SiC plates in the shield. This difference, however, is not expected to cause any appreciable changes in the neutronics analysis.

The magnet shield is located behind the blanket to protect the superconducting magnet. For the ARIES-I reactor, the inboard shield is 0.7-m thick. The 0.3-m region closest to the magnet uses a high density shield consisting of a 95% SiC/B_4C mixture (respectively, 70% and 30%) and 5% He. The 0.4 m of shield close to the blanket vessel is made of low-density shield particles. The packing fraction of these variable-size SiC and B_4C particles is 80%, which allows the particles to be extracted to create extra space behind the vacuum vessel when the vessel is to be disassembled. (This shield arrangement, however, should be reversed when the vacuum vessel is outside the shield, as it is for the final ARIES-I blanket design.) The shield elsewhere is designed to be 0.8-m thick and is made of high-density shield materials. The shield is cooled by low-temperature helium.

The total blanket thickness for the inboard location is 0.7 m, while it is 1.0 m elsewhere. The overall blanket and shield thickness for the inboard location is 1.4 m, and 1.8 m elsewhere. The inboard blanket and shield are capable of protecting the superconducting magnet against radiation damage throughout the lifetime of the ARIES-I power plant. In addition to protecting the magnet, the 1.8-m thickness elsewhere is designed to reduce the activation level of the reactor materials behind the blanket and shield component such that hands-on maintenance may be possible behind the shield.

Table 8.4-II displays the neutronics performance of the ARIES-I blanket and shield. The ^6Li enrichment in the Li_2ZrO_3 solid breeder is 80% at the blanket beginning of life. At the end of life (after 20-MWy/m^2 neutron fluence), the ^6Li enrichment is reduced to 20%. Figure 8.4-3 shows the TBR and M as functions of ^6Li enrichment in the breeder. The TBR for ARIES-I from a 1-D full-coverage analysis is 1.21 at the beginning of life and is reduced by 5.6% to 1.15 at the end of life. The average TBR over the blanket life is 1.18, which is more than enough to guarantee adequate tritium production in a realistic 3-D geometry that includes allowance for the divertors. The blanket energy multiplication is initially 1.30, and then increases slightly to 1.32 at the blanket end of life.

Figure 8.4-4 depicts the distribution of volumetric nuclear-heating rates which are normalized to 1 MW/m^2 of neutron wall loading. The maximum volumetric nuclear heating of 11 MW/m^3 occurs at the breeder zone immediately behind the SiC first wall. However, the volumetric nuclear heating at the SiC first wall is only 6.7 MW/m^3. At the inboard region of the superconducting magnets, the maximum nuclear heating rate is $\sim$370 W/m^3 and the fast neutron (energy above 0.1 MeV) flux is 2.3×10^{13} n/m^2-s (also normalized to 1 MW/m^2 of wall loading). The superconducting magnet is more

Table 8.4-II.
Neutronics Performance of the ARIES-I Blanket and Shield

	Beginning of Life[a]	End of Life[b]
Tritium breeding (T/DT neutron)		
^{6}Li (n,α)T	1.1994	1.1337
^{7}Li (n,n'α)T	0.0036	0.036
Be (n,T)	0.0112	0.0114
Neutron multiplication (reactions/DT neutron)		
Be (n,2n)	0.7516	0.7643
Nuclear heating (MeV/DT neutron)		
First wall	0.8375	0.8449
Breeder zone	13.35	13.06
Be reflector	1.317	1.413
SiC reflector	2.284	2.651
Plenum	0.5495	0.6345
Total blanket heating	18.34	18.60
Blanket energy multiplication	1.30	1.32
Maximum nuclear heating rate (MW/m^3)[c]		
SiC first wall	6.7	
Breeder/multiplier mixture average	11.0	
At superconducting magnet (inboard)		
Maximum nuclear heating (W/m^3)[c]	370	
Maximum fast neutron flux (n/m^2-s)[c]	2.3×10^{13}	

[a]Beginning of life: 0 MWy/m^2, 80% ^{6}Li.

[b]End of life: 20 MWy/m^2, 20% ^{6}Li.

[c]Normalized to 1 MW/m^2 of neutron wall loading.

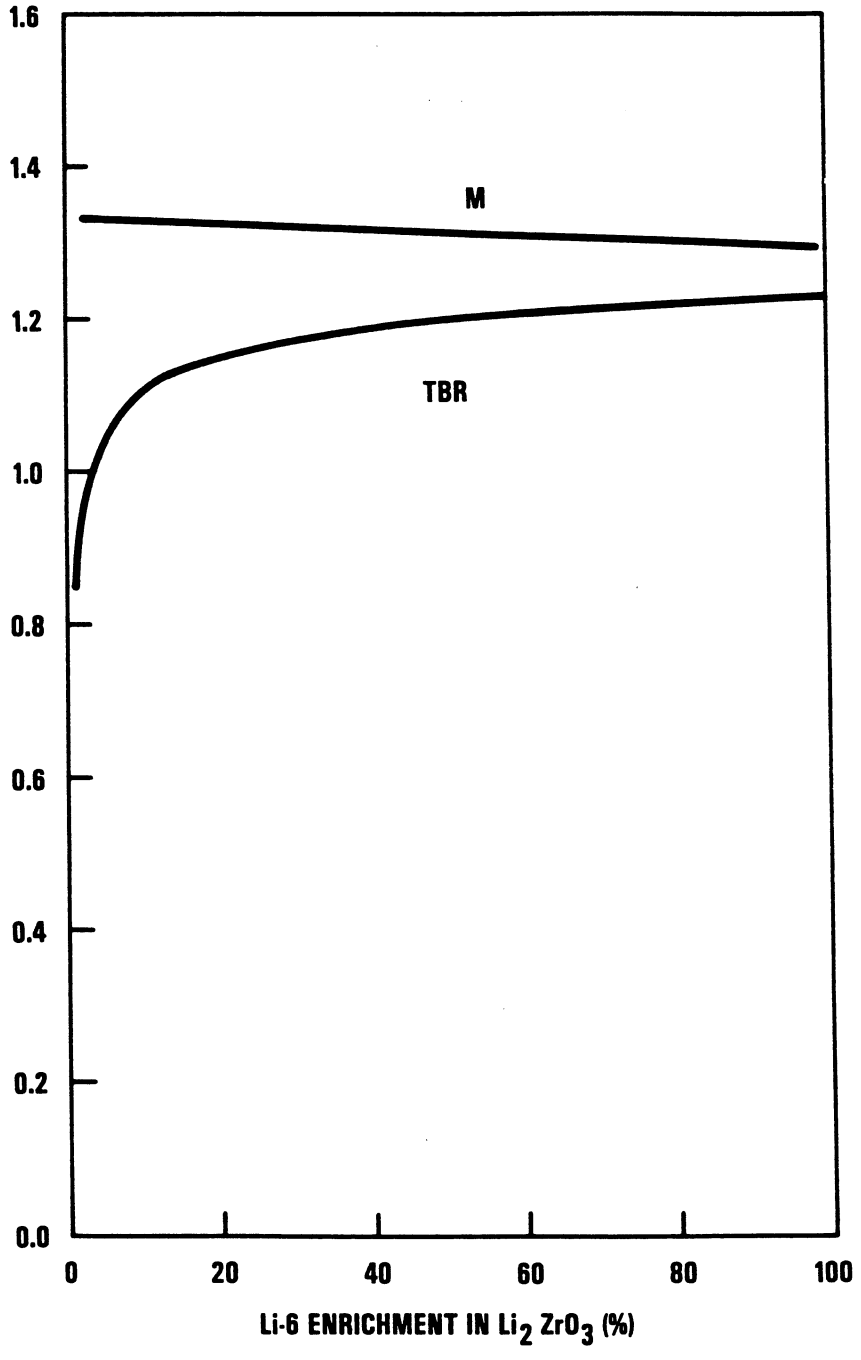

Figure 8.4-3. Tritium breeding ratio (TBR) and blanket energy multiplication, M, as functions of ^{6}Li enrichment in Li_2ZrO_3 breeder in the ARIES-I blanket.

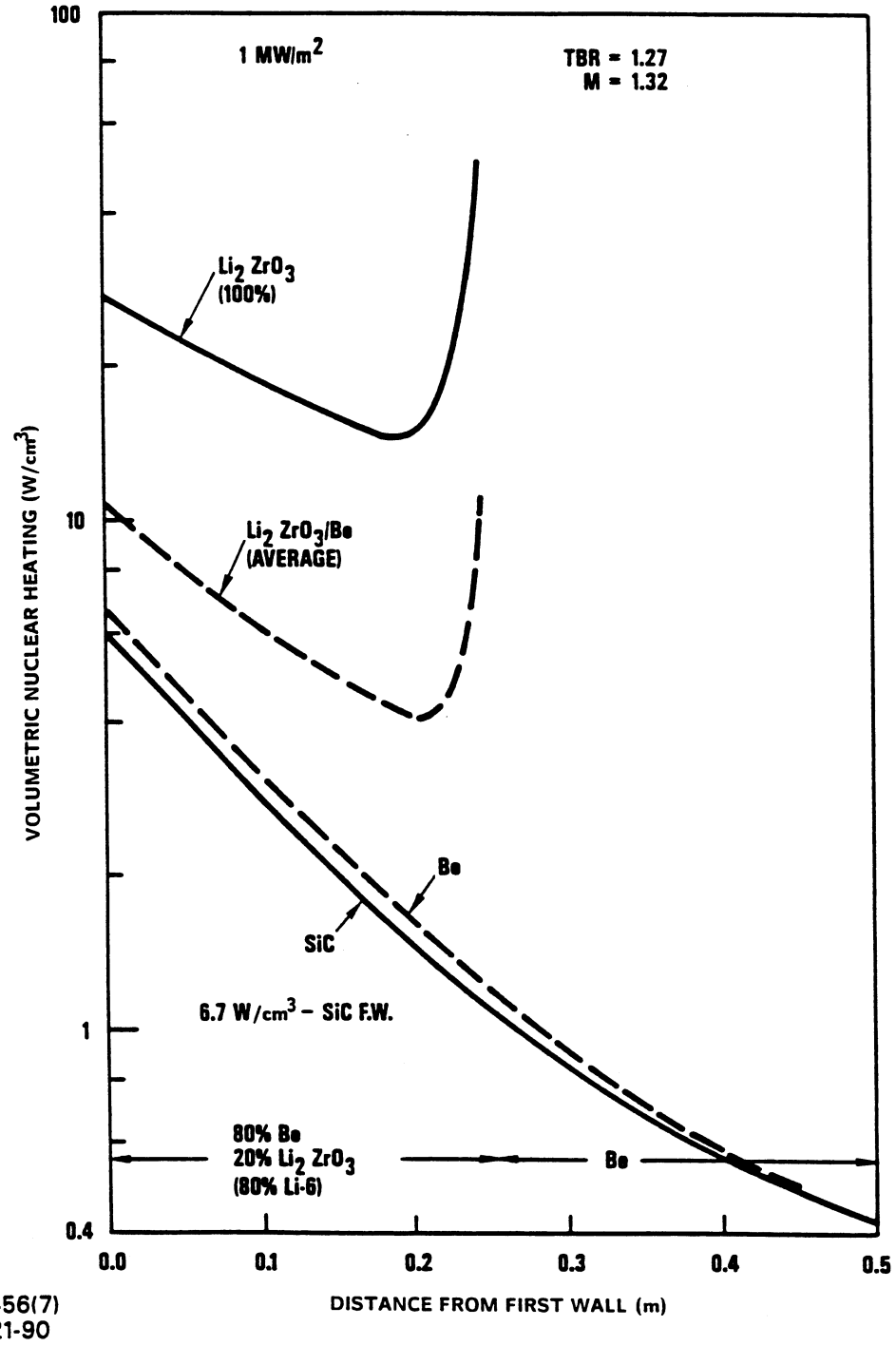

Figure 8.4-4. Spatial distribution of volumetric nuclear-heating rates in the ARIES-I fusion power core (normalized to 1-MW/m^2 neutron wall loading).

than capable of operating continuously for 40 full power years since the radiation damage limit is believed to be 1.0×10^{23} n/m^2 fast neutron fluence and the neutron wall loading at the inboard region is 2.4 MW/m^2.

8.5. THERMAL ANALYSIS

8.5.1. Thermal Hydraulics

In order to optimize the thermal efficiency of the blanket system, thermal-hydraulic analysis was closely coupled with materials selection and with the structural, mechanical, and neutronics designs. This was especially true during the concept evaluation phase of the ARIES-I study. During this phase, the thermal-hydraulic designs of several different blanket concepts were studied. These included the FLiBe loop design, the 0.5-MPa CO_2-gas and solid-particulate mixture design, the 5-MPa helium-cooled poloidal-flow design, and the 10-MPa helium-cooled nested-shell design (Sec. 8.1 and Figs. 8.1-1 through 8.1-6).

The reference ARIES-I blanket is shown in Figs. 8.1-5 and 8.1-6. The blanket is configured in the form of nested SiC-composite shells in which small coolant channels (0.5- to 0.8-cm diam) are embedded. The helium coolant enters the blanket from the inlet plenum, which is located between the reflector and the shield. Coolant then flows radially inward towards the first wall. It cools the first wall while flowing in the toroidal direction before it turns and flows radially outward away from the first wall into the coolant outlet plenum. This coolant routing configuration was selected to provide adequate cooling of the blanket materials and to minimize the blanket pressure drop. In order to maintain the breeder and Be within their material temperature limits, it was necessary to minimize the maximum local power density. The solid breeder is mixed with the Be in order to reduce the effective power density and to increase the effective thermal conductivity of the mixture. A detailed estimate of the thermal conductivity of the sphere-pac mixture was performed (Sec. 8.5.2) and the results were used in the heat transfer calculations. For the sphere-pacs of the breeder/multiplier mixture and of the Be (in the reflector zone), the estimated effective thermal conductivities are, respectively, 4.6 and 7.3 W/K-m. Thermal-hydraulic design inputs are presented in Table 8.5-I.

Including the first wall, there are 17 nested shells that have built-in coolant channels. Table 8.5-II shows the detailed configuration at the mid-plane location of the blanket where the neutron and surface wall loadings are at their maximum values of, respectively,

Table 8.5-I.
Thermal-Hydraulic-Design Input Parameters

Reactor geometry	
Major toroidal radius, R (m)	6.55
Minor plasma radius, a (m)	1.5
First wall area (m^2)	711
Module width[a] (m)	1.76
Module height (m)	
Outboard	7.0
Inboard[b]	8.5
Number of modules[a]	32
First-wall circular tube diameter (m)	
At mid-plane	0.008
At top and bottom of the module	0.0065
Material	
Structure	SiC composite
Breeder (sphere-pac)	Li_2ZrO_3[c]
Multiplier (sphere-pac)	Be-metal
Reflector	SiC
Coolant	He (10 MPa)
Inlet temperature (°C)	350
Outlet temperature (°C)	650

[a]Same for inboard and outboard.

[b]Covering the back of divertors.

[c]Mixed with Be.

Table 8.5-I Cont'd

Property inputs	
SiC thermal conductivity (W/K-m)	10
Breeder packed-bed effective thermal conductivity (W/K-m)	4.6
Packed-bed and surface-contact heat-transfer coefficient[a] (W/K-m^2)	6,649
Large sphere-pac particle size (mm)	1.0
Small sphere-pac particle size (mm)	0.1
First-wall minimum structural thickness (m)	0.001
First-wall CVD erosion-layer thickness (m)	0.002
Channel wall thickness (m)	0.001
Channel path length (m)	3.36
Fusion power (MW)	1963
Blanket multiplication ratio	1.3
Neutron wall loading (MW/m^2)	
Average[a]	2.207
Maximum[b]	3.340
Surface heat flux (MW/m^2)	
Average[a]	0.353
Maximum[b]	0.553
Maximum nuclear-heating rate (MW/m^3)	
First wall (SiC)	23.38
Breeder/multiplier	28.9

[a] At top and bottom of the outboard poloidal module.

[b] At mid-plane.

[c] Gas conductivity and small particle radius.

Table 8.5-II.
Outboard First-Wall and Breeder Shell Geometry

	No. of Shells	Minimum Solid Zone Thickness (cm)	Thermal Power Fraction	Radial Thickness (cm)	Volume Fractions (100% dense material) SiC Shell	Void	Solid
Mid-plane location[a]							
First wall	1		0.185	1.2	0.50	0.50	
Breeder/multiplier							
Zone 1	2	1.1	0.160	4.	0.24	0.26	0.50
Zone 2	3	1.1	0.167	6.	0.24	0.24	0.52
Zone 3	5	1.1	0.271	10.	0.24	0.23	0.53
Beryllium reflector	2	4.1	0.064	10.	0.10	0.27	0.63
SiC reflector	4	8.6	0.15	38.	0.05	0.27	0.68
Reflector/plena				30.	0.75	0.25	
Top and bottom locations[b]							
First wall	1		0.185	1.05	0.57	0.43	
Breeder/multiplier							
Zone 1	2	1.2	0.160	4.	0.23	0.25	0.52
Zone 2	3	1.2	0.167	6.	0.23	0.24	0.53
Zone 3	5	1.2	0.271	10.	0.23	0.23	0.54
Beryllium reflector	2	4.2	0.064	10.	0.09	0.27	0.64
SiC reflector	4	8.7	0.15	38.	0.05	0.27	0.68
Reflector/plena				30.	0.75	0.25	

[a]First-wall channel diameter is 8 mm; shell channel diameter is 5 mm.

[b]First-wall channel diameter is 6.5 mm; shell channel diameter is 4 mm.

3.87 and 0.61 MW/m^2. Table 8.5-II also shows the detailed configuration at the top and bottom locations of the outboard blanket where the neutron and surface wall loadings are, respectively, 2.48 and 0.39 MW/m^2. The temperature distribution in the blanket was evaluated for six radial zones (Table 8.5-II). As indicated, the coolant channels have slightly different diameters at different vertical locations to allow for the poloidal variation of the neutron and surface wall loadings while maintaining similar pressure drops along the same blanket shell.

The volumetric power generation of the reference design was discussed in Sec. 8.4. Results of the thermal-hydraulic calculations of the ARIES-I outboard blanket are presented in Tables 8.5-III and 8.5-IV, respectively, at the mid-plane and at the top and bottom of the blanket modules. The first-wall maximum temperature is 1000 °C, less than the SiC design limit of 1100 °C. The Li_2ZrO_3 breeder has maximum temperatures of 908 and 933 °C occurring where the maximum volumetric power is generated, respectively, at the front and at the back of the blanket zone. This shows that the breeder material can be designed to within the recommended operational window of 400 to 1400 °C [8] for Li_2ZrO_3. The Be reflector zone can be designed to less than 900 °C. At the SiC reflector zone, the maximum SiC sphere-pac temperature is 1075 °C. These results should also be representative of the inboard blanket modules, which operate at somewhat lower wall load.

As shown in Figs. 8.1-5 and 8.1-6, the helium coolant enters the blanket from the inlet plenum which is located in the shield behind the blanket and reflector. It then flows radially inward towards the first wall. It cools the first wall while flowing in the toroidal direction before it turns and flows radially outward away from the first wall into the coolant outlet plenum. A schematic of the ARIES-I coolant path is given in Fig. 8.5-1. Table 8.5-V shows the estimated pressure drops in the outboard blanket including frictional losses, turns, and contractions and expansions. The total blanket pressure drop is 43.31 kPa. The external pressure drop through the steam heat exchanger and circulator is about 37.5 kPa [103]. Therefore the total blanket-loop internal and external pressure drop is 80.81 kPa. By assuming a similar pressure drop in the inboard blanket modules, the total pumping power is 17.1 MW. At a circulator efficiency of 90%, the blanket-loop pumping power is about 19 MWe.

8.5.2. Effective Thermal Conductivity of Packed Beds

Some of the many heterogeneous systems currently in use are packed beds and composite materials, foamed metals and glasses, emulsions, mixtures of solids in gases and

Table 8.5-III.
Thermal-Hydraulic Results
(outboard module, mid-plane location)[a]

	Velocity (m/s)	h (W/K-m^2)	Surface Temp (°C)	Maximum Temp (°C)	Pressure Drop (kPa)
First wall					
Inboard	19	2,088[b]	655	718	20.2
Mid-plane	24	2,153[b]	796	858	
Outboard	29	2,208[b]	938	1,000	
Breeder/Be, Zone 1					
Inboard	14	2,079	504	613	22.0
Mid-plane	17	2,145	654	764	
Outboard	20	2,208	798	908	
Breeder/Be, Zone 2					
Inboard	10	2,148	500	610	24.6
Mid-plane	12	2,219	650	795	
Outboard	14	2,280	795	938	
Breeder/Be, Zone 3					
Inboard	9	1,520	535	645	11.6
Mid-plane	11	1,571	685	745	
Outboard	14	1,613	828	938	
Beryllium reflector					
Inboard	5	997	458	570	4.62
Mid-plane	7	1,030	607	720	
Outboard	8	1,058	754	866	
SiC reflector					
Inboard	6	1,132	476	780	6.12
Mid-plane	8	1,170	625	929	
Outboard	9	1,202	770	1,075	

[a]First-wall channel diameter is 6.5 mm; shell channel diameter is 4 mm.

[b]20% reduction assumed due to non-symmetric surface heat flux (Sec. 8.7).

Table 8.5-IV.
Thermal-Hydraulic Results
(outboard module, top and bottom locations)[a]

	Velocity (m/s)	h (W/K-m^2)	Surface Temp (°C)	Maximum Temp (°C)	Pressure Drop (kPa)
First wall					
Inboard	16	1,891[b]	566	606	19.3
Mid-plane	20	1,950[b]	709	749	
Outboard	24	2,000[b]	854	894	
Breeder/Be, Zone 1					
Inboard	12	1,925	462	546	23.2
Mid-plane	14	1,986	612	696	
Outboard	27	2,000	759	843	
Breeder/Be, Zone 2					
Inboard	8	1,989	460	544	25.0
Mid-plane	10	2,055	610	694	
Outboard	12	2,111	756	839	
Breeder/Be, Zone 3					
Inboard	8	1,489	482	565	13.8
Mid-plane	10	1,538	631	715	
Outboard	12	1,580	777	860	
Beryllium reflector					
Inboard	5	923	425	501	4.68
Mid-plane	6	954	575	650	
Outboard	7	980	722	798	
SiC reflector					
Inboard	5	1,048	436	636	6.18
Mid-plane	7	1,083	586	758	
Outboard	8	1,112	733	932	

[a] First-wall channel diameter is 6.5 mm; Shell channel diameter is 4 mm.

[b] 20% reduction assumed due to non-symmetric surface heat flux (Sec. 8.7).

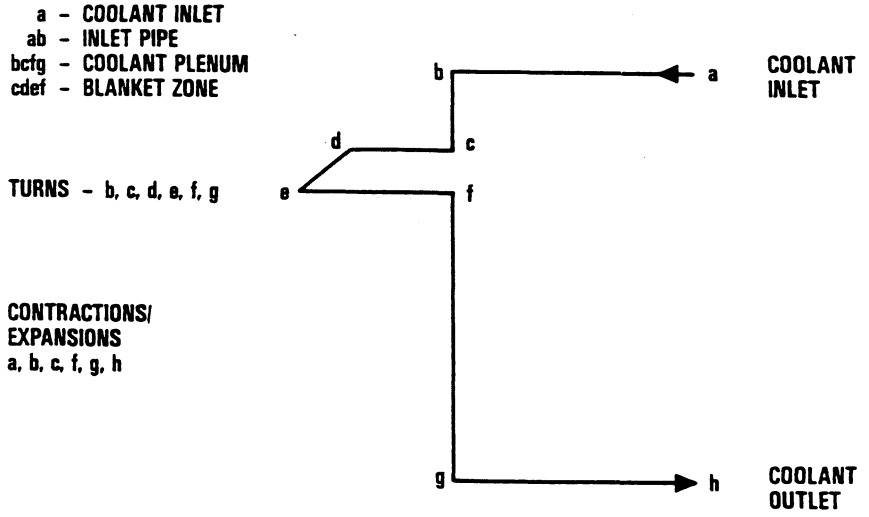

Figure 8.5-1. ARIES-I blanket coolant-routing schematic.

Table 8.5-V.
ARIES-I Outboard Blanket Pressure Drop (Pa)

Designation[a]	Coolant Description	Frictional	Turns	Contraction & Expansion
a	Enters the blanket			297
ab	Inlet pipe	29		
b	Turns into plenum		85	593
bcfg	Plenum flow	2,288		
c	Turns into blanket		87	3,346
d	Turn		87	
e	Turn		87	
cdef	Blanket channel flow	25,000		
f	Turns into plenum		87	9,839
g	Turns into outlet pipe		133	436
gh	Outlet pipe		45	
h	Exits the blanket			872
	Total[b]	27,362	566	15,383

[a]Coolant path locations as given in Fig. 8.5-1.
[b]Total blanket pressure drop is 43.31 kPa.

liquids, gels, alloys, ceramics, *etc.* A heterogeneous system comprises two or more constituent elements: one is the continuous medium and the remainder are discontinuous media. In foamed glass, the continuous medium is glass and the discontinuous medium is a gas. In a packed-bed discontinuous system, the continuous medium is a fluid and there may be one or more discontinuous media of solid materials. A heterogeneous system may also have more than two different materials, leading to a multiphase system. Again, the solid discontinuous medium may have particles of different sizes leading to binary or ternary beds.

The blanket of ARIES-I is a packed bed with spherical particles. The continuous phase is He gas. In the multiplier and reflector zones, the discontinuous phase comprises binary Be spheres with 1- and 0.1-mm diameters. In the breeder zone, the discontinuous phase comprises binary solid spheres of the breeder material, Li_2ZrO_3 (0.1-mm diam), and Be (1-mm diam). Therefore, the multiplier and reflector zones are binary, two-phase packed beds and the breeder zone is a binary, three-phase packed bed. The packing factors are about 0.6 for beds with single spheres and about 0.8 ($\simeq 0.6 + 0.6 \times 0.4$) for binary beds.

The effective thermal conductivity of a packed bed depends upon many variables and is not easy to analyze completely. Among the variables are: (1) thermophysical properties of all of the phases, (2) packing factor, (3) size and shape of the solid particles, (4) pressure and temperature, (5) the nature of contact of the solid particles, (6) presence of oxide layer, (7) the nature of solid surface, *etc.* Large amounts of theoretical, numerical, and experimental data are available for the determination of effective thermal conductivity of a heterogeneous medium. However, work is continuing because further improvement and refinement of these analyses are necessary. The purpose of this section is to find the best possible estimate for the effective thermal conductivities of the packed-bed blanket zones for ARIES-I by reviewing the existing literature.

8.5.2.1. Available work

Work on effective thermal conductivity of a heterogeneous medium dates back to the 1880s [104, 105] and an excellent review of work in this area is provided by Nozad *et al.* [106]. The effective thermal conductivity, k_{eff}, of a porous medium is given by [107]

$$k_{eff} = k_s (1 - P) , \tag{8.5-1}$$

where k_s is the thermal conductivity of the solid and P is its porosity. Hamilton [108, 109] provided a theoretical expression for k_{eff} for a multiphase mixture:

$$k_{eff} = k_c \left[1 - \sum_{i=1}^{m} \frac{P_i (n_i - 1)(k_c - k_i)}{k_i + (n_i - 1)k_c}\right] \left[1 + \sum_{i=1}^{m} \frac{P_i (k_c - k_i)}{k_i + (n_i - 1)k_c}\right]^{-1}, \quad (8.5\text{-}2)$$

where k_c is the thermal conductivity of the continuous phase, k_i is the thermal conductivity, P_i is the porosity, and n_i is the shape factor of the particles. The subscript i signifies the ith phase. The shape factor is given by

$$n = \frac{3}{\Psi}, \quad (8.5\text{-}3)$$

where Ψ is the sphericity of the solid particle. The shape factor is equal to 1 for a sphere and is defined as the ratio of the surface area of a sphere of volume equal to that of a particle to the surface area of the particle.

There are studies where an analytical solution from a simplified model is derived and then modified to account for other effects such as pressure, temperature, radiation, oxide layer, contact, *etc.* [110, 111]. For a cubic-packed model of spherical particles, Hall and Martin [111], provided the following equation for the effective thermal conductivity:

$$\frac{k_{eff}}{k_g} = \frac{\pi}{2} \frac{\delta - 1 - ln\delta}{(\delta - 1)^2} + 1 - \frac{\pi}{4}. \quad (8.5\text{-}4)$$

This equation accounts for conduction only through the solid and gas. The gas conductivity is k_g and δ is the ratio of solid-to-gas thermal conductivities. Their modified equation to account for low pressure and radiation effects is

$$\frac{k_{eff}}{k_g} = \frac{\pi}{2} \left\{ \frac{1 - \lambda}{\delta(1 - \lambda) - 1} - \frac{1 + m}{[\delta(1 - \lambda) - 1]^2} ln \left[\frac{\delta(1 + \lambda m) + m}{(1 + \delta\lambda)(1 + m)}\right]\right\} + \left(1 - \frac{\pi}{4}\right)(1 - \lambda), \quad (8.5\text{-}5)$$

where

$$\lambda = \frac{4\, d_p\, \sigma\, T^3}{k_g\, [(2/\epsilon) - 1]}. \quad (8.5\text{-}6)$$

In these two equations, $m = g/d_p$, σ is the Stefan-Boltzmann constant, d_p is the particle diameter, ϵ is the emissivity of the solid, T is the gas temperature, and $g/2$ is the

temperature jump distance. Accounting for the Knudsen effect, the effective thermal conductivity of a gas between two parallel plates separated by a distance l is given by

$$k_g^{eff} = \frac{k_g}{1 + g/l} . \tag{8.5-7}$$

Ades and Peddicord [112] conducted numerical and experimental studies of binary and ternary packed beds with spherical particles. A schematic diagram of a ternary bed is reproduced from Ref. [112] in Fig. 8.5-2. They found a factor of about 2 increase in effective thermal conductivity from a single sphere to a binary bed.

Heat transfer in multiphase systems has also been analyzed theoretically, using volume averaging method, by Nozad *et al.* [106], Batchelor and O'Brien [113], Hadely [114], and Shonnard and Whitaker [115], among others. Figure 8.5-3 shows Nozad's result and comparison with experimental data.

Reference [113] obtained solutions for the effective bed thermal conductivity in closed forms by inner and outer expansions of the volume-averaged equations. The inner expansion solution corresponds to the point contact and the outer expansion solution to good contact between the solid particles. The inner expansion solution is given by

$$\frac{k_{eff}}{k_g} = 4\, ln\left(\frac{k_s}{k_g}\right) - 11 . \tag{8.5-8}$$

Equation (8.5-8) and the numerical solution of Ref. [106] are very close in the range $k_s/k_g = 100$ to 1000 and also represent the experimental data well. The comparison between Eq. (8.5-8) and the numerical solution in Ref. [106] is shown in Fig. 8.5-4 from Ref. [115].

Abdou *et al.* [116] performed bed conductance experiments with binary mixtures of Aℓ and Cu with He and N_2 as the fill-gases. Adnani *et al.* [117] have done 2-D numerical modeling for effective bed conductivity with the capacity to incorporate contact and surface roughness effects.

8.5.2.2. Effective bed conductivities for ARIES-I blanket

The effective thermal conductivity of a gas in a small gap in given by Eq. (8.5-7). The temperature jump distance, $g/2$, is given by [118]

$$g = 4\frac{2-\alpha}{\alpha}\frac{\gamma}{1+\gamma}\frac{1}{Pr}\lambda , \tag{8.5-9}$$

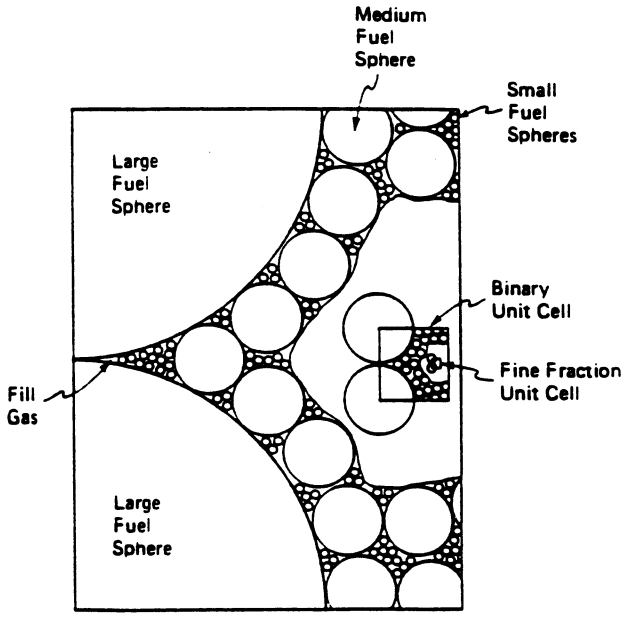

Figure 8.5-2. A schematic of a packed bed with spherical solids of different diameters [112].

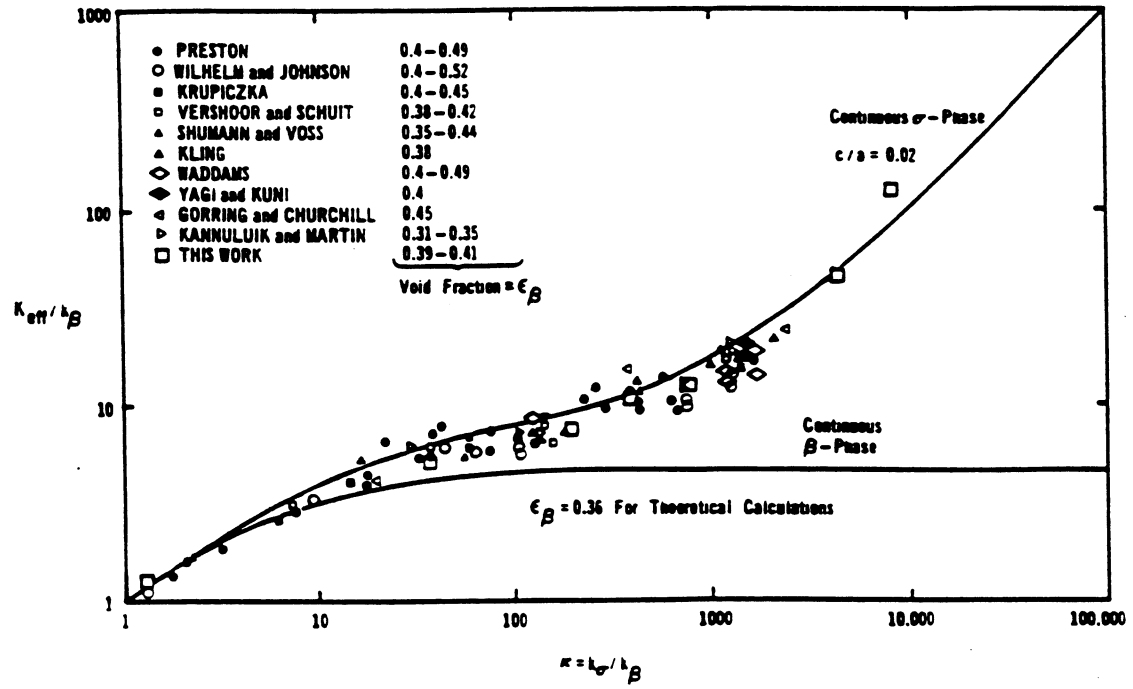

Figure 8.5-3. Verification of the numerical solution of Ref. [106] by experimental data.

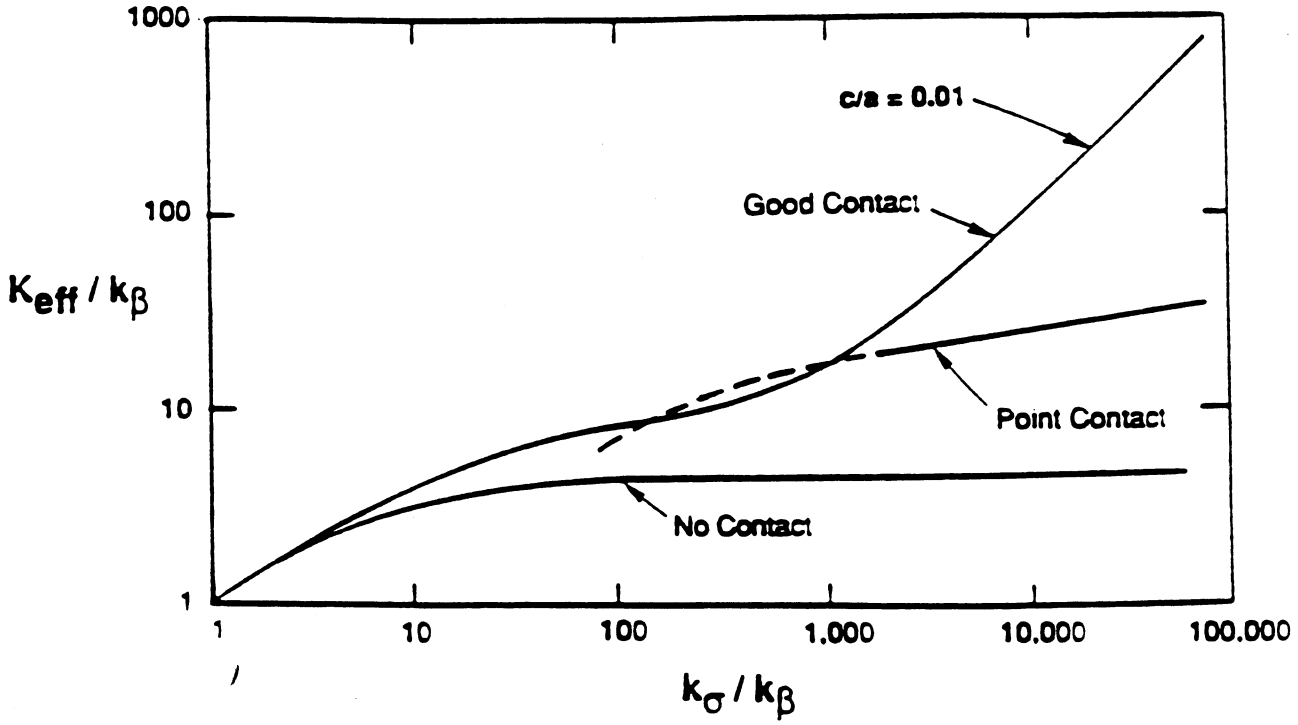

Figure 8.5-4. Comparison of inner expansion solution of Ref. [113] and the numerical solution of Ref. [106] (from Ref. [115]).

where α is thermal accommodation coefficient, γ is the ratio of specific heats, Pr is the gas Prandtl number, and λ is the mean free path of the gas molecules at the gas temperature and pressure. Knudsen domain is assumed for $l \leq 100\lambda$. The mean free path is a function of temperature and pressure and is given by

$$\lambda = \frac{3}{4}\frac{1}{N\pi}\frac{1}{d_m^2} = \lambda_o \frac{T}{T_o}\frac{p_o}{p}, \tag{8.5-10}$$

where N is number of molecules per unit volume, d_m is the molecular diameter, and p_o and T_o are, respectively, the standard atmospheric pressure and temperature at which the mean free path, λ_o, is equal to $8.89 \times 10^{-27}\ d_m^2$ (m). The thermal accommodation coefficient, α, is a function of temperature, pressure, fill-gas properties, wall material, and surface conditions. The coefficient α is determined experimentally, but precise measurement of α is difficult and has been done only for a few solid-gas combinations. Ullman *et al.* [119] measured α to be about 0.3 at 500 K and about 0.1 at 1200 K for He with 316 SS and with UO_2.

Figure 8.5-5 shows the variation of k_g^{eff} with pressure for He fill-gas in the ARIES-I blanket where the gap size is taken to be equal to the diameter of the smaller spherical

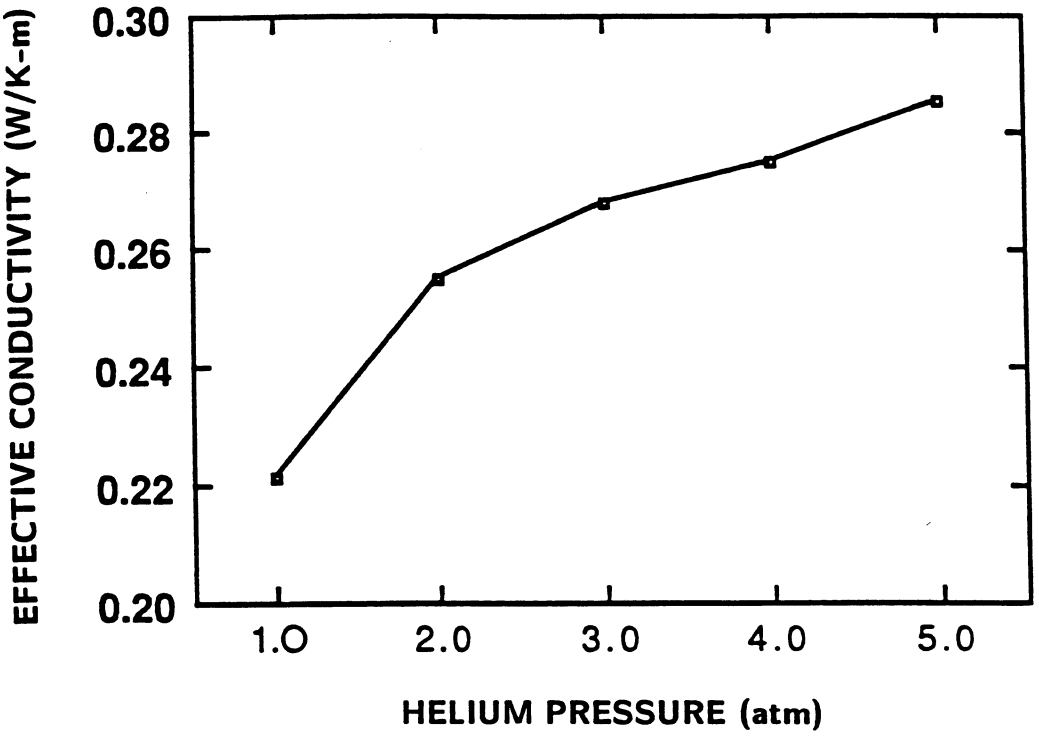

Figure 8.5-5. Variation of effective thermal conductivity of He with pressure.

particle (0.1 mm). It is seen that the effective gas conductivity becomes close to 0.3 at a pressure of 4 atm. At this pressure and the expected temperature of the ARIES-I blanket, the gap size is more than 100 times the mean free path. There is no experimental data available for the thermal accommodation coefficient for the He-Be and He-Li_2ZrO_3 combinations. Therefore, it is decided to avoid the Knudsen effect on the effective fill-gas thermal conductivity by raising the purge-gas pressure to 4 atm.

Assuming 10% porosity in Be and Li_2ZrO_3, their effective thermal conductivities at the ARIES-I blanket temperature become, respectively, 81 and 1.2 W/K-m, according to Eq. (8.5-1). Radiation and oxide layer effects are assumed to be negligible. Among the various equations and correlations for effective bed conductivity, Eq. (8.5-8) and the numerical solution in Ref. [106] are supported by a wide variety of experimental data and over a wide range of solid-to-gas conductivity ratios. In the multiplier zone, the conductivity ratio is $81/0.3 = 270$. Equation (8.5-8) is valid for $k_s/k_g = 100$ to 1000. This equation is used, therefore, to estimate the effective bed conductivity with single-size solids. This number is then modified to obtain the effective bed conductivities for the multiplier and breeder zones, which are, respectively, two- and three-phase binary beds.

Multiplier zone. Equation (8.5-8) gives effective thermal conductivity of 3.4 W/K-m for single-size solids. For a binary bed, the factor by which the effective bed conductivity increases is about 2 from Ref. [112] and 2.3 from Eq. (8.5-2) for packing factors of 0.6 and 0.8. Therefore, the effective thermal conductivity of the multiplier zone of the ARIES-I blanket is taken to be 7.3 W/K-m (3.4 × 2.15).

Breeder zone. In the binary bed of the breeder zone, the smaller spherical solids are Li_2ZrO_3 (k = 1.2 W/K-m) instead of Be (k = 81 W/K-m). According to Eq. (8.5-2), the resulting reduction in the effective conductivity is about 37%. Therefore, the effective bed conductivity for the breeder zone of the ARIES-I blanket is taken to be 4.6 W/K-m (7.3 × 0.63).

At the bed wall, the number of contact points is larger than that inside the bed. This should increase the effective conductivity adjacent to the wall. However, the gap size becomes nearly half of that inside the bed, thus making the Knudsen effect more pronounced near the wall. The general belief is that these two opposing effects cancel each other. Therefore, the effective thermal conductivity at the packed-bed wall is taken equal to that inside the bed.

8.6. TRITIUM PURGE-FLOW DESIGN

The reference ARIES-I blanket design uses SiC composite as the structural material, 10-MPa helium as the coolant, Li_2ZrO_3 as the solid tritium breeder, and beryllium-metal sphere-pac pellets as the neutron multiplier. The blanket is segmented toroidally into 32 inboard and 32 outboard poloidal modules. Each poloidal module comprises 17 nested, U-shaped SiC-composite shells, as shown in Figs. 8.1-5 and 8.1-6. The sphere-pac solid-breeder and Be neutron-multiplier mixture is located between the shells. The tritium systems, including estimates of blanket tritium inventory, are described in Sec. 6.

For the extraction of bred tritium, a separate helium purge stream that flows through the breeder sphere-pac material is used. The helium purge-stream pressure is 0.4 MPa. This pressure was selected in order to maintain adequate effective thermal conductivity of the sphere-pac bed. Details of this analysis are reported in Sec. 8.5.2. To form the purge flow stream, 1-mm-thick porous SiC-fiber sheets are located on each side of the tube-bank-geometry coolant-channel shell. The triangular shaped channel that is formed between adjacent cylindrical coolant tubes and the porous sheet becomes the blanket-zone purge-flow channel. This allows the shortest flow path (*i.e.*, half of the individual

breeder-zone thickness) for the bred tritium to migrate before it reaches a purge flow channel. These purge flow channels are then connected to the purge-flow collection channels at the end of the blanket shells. The purge stream then flows vertically to the external tritium purge-flow collection pipes.

For the reference design, the Li_2ZrO_3 breeder and Be multiplier sphere-pac is composed of 1- and 0.1-mm-diameter pellets. If these sizes lead to excessive purge-flow pressure drop, a combination of larger size pellets (1.5- and 0.2-mm-diam) will be acceptable. With the larger size pellets, a pellet packing fraction of about 80% can be maintained [120]. Similarly, with the large 1.5-mm pellet, the minimum channel dimension (1.1 cm) to pellet diameter ratio is larger than 7. Therefore, the problem of bridging during the filling operation of the sphere-pac into the breeder zone is not expected. Details of the purge flow design, including the purge-channel detailed configuration, pressure drop, and the extraction loop, need further study.

8.7. HEAT TRANSFER IN PLASMA-FACING COMPONENTS

8.7.1. Uniqueness of Heat Transfer in Plasma-Facing Components

A coolant channel in plasma-facing components, such as the first wall and divertor plates, has circumferentially varying surface heat flux because the plasma radiation is incident only on the plasma-facing side of the channel. Convective heat transfer with nonuniform heat flux varies significantly from the uniform heat-flux case because the temperature field becomes asymmetric under the influence of nonuniform heat flux. As a result, the thermal entry length, and the Nusselt number (Nu) in the entry region and in the steady state are greatly affected. Therefore, thermal-hydraulic designs of the plasma-facing components must account for the effects of nonuniformity of the surface heat flux.

Work in this area for fusion applications is rather limited and continues. Hasan [121] performed analytical work to investigate the effects of nonuniformity of surface heat flux and fully developed laminar velocity profiles on heat transfer in a circular tube and on the thermal-hydraulic design of fusion reactors. This work also investigated the effects of a transverse magnetic field on liquid-metal heat transfer by assuming a power velocity profile to approximate the flattening of the velocity profile. The first analytical and semi-analytical work in convective heat transfer with nonuniform heat flux was done by Reynolds [122, 123]. Analytical solutions are, however, difficult or impossible in many

practical cases. Hasan and Kunugi have recently obtained numerical solutions to various laminar and turbulent heat-transfer problems for the plasma-facing components of fusion reactors (see Refs. [124–127]).

In ARIES-I, the primary coolant is helium flowing through circular tubes in the first wall and divertor plates. The flow is non-magnetohydrodynamic and turbulent. This section presents the results of the numerical analysis in order to provide heat transfer guidelines for the thermal-hydraulic designs of the first wall and divertor plates for the ARIES-I reactor.

8.7.2. Formulation and Solution of the Problem

The physical details of the heat transfer problem in the plasma-facing components using circular coolant tubes are shown in Fig. 8.7-1. The uniform radiation heat flux incident on a coolant tube is denoted by q''_R, d is the tube diameter, and L is the axial length. The radiation heat flux is taken to be uniform along the axis of the tube. A cylindrical (r, θ, z) coordinate system is used in the numerical solution.

8.7.2.1. Governing equations

The transient, three-dimensional (3-D) energy equation can be written as

$$\frac{\partial(\rho\, c_p\, T)}{\partial t} + \nabla \cdot (\rho\, c_p\, \mathbf{u}\, T) \;=\; \nabla^2(kT) - \nabla \cdot (\langle \rho\, c_p\, \mathbf{u}\, T' \rangle) + Q\,, \qquad (8.7\text{-}1)$$

where Q is the volumetric heat source, t is time, T and T' are, respectively, temperature and temperature fluctuation, u_j are the velocity components (u, v, w), x_j are the spatial coordinates (r, θ, z), k, ρ, and c_p are, respectively, the thermal conductivity, density, and specific heat capacity, and $\langle \cdot \rangle$ denotes ensemble average of the bracketed quantity. The second term on the right-hand side of Eq. (8.7-1) is the turbulent heat-flux term. For laminar flow, this term is dropped. To close Eq. (8.7-1) for turbulent flow, a turbulence model is needed.

The boundary conditions for Eq. (8.7-1) are

$$q''(\theta) \;=\; \begin{cases} A + B\cos\theta, & -\dfrac{\pi}{2} \le \theta \le \dfrac{\pi}{2} \\ A, & \dfrac{\pi}{2} \le \theta \le \dfrac{3\pi}{2} \end{cases}, \qquad (8.7\text{-}2)$$

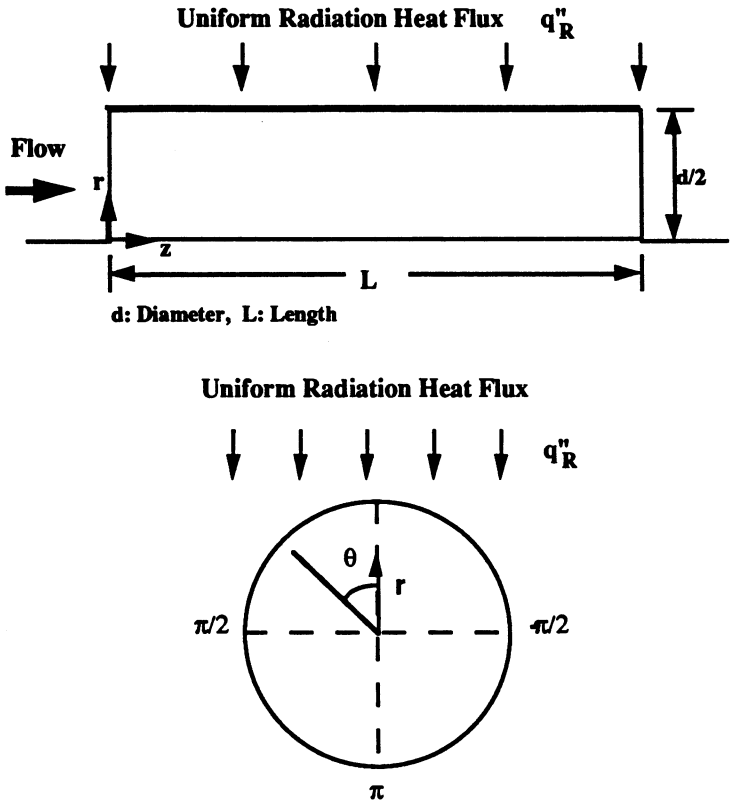

Figure 8.7-1. A circular coolant tube in a plasma-facing component showing the geometry and heat flux conditions (the solution domain is $0 \leq \theta \leq \pi$).

where $A \sim Q_{NH}\delta$, $B = q''_R$, and Q_{NH} is the volumetric nuclear heat generation in the tube wall. The ratio B/A gives a measure of the peakedness or nonuniformity of the surface heat flux. There are symmetry conditions at $\theta = 0$ and $\theta = \pi$ (Fig. 8.7-1) so the problem is solved in half of the tube ($0 \leq \theta \leq \pi$).

The conventional definition of Nu is used. Since the surface heat flux varies circumferentially, Nu also varies along θ. In the entry region, Nu varies axially. Therefore,

$$Nu(\theta, z) = \frac{q''(\theta)\, d}{k\,[T_w(\theta, z) - T_b(z)]}, \tag{8.7-3}$$

where $T_w(\theta, z)$ is the coolant/wall interface temperature and $T_b(z)$ is the fluid bulk temperature.

8.7.2.2. Turbulence model

In general, many turbulent quantities need to be known. If both flow and temperature fields are analyzed, some turbulence model is necessary to close the system of equations. Usually a two-equation turbulence modeling (the so-called "$k - \epsilon$ model of turbulence" [128]), which is coupled with the momentum equations, is used. The interest here, however, is to solve the energy equation only. Therefore, empirical correlations for turbulent velocity and eddy diffusivity profiles are used instead of solving the Navier-Stokes and turbulence transport equations.

Velocity profile. The well-known 1/7th-power law of velocity [129] is assumed for the turbulent velocity profile and is given by

$$w^+ = 8.65(y^+)^{1/7}, \tag{8.7-4}$$

where $w^+ = w/w^*$ and $y^+ = yw^*/\nu$, w is the velocity component along z-direction, w^* is the friction velocity, y is the distance from the wall, and ν is the kinematic viscosity.

Eddy diffusivity. The Reichardt formula [130] is used for eddy diffusivity:

$$\frac{\nu^*}{\nu} = \frac{\kappa y^+}{3}\left[0.5 + \left(\frac{r}{R}\right)^2\right]\left(1 + \frac{r}{R}\right), \tag{8.7-5}$$

where κ is the Karman constant ($= 0.42$) and R is the radius of the tube. This correlation is valid for $y^+ \geq 50$. Figure 8.7-2 shows the velocity and eddy diffusivity profiles for $Re = 10^5$ which is used for turbulent flow calculations.

8.7.2.3. Numerical solution

Equation (8.7-1) is discretized by a finite/control volume method in the computer code, CONDIF, which was developed as a transient 3-D fluid flow and heat transfer solver [131, 132]. This code uses the Euler implicit method for time advancing and the central differencing scheme for the spatial derivatives. The convective terms are approximated by a CONDIF method [133]. All variables are defined on the well-known staggered grid system. All of the calculations presented here are done using the grid size $10 \times 15 \times 50$ in the r, θ, z coordinates.

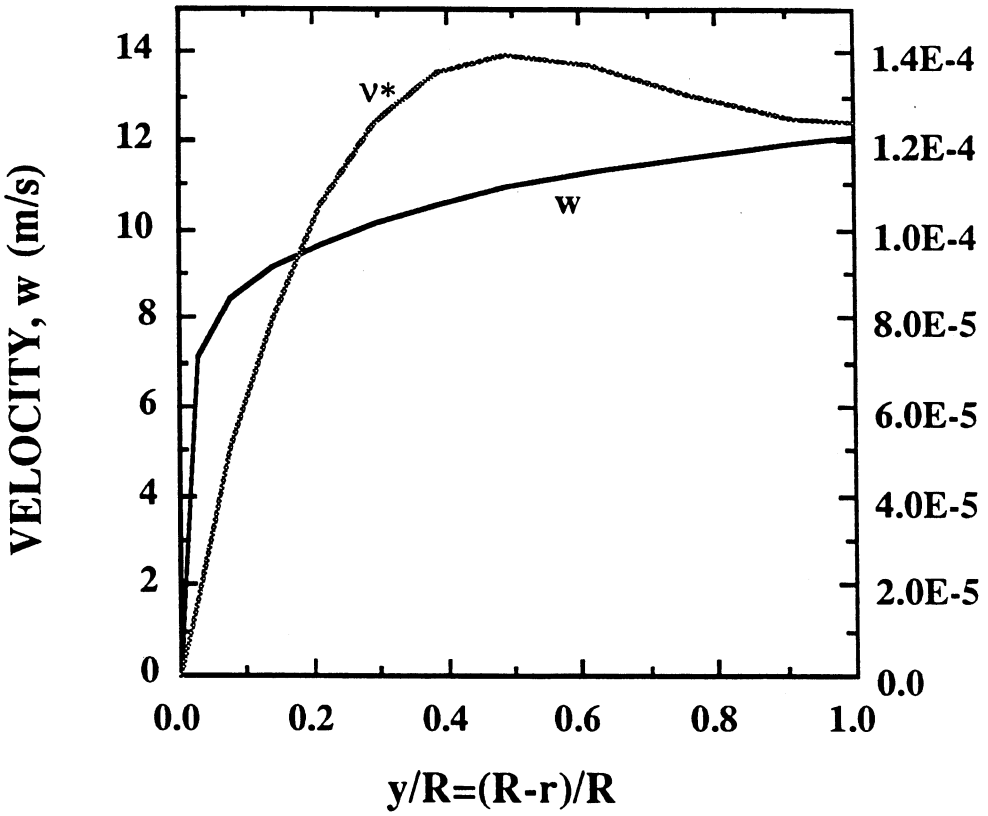

Figure 8.7-2. Turbulent velocity and eddy diffusivity profiles for $Re = 10^5$.

The CONDIF code is used directly for the case of laminar flow. However, the code needed to be improved for turbulent-flow heat-transfer calculations because a wall temperature is determined by using an equivalent eddy-diffusivity model applied to the nearest wall computational cell [134]. The equivalent eddy diffusivity, ν^{**}, is defined as

$$\nu^{**} = \frac{\mu y^+}{Pr_t \left[C_\mu^{1/4} Re_v \left(\frac{Pr}{Pr_t} - 1 \right) + \frac{1}{\kappa} ln(E y^+) \right]}, \tag{8.7-6}$$

where Re_v is the Reynolds number based on a viscous sub-layer thickness, y_v, Pr and Pr_t are, respectively, molecular and turbulent Prandtl numbers, C_μ and E are turbulence model constants, and μ is the molecular viscosity coefficient. In Eq. (8.7-6), $Pr_t = 0.9$ and $Re_v = 20$ have been used because these values are confirmed to be valid for many turbulent equilibrium flows [135].

8.7.3. Results and Discussion

Heat transfer calculations have been performed for both laminar and turbulent flows for the entry region as well as for steady state. The results are obtained for laminar flow with liquid lithium and for turbulent flow with both liquid lithium and helium. For laminar flow, the Nu is independent of coolant property and flow velocity. Helium pressure is assumed to be 10 MPa, which is the pressure in the ARIES-I design.

Figure 8.7-3 shows the axial variation of Nu at $\theta = 0$ for laminar and turbulent flows. The coolant is liquid lithium. The ratio B/A is the parameter. This figure shows that Nu at the point of maximum heat flux (at $\theta = 0$) is significantly reduced as the nonuniformity of heat flux (ratio B/A) is increased. This is true both in the entry region and in the steady state.

Figure 8.7-4 shows the Nu for turbulent flow in the entry region for helium with conditions similar to those for ARIES-I. Nusselt numbers are shown for uniform heat flux ($B/A = 0$) and for $B/A = 1$ (Nu is at $\theta = 0$). Compared with the turbulent flow Nu for liquid lithium, helium gives much higher values. However, the relative reduction of Nu at the point of maximum heat flux in the case of nonuniform heat flux is of similar magnitude.

The variation of Nu (at $\theta = 0$) with B/A is shown in Fig. 8.7-5 for Poiseuille, slug, and turbulent flows. It can be seen that Nu decreases rapidly with B/A and levels off beyond $B/A = 10$. This reduction is substantial: 38%, 62%, and 37%, respectively, for Poiseuille, slug, and turbulent flows.

The effect of nonuniformity of heat flux on the entry length is shown in Fig. 8.7-6 for laminar and turbulent flows. The curves marked by 1% give the axial length from the entrance at which the Nu differs from its steady-state value by 1%; similarly for the curves marked by 10%. These results show that the entry length is greatly increased by the nonuniformity of the surface heat flux. For laminar flow in a circular tube, the entry length can be increased by a factor of 2.4. For turbulent flow, the corresponding factor is 3.5.

8.7.4. Conclusions

Heat transfer in the plasma-facing components of a fusion reactor has been analyzed numerically to investigate the effects of nonuniformity of surface heat flux on a coolant channel in these components. Analysis has been performed for circular-tube coolant

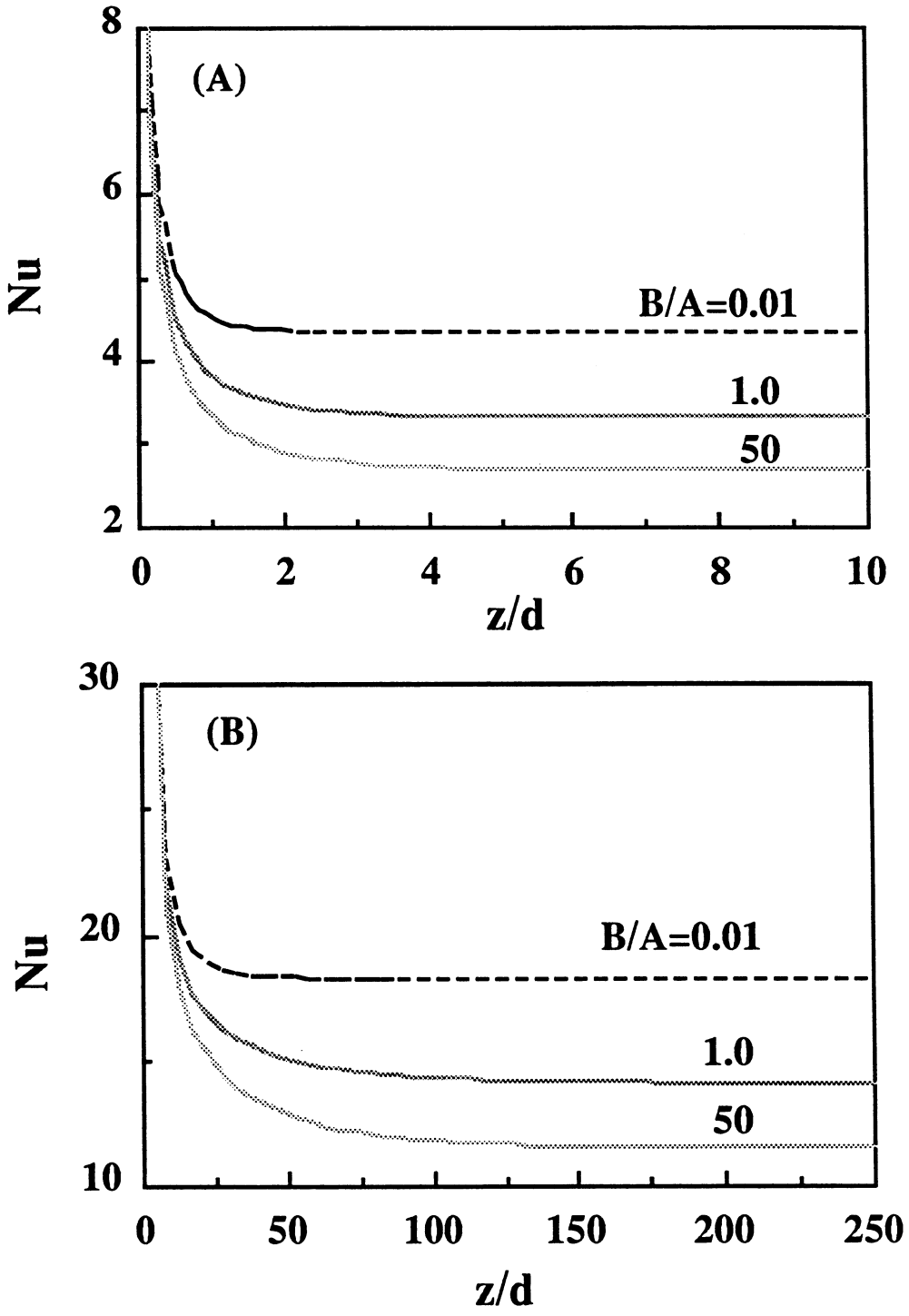

Figure 8.7-3. Nusselt number (at $\theta = 0$) in the entry region for (A) laminar flow and (B) turbulent flow (the coolant is liquid lithium).

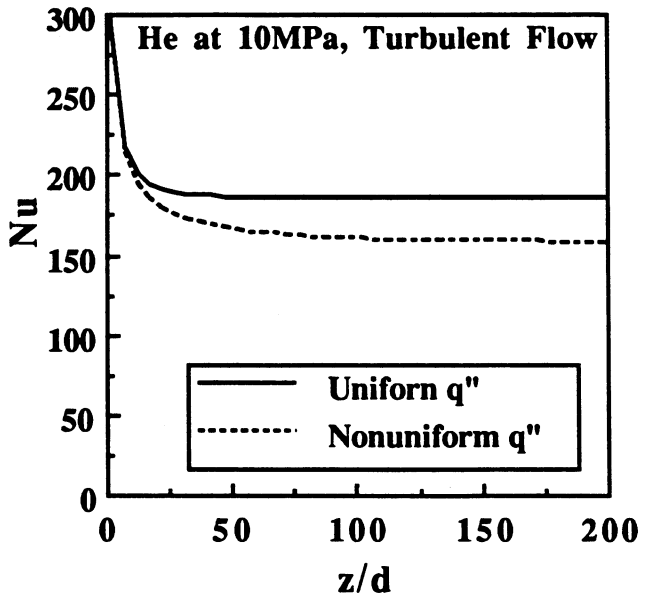

Figure 8.7-4. Nusselt number (at $\theta = 0$ for $B/A = 1$) in the entry region for turbulent flow for $B/A = 0$ and 1 (the coolant is helium at 10 MPa).

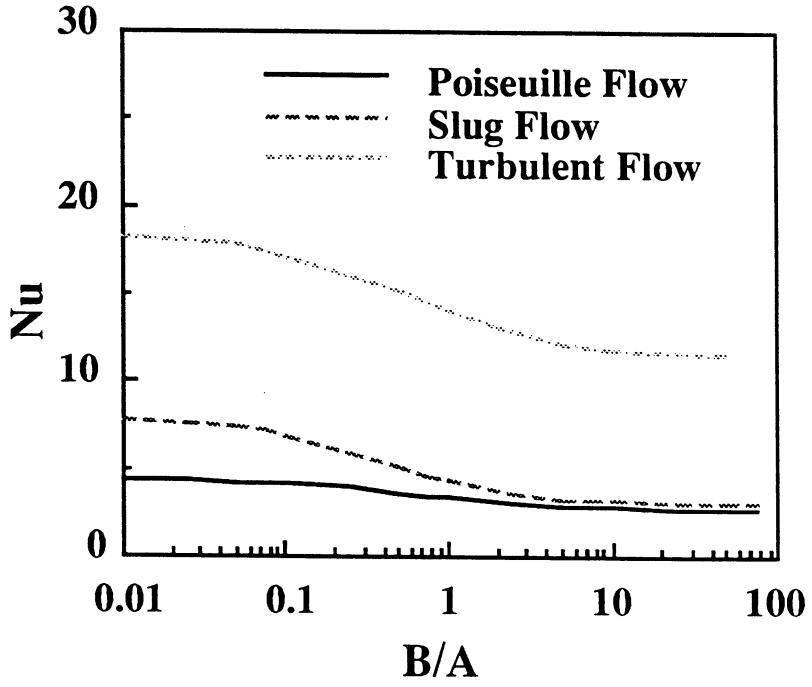

Figure 8.7-5. Variation of steady-state Nu (at $\theta = 0$) with the nonuniformity of surface heat flux as measured by the ratio B/A.

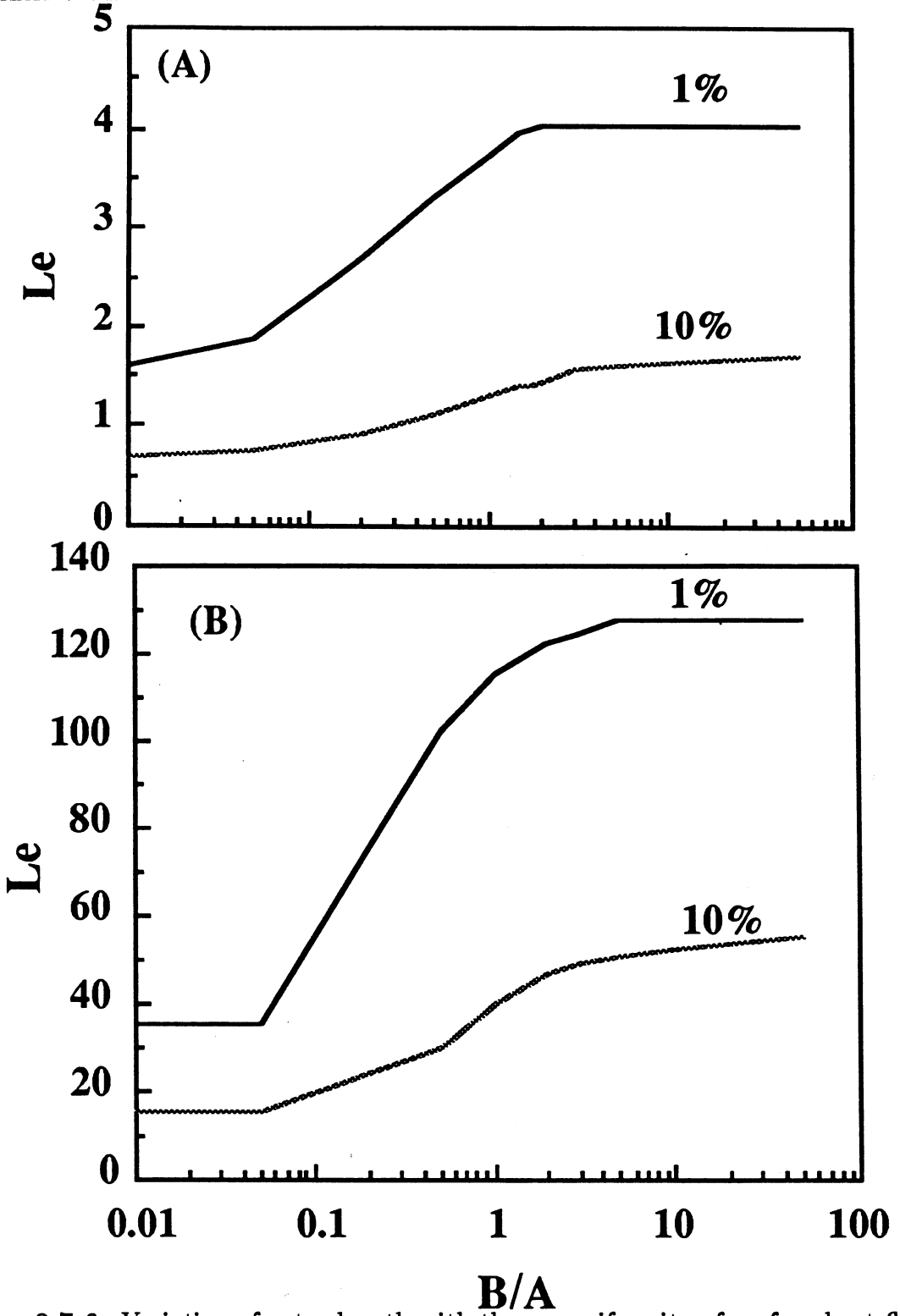

Figure 8.7-6. Variation of entry length with the nonuniformity of surface heat flux for (A) laminar and (B) turbulent flows.

channels (as used in the ARIES-I design). The effects of the nonuniformity of surface heat flux on the Nusselt number and entry length are significant and must be taken into account for an accurate and safe thermal-hydraulic design of the plasma-facing components.

The maximum wall temperature of a coolant channel in the plasma-facing components will occur at the point of maximum heat flux. The nonuniformity of surface heat flux reduces Nu at the same location. For both laminar and turbulent flows, this reduction in Nu can be up to 37% compared with uniform heat flux, thus increasing the film temperature drop by the same amount. The Nu is also reduced in the entry region. However, the entry length is increased by 2.4 and 3.5, respectively, for laminar and turbulent flows.

In light of this study, it is recommended that the steady-state Nu for the thermal-hydraulic design of the first wall and divertor plates of ARIES-I be reduced by 37% from the uniform heat-flux value. Otherwise, the maximum coolant-channel temperature will be underestimated. Even with the resulting increase of entry length, it is short relative to the total length of the coolant channel. Therefore, advantage cannot be taken of higher Nu in the entry region. A possible exception to this conclusion would be in the divertor plate design where the inlet is at the point of peak divertor heat flux.

Further work in this area is necessary and is continuing. Because of the approximate nature of turbulence heat-transfer model, experimental study is necessary.

8.8. SUMMARY AND CONCLUSIONS

A comparative study of blanket concepts was performed for the ARIES-I reactor. After a preliminary investigation of many possible blanket concepts, three were selected for further study: (1) FLiBe molten-salt-cooled, low-pressure with vanadium alloy structure; (2) gas-carried, particulate-cooled, low-pressure with ceramic composite structure; and (3) helium-cooled, high-pressure with ceramic composite structure. The tritium breeders considered in the gas cooled systems included Li_2O, $LiA\ell O_2$, Li_4SiO_4, and Li_2C_2; the neutron-multiplier material was Be.

Silicon-carbide composite was selected as the structural material for the ARIES-I blanket and shield because of its low-activation features. Beryllium metal was determined to be the neutron multiplier because of the high (n,2n) performance capability. Solid-breeder materials, particularly Li_2O, Li_4SiO_4, and Li_2ZrO_3, were considered as breeder

material candidates for the ARIES-I blanket because of generally favorable thermal and physical properties, good tritium recovery, high-temperature capability, and low waste-disposal concern.

Although SiC composites are still in their developmental infancy, this study indicates that they are a viable material for future fusion-reactor applications. The fabricability of SiC composite materials has been demonstrated, and the thermal and structural response has shown that an SiC-composite first wall for ARIES-I does not exceed the maximum-allowable design criteria of temperature and stress; at the same time, SiC composite materials can tolerate temperatures well above those allowable for conventional metallic alloys.

The reference ARIES-I blanket design uses SiC composite as the structural material, 10-MPa helium as the coolant, Li_2ZrO_3 as the solid tritium breeder, and beryllium-metal sphere-pac pellets as the neutron multiplier. The blanket is segmented toroidally into 32 inboard and 32 outboard poloidal modules. Each poloidal module comprises 17 nested, U-shaped SiC-composite shells, as shown in Figs. 8.1-5 and 8.1-6. The sphere-pac solid-breeder and Be neutron-multiplier mixture is located between the shells. Thermal hydraulic and structural analyses indicate that all components operate below their respective temperature and stress limits. Using the nested-shell configuration, the total blanket-loop pumping power is reasonable at 19 MWe.

Lithium zirconate was chosen as the reference solid breeder mainly because of its favorable stability behavior under neutron irradiation [8]. Unfortunately, extensive isotopic tailoring of Zr is needed to reduce activation and afterheat. It should be noted that even after extensive isotopic tailoring, the off-site dose from a severe accident in the ARIES-I reactor is still dominated by Zr. This provides an important incentive to develop low-activation solid breeders such as Li_4SiO_4. Lithium oxide is also a viable low-activation solid breeder if the generation and migration of LiOT at high temperature ($\sim$1000 °C) can be controlled. Again, this can only be addressed by high-temperature, *in-situ*, tritium-extraction irradiation experiments. In all of the designs considered, including the selected reference nested-shell design, Be neutron-multiplication material will be needed in order to obtain a high blanket-energy multiplication and adequate tritium breeding (it may be possible to achieve adequate tritium breeding ratio with Li_2O breeder and SiC structure without any Be multiplier).

Considering only the thermal-hydraulic aspects, the nested-shell configuration is an excellent design and no critical issue has been identified. However, in order to provide further confidence in the design, the effective thermal conductivity of the solid-breeder/Be-multiplier sphere-pac materials will need to be measured. Experimental study of the

change in properties of the sphere-pac materials packed in slab geometry after operation to high neutron fluence is also needed.

The critical issues in the ARIES-I nested-shell blanket design that will need to be addressed are:

- Developing the SiC-composite material, including vacuum leak-tight SiC-composite components, and a technique of brazing nested shells onto the back coolant plenum;
- Developing the techniques necessary for joining SiC composite to metal for the transition from (ceramic) blanket pipes to the (metallic) heat exchanger pipes;
- Isotopic tailoring of Zr in Li_2ZrO_3, with acceptable tailoring cost;
- Studying the irradiation properties of SiC composite, breeder, and Be neutron-multiplier materials, and the sphere-pac fuel form;
- Studying tritium generation and migration under high burnup for SiC composite, breeder, and Be neutron-multiplier materials.

There are critical issues for other design options that, once addressed, could potentially improve the ARIES-I blanket performance. These issues are:

- Improving the tritium inventory and breeder behavior of Li_4SiO_4 under high burnup could affect the selection of the solid breeder for the reference design. Using Li_4SiO_4 instead of Li_2ZrO_3 would reduce afterheat and the radioactive inventory, and would improve the waste disposal rating.
- Mitigating the Li_4SiO_4 and SiC particulate erosion on SiC composites would lead to a re-evaluation of using a gas and solid-particulate mixture as the blanket coolant, possibly yielding a viable low-pressure gas-cooled design.
- Controlling the corrosive behavior of FLiBe on vanadium alloy would lead to the re-evaluation of FLiBe as the blanket coolant and breeder and thereby avoid the uncertainties associated with solid-breeder materials.

REFERENCES

[1] D. L. Smith, G. D. Morgan, M. A. Abdou, *et al.*, "Blanket Comparison and Selection Study—Final Report," Argonne National Laboratory report ANL/FPP-84-1 (1984).

[2] F. Najmabadi, R. W. Conn, R. A. Krakowski, K. R. Schultz, D. Steiner, and the TITAN Research Group, "The TITAN Reversed-Field-Pinch Reactor Study—The Final Report," University of California Los Angeles, General Atomics, Los Alamos National Laboratory, and Rensselaer Polytechnic Institute, University of California Los Angeles report UCLA PPG-1200 (1990); also, F. Najmabadi, R. W. Conn, R. A. Krakowski, K. R. Schultz, D. Steiner, and the TITAN Research Group, "Engineering and Physics of High-Power-Density, Compact, Reversed-Field-Pinch Fusion Reactors: The TITAN Study," *Proc. 15th Symp. Fusion Technol. (SOFT),* Utrecht, the Netherlands (Sept. 1988), *Fusion Technology 88*, A. M. Van Ingen, A. Nijsen-Vis, H. T. Klippel, Eds., North-Holland, Amsterdam (1989) p. 1779.

[3] D. K. Sze, "IPFR, Interpretated Pool Fusion Reactor Concept," *Fusion Technol.* **10** (1986) 875.

[4] C. P. C. Wong, E. T. Cheng, R. L. Creedon, *et al.*, "Blanket Design for the ARIES-I Tokamak Reactor," *Proc. IEEE 13th Symp. on Fusion Eng.,* Knoxville, TN (Oct. 1989), IEEE No. 89CH2820-9, IEEE, Piscataway, NJ (1990) p. 1035.

[5] C. P. C. Wong and M. Z. Hasan, "Thermal-Hydraulic Design of A Solid Particulate Fusion Reactor Blanket," *Proc. 10th Int. Conf. Stru. Mech. in Reactor Technol. (SMiRT-10),* Anahiem, CA (Aug. 1989) N19.

[6] D. C. Schluderberg *et al.*, "Gaseous Suspensions—A New Reactor Coolant," *Nucleonics* **19** (1961) 8.

[7] D. Krucoff, "Armor Dust-Fueled Reactor," *Nucleonics* **17** (1959).

[8] C. E. Johnson, K. R. Kummerer, and E. Roth, "Ceramic Breeder Materials," *Proc. 3th Int. Conf. Fusion Reactor Mater.*, Karlsruhe, Germany (Oct. 1987), *J. Nucl. Mater.* **155-157** (1988) 188.

[9] G. R. Hopkins, and E. Cheng, "Low Activation Fusion Rationale," *Nucl. Technol./Fusion* **4** (1983) 528.

[10] J. A. DiCarlo, Deputy Chief, Ceramics Branch, Material Division, National Aeronautics and Space Administration, Lewis Research Center, OH, private communication (April 1989).

[11] O. Koyama, Materials Science Department, University of Tokyo, Japan, private communication (Dec. 1989).

[12] R. Kamo, "Ceramics for Advanced Heat Engines," *High Technology Ceramics*, P. Vincenzini, Ed., Elsevier, Amsterdam (1987) p. 2473.

[13] M. J. Bennet, M. R. Houlton, and R. W. M. Hawes, "The Improvement by a CVD Silica Coating of the Oxidation Behaviour of a 20% Cr/25% Ni Niobium Stabilized Stainless Steel in Carbon Dioxide," *Corrosion Sci.* **22** (1982) 111.

[14] B. A. Thiele and K. Koizlig, "Neutron Irradiation of Ceramics for Fusion Application in a Material Test Reactor and Spallation Neutron Source (Pre-irradiation Characteristics and Test Layout)," *High Technology Ceramics*, P. Vincenzini, Ed., Elsevier, Amsterdam (1987) p. 2971.

[15] D. Stinton, A. J. Caputo, and R. A. Lowden, "Synthesis of Fiber-Reinforced SiC Composites by Chemical Vapor Infiltration," *Am. Ceram. Bull.* **65** (1986) 347.

[16] P. J. Lamicq, G. A. Bernhardt, M. M. Dauchier, and J. G. Mace, "SiC/SiC Composite Ceramics," *Am. Ceram. Bull.* **65** (1986) 336.

[17] D. J. Pysher, K. C. Goretta, R. S. Hodder, Jr., and R. E. Tressler, "Strengths of Ceramic Fibers at Elevated Temperatures," *J. Am. Ceram. Soc.* **72** (1989) 284.

[18] H. Fukunaga and K. Goda, "The Tensile Characteristics of Coreless and Carbon-Core Silicon Carbide Fibers Exposed to Some Environments," *Proc. Int. Symp. on Composite Mater. and Structures*, Beijing, China (1986) 56.

[19] F. W. Clinard, Jr., G. F. Hurley, R. A. Youngman, and L. W. Hobbs, "The Effect of Elevated-Temperature Neutron Irradiation on Fracture Toughness of Ceramics," *J. Nucl. Mater.* **133&134** (1985) 701.

[20] G. K. Bansal and A. Heuer "Precipitation in Non-Stochiometric Magnesium Aluminate Spinel," *Philos. Mag.* **29** (1974) 709.

[21] D. J. Green, P. S. Nicholson, and J. D. Embury, "Crack Shape Studies in Brittle Porous Materials," *J. Mater. Sci.* **12** (1977) 987.

[22] A. G. Evans, "The Strength of Brittle Materials Containing Second Phase Dispersions," *Philos. Mag.* **26** (1972) 1327.

[23] K. T. Faber and A. G. Evans, "Crack Deflection Processes—I. Theory," *Acta Metall.* **31** (1983) 565.

[24] K. T. Faber and A. G. Evans, "Crack Deflection Processes—II. Experiment," *Acta Metall.* **31** (1983) 577.

[25] D. J. Green and P. S. Nicholson, "Fracture of Brittle Particulate Composites," *Fracture Mechanics of Ceramics*, R. C. Bradt, D. P. H. Hasselman, and F. F. Lange, Eds., Plenum Press, New York (1978) Vol. 4, p. 945.

[26] J. S. Nadeau and J. I. Dickson, "Effects of Internal Stresses Due to a Dispersed Phase on the Fracture Toughness of Glass," *J. Am. Ceram. Soc.* **63** (1980) 517.

[27] R. J. Price, "Properties of SiC for Nuclear Fuel Particle Coatings," *Nucl. Technol.* **35** (1977) 321.

[28] G. P. Pells, "Ceramic Materials for Fusion Reactor Applications," *J. Nucl. Mater.* **122&123** (1984) 1338.

[29] R. B. Mattews, "Irradiation Damage in Reaction-Bonded Silicon Carbide," *J. Nucl. Mater.* **51** (1974) 203.

[30] R. B. Mattews, "Radiation Damage in Silicon Carbide and Graphite for Fusion Reactor First Wall Applications," *J. Nucl. Mater.* **83** (1979) 313.

[31] T. Suzuki, T. Yano, T. Maruyama, T. Iseki, and T. Mori, "Effects of Sintering Aids on the Length Change of Neutron Irradiated SiC Ceramics During Annealing at High Temperature," *J. Nucl. Mater.* **165** (1989) 247.

[32] T. Iseki, T. Maruyama, T. Yano, and T. Suzuki, "Effects of Neutron Irradiation and Subsequent Annealing on Strength and Toughness of SiC Ceramics," *J. Nucl. Mater.* **170** (1990) 95.

[33] R. J. Price and G. R. Hopkins, "Flexural Strength of Proof-Tested and Neutron Irradiated Silicon Carbide," *J. Nucl. Mater.* **108&109** (1982) 732.

[34] T. Yano, T. Suzuki, T. Maruyama, and T. Iseki, "Microstructure and Annealing Behavior of Heavily Neutron-Irradiated β-SiC," *J. Nucl. Mater.* **155-157** (1988) 311.

[35] T. Suzuki, T. Maruyama, and T. Iseki, "Recovery Behavior in Neutron Irradiated β-SiC," *J. Nucl. Mater.* **149** (1987) 334.

[36] R. P. Thorne, V. C. Howard, and B. Hope, "Radiation-Induced Changes in Porous Cubic Silicon Carbide," *Proc. Br. Ceram. Soc. Nucl. and Eng. Ceram.*, Harwell, United Kingdom (Oct. 1965), British Ceramic Society, Stoke-on-Trent (1967) 449.

[37] R. S. Wilks,"Neutron-Induced Damage in BeO, $A\ell_2O_3$ and MgO—A Review," *J. Nucl. Mater.* **26** (1968) 137.

[38] R. J. Price, "Neutron Irradiation-Induced Voids in Beta Silicon Carbide," *J. Nucl. Mater.* **48** (1973) 47.

[39] T. Suzuki and T. Iseki, "The Influence of Thermal Vacancies on Helium-Induced Volume Swelling in Silicon Carbide," *J. Nucl. Mater.* **170** (1990) 113.

[40] K. Hojou and K. Izui, "Structural Changes Induced by Helium Ion Irradiation in Silicon Carbide Crystals," *J. Nucl. Mater.* **133&134** (1985) 709.

[41] S. D. Harrison and J. C. Corelli, "Microstructure of Neutron Irradiation-Induced Defects in Sintered and Siliconized SiC," *J. Nucl. Mater.* **122&123** (1984) 833.

[42] A. M. Carey, F. J. Pineau, C. W. Lee, and J. C. Corelli, "Radiation Response of Reaction-Bonded and Sintered SiC: Effects of Boron Isotopes," *J. Nucl. Mater.* **103&104** (1981) 789.

[43] K. Hojou, S. Furuno, H. Otsu, K. Izui, and T. Tsulamoto, "In-Situ Observation of the Dynamic Process of Structural Changes During Ion Irradiation and Its Application to SiC and TiC Crystals," *Proc. 3th Int. Conf. Fusion Reactor Mater.*, Karlsruhe, Germany (Oct. 1987), *J. Nucl. Mater.* **155-157** (1988) p. 298.

[44] T. Stoto and L. Zuppiroli, "Irradiation Damage in Boron Carbide: Point Defects, Clusters, and Helium Bubbles," *High Technology Ceramics,* P. Vincenzini, Ed., Elsevier, Amsterdam (1987) p. 2959.

[45] C. A. Parker, L. W. Hobbs, K. C. Russel, and F. W. Clinard, Jr., "Damage Structures in Fast Neutron Irradiated Magnesium Aluminate and Electron Irradiated Aluminum Oxynitride Spines," *J. Nucl. Mater.* **133&134** (1985) 741.

[46] N. Igata, A. Kohyama, and H. Tezuka, "Characteristics of PCS-Type SiC/Aℓ Composites After Thermal Exposure and Neutron Irradiation," *Proc. 3rd Japan-U.S.*

Conf. on Composite Mater., Tokyo, Japan (June 1986), Japan Society for Composite Materials, Tokyo, Japan (1986) 505.

[47] K. Okamura, T. Matzsuzawa, M. Soto, Y. Higashiguchi, and S. Morozumi, "Effects of Neutron Irradiation on SiC Fiber," *J. Nucl. Mater.* **133&134** (1985) 705.

[48] E. Cheng, General Atomics, San Diego, CA, private communication (Feb. 1989).

[49] "Ceramic Matrix Composites: Preliminary Engineering Data," Du Pont Co., Magnolia Run, Willmington, DE, Composite Division commercial literature H-10627-4 (1989).

[50] C. C. Chamis, "Simplified Composite Micromechanics Equations for Mechanical, Thermal, and Moisture-Related Properties," *Engineer's Guide to Composite Materials*, American Society for Metals, Metals Park, OH (1987) p. 3-8.

[51] J. J. Kibler, "Composite Laminate Analysis System (CLASS)," Materials Sciences Corp., ASM International, Metals Park, OH (1987).

[52] C. W. Lee, F. J. Pineau, and J. C. Corelli, "Thermal Properties of Neutron-Irradiated SiC; Effects of Boron Doping," *J. Nucl. Mater.* **108&109** (1982) 678.

[53] G. R. Hopkins and J. Chin, "SiC/SiC Composite," General Atomics report GA-A18295 (1985); also, E. Fitzer and R. Gadow, "Fiber-Reinforced Silicon Carbide," *J. Am. Ceram. Bull.* **65** (1986) 326.

[54] "Capability Brochure," Atlantic Research Corp., a Subsidiary of the Sequa Corp., Virginia Propulsion Division, 5945 Wellington Rd., Gainsville, VA (1989).

[55] R. W. Davidge, "Mechanical Properties and Engineering Design with Ceramics," *Ceramics in Advanced Energy Technologies*, H. Krockel, M. Merz, and O. Van der Biest, Eds., Reidel Publishing (1984) p. 98.

[56] P. Fang, C. Ko, and M. Koczak, "Stress-Strain-Time Relationship of SiC Yarns," *Proc. Int. Symp. Composite Mater. and Structures*, Beijing, China (1986) 38.

[57] H. Fukuda, T. W. Chou, and K. Kawata, "Probabilistic Approach on the Strength of Fibrous Composites," *Composite Materials*, K. Kawata and T. Akasaka, Eds., Japan Society for Composite Materials, Tokyo (1981) p. 181.

[58] R. J. Price, "Thermal Conductivity of Neutron-Irradiated Pyrolytic β-Silicon Carbide," *J. Nucl. Mater.* **46** (1973) 268.

[59] H. Bhatt, K. Y. Donaldson, and D. P. H. Hasselman, "Role of Thermal Barrier Resistance in the Effective Thermal Diffusivity/Conductivity of SiC Fiber Reinforced Reaction Bonded Silicon Nitride," to be published in *J. Am. Ceram. Soc.*

[60] H. Tawil, L. D. Bensten, S. Baskaran, and D. P. H. Hasselman, "Thermal Diffusivity of Chemically Vapour Deposited Silicon Carbide Reinforced with Silicon Carbide or Carbon Fibers," *J. Mater. Sci.* **20** (1985) 3201.

[61] R. J. Price, "Effects of Fast Neutron Irradiation of Pyrolytic Silicon Carbide," *J. Nucl. Mater.* **33** (1969) 17.

[62] L. Snead, Rennselear Polytechnic Institute, private communication (Jan. 1990).

[63] J. Roth and J. Bohdansky, "Erosion of Carbon Due to Bombardment with Energetic Ions at Temperatures up to 2000 K," *J. Nucl. Mater.* **111&112** (1982) 775.

[64] J. Bohdansky and J. Roth, "Light Ion Sputtering of Low Z Materials in the Temperature Range 20–1000 °C," *J. Nucl. Mater.* **122&123** (1984) 1417.

[65] F. Porz, G. Grathwohl, and F. Thummler, "SiC as a Structural Material in the Plasma Chamber of Nuclear Fusion Reactors," *Mater. Sci. Eng.* **71** (1985) 273.

[66] S. Miyagawa, Y. Ato, and Y. Miyagawa, "Implantation Profiles of Low-Energy Helium in Silicon Carbide," *Jpn. J. App. Phys.* **23** (1984) 1380.

[67] S. Miyagawa, Y. Ato, and Y. Miyagawa, "Surface Structure of Silicon Carbide Irradiated with Helium Ions with Monoenergetic and Continuous Energy Distributions," *J. Appl. Phys.* **53** (1982) 8697.

[68] S. Nagata, S. Yamaguchi, and Y. Fujino, "Retention of Hydrogen Implanted into SiC Crystals," *J. Nucl. Mater.* **128&129** (1984) 760.

[69] "ASME Boiler and Pressure Vessel Code, 1977 Code Cases-Nuclear Components," 1977 Edition, Case N-47 (1977) 1592-10.

[70] R. Bustamante, Product Development Engineer, Amercom Inc., Chatsworth, CA, private communication (Feb. 1989).

[71] A. N. Scoville, P. Reagan, and F. N. Huffman, "Evaluation of SiC Matrix Composites for High Temperature Applications," *Adv. Mater. & Manufacturing Processes* **3** (1988) 643.

[72] W. Tarasen, BP Chemical Corp. (HITCO), Gardena, CA, private communication (Feb. 1990).

[73] Fred Mazandarany, General Electric Materials R&D, Schnectedy, NY, private communication (Dec. 1988).

[74] "Capability Bulletin," Amercom Inc., Chatsworth, CA (1989).

[75] J. Chin, Ceramics Division, General Atomics, San Diego, CA, private communication (Nov. 1989).

[76] The U.S. ITER Nuclear Group, "ITER Shield and Blanket Work Package Report," Argonne National Laboratory report ANL/FPP/88-1 (1988).

[77] F. C. Kracek, *J. Phys. Chem.* **34** (1930) 2645.

[78] O. P. Preuss, "Historical Perspective on the Uses and Health Risks of Beryllium," *Fusion Technol.* **8** (1985) 1137.

[79] T. J. McCarville, D. H. Berwald, W. Wolfer, F. J. Fulton, J. D. Lee, *et al.*, "Technical Issues for Beryllium Use in Fusion Blanket Applications," Lawrence Livermore National Laboratory report UCID-20319 (1985).

[80] *Beryllium Science and Technology,* D. Webster and G. J. London, Eds., Plenum Press, New York (1979).

[81] J. B. Rich and G. P. Walters, "The Effects of Heating Neutron Irradiated Beryllium," *J. Nucl. Mater.* **1** (1959) 96.

[82] C. E. Ells and E. C. W. Perryman, "Effects of Neutron-Induced Gas Formation on Beryllium," *J. Nucl. Mater.* **1** (1959) 73.

[83] J. R. Weir, "The Effects of High-Temperature Reactor Irradiation on Some Physical and Mechanical Properties of Beryllium," *Proc. Int. Conf. on Metallurgy of Beryllium*, London, United Kingdom (Oct. 1961), Institute of Metals, London (1962) 362.

[84] J. B. Rich and R. S. Barnes, "Mechanical Properties of Some Highly Irradiated Beryllium," *J. Nucl. Mater.* **4** (1961) 287.

[85] J. D. Lee, R. W. Moir, W. L. Barr, R. S. Devoto, G. W. Hamilton, *et al.*, "Feasibility Study of a Fission-Suppressed Tandem-Mirror Hybrid Reactor," Lawrence Livermore Laboratory report UCID-19327 (1982).

[86] M. O. Tucker and R. J. White, "The Geometry in Interlinked Grain Edge Porosity," *Res Mechanica* **1** (1980) 21.

[87] L. G. Miller and J. M. Beeston, "Radiation Damage Experiments and Lifetime Estimates for Beryllium Components in Fusion Systems," *Fusion Technol.* **8** (1985) 1152.

[88] J. M. Beeston, "Gas Release and Compression Properties in Beryllium Irradiated at 600 and 700 °C," *Effects of Irradiation on Structural Metals*, ASTM STP 426 American Society for Testing and Materials, Richland, WA (1967) p. 135.

[89] N. P. Pinto, J. P. Denny, and G. J. London, "Isostatic Pressing of Beryllium Powder," *Light Metals*, American Institute of Mining Engineers, New York (1974) p. 356.

[90] G. M. D'Hospital and P. Fortesque, "On the Choice of Gas Coolant for Nuclear Reactors," General Atomics report GA-7344 (1966).

[91] G. M. D'Hospital and G. R. Hopkins, "Gas Cooling for Fusion Reactor Blankets," General Atomics report GA-10004 (1970).

[92] Kato and Kagawa, Nippon Carbon Corp., Japan, private communication (July 1990).

[93] G. Vogel, Dow Chemical Co., Midland, MI, private communication (July 1990).

[94] A. Fresco, Lanxide/Du Pont Inc., Willmington, DE, private communication (July 1990).

[95] P. Delles, Coors Ceramic Co., Golden, CO, private communication (July 1990).

[96] M. Jost, Eagle Pitcher Boron, Quapaw, OK, private communication (July 1990).

[97] *Chemical Marketing Reporter*, Schnell Publishing Co., New York (1989) Vol. 236.

[98] F. P. Magin, III, Hercules Inc., Magna, UT, private communication (June 1990).

[99] M. Dalle Donne, Ulrich Fischer, and Marko Kuchle, "A Helium-Cooled, Poloidal Blanket with Ceramic Breeder and Beryllium Multiplier for the Next European Torus," *Nucl. Technol.* **71** (1985) 15.

[100] G. Desalvo and J. A. Swanson, "ANSYS—Engineering Analysis System," Version 4.1, Swanson Analysis Systems Inc., Houston, PA (1979).

[101] E. T. Cheng, "Radioactivity Aspects of Fusion Reactors," *Fusion Eng. Des.* **10** (1989) 231.

[102] E. T. Cheng and K. R. Schultz, "Activation Evaluation of Fusion Solid Breeder Materials," *Proc. IEEE 13th Symp. on Fusion Eng.,* Knoxville, TN (Oct. 1989), IEEE No. 89CH2820-9, IEEE, Piscataway, NJ (1990) p. 1116.

[103] M. Huggenberger, "Helium-Cooled, Solid Breeder Blanket Design for a Tokamak Fusion Reactor," General Atomics report GA-A16308 (1981).

[104] J. C. Maxwell, *Treatise on Electricity and Magnetism*, 2nd ed., Clarendon Press, Oxford (1881).

[105] L. Lorenz, *Ann. Phys. Chem.* **11** (1880) 70.

[106] I. Nozad, R. G. Carbonell, and S. Whitaker, "Heat Conduction in Multiphase Systems—I: Theory and Experiment for Two-Phase Systems," *Chem. Eng. Sci.* **40** (1985) 843.

[107] J. Francl and W. D. Kingery, "Thermal Conductivity: IX, Experimental Investigation of Effect of Porosity on Thermal Conductivity," *J. Am. Ceram. Soc.* **37** (1954) 99.

[108] R. L. Hamilton, "Thermal Conductivity of Two-Phase Materials," Ph.D. thesis, University of Oklahoma (1960).

[109] R. L. Hamilton and O. K. Crosser, "Thermal Conductivity of Heterogeneous Two-Component Systems," *Ind. Eng. Chem.* **1** (1963) 187.

[110] R. Bauer and E. U. Schlünder, "Effective Radial Thermal Conductivity of Packings in Gas Flow, Part II, Thermal Conductivity of the Packing Fraction without Gas Flow," *Int. Chem. Eng.* **18** (1978) 189.

[111] R. O. A. Hall and D. G. Martin, "The Thermal Conductivity of Powder Beds, a Model, Some Measurements on UO_2 Vibro-Compacted Microspheres, and Their Correlation," *J. Nucl. Mater.* **101** (1981) 172.

[112] M. J. Ades and K. L. Peddicord, "A Model for Effective Thermal Conductivity of Unrestructured Sphere-Pac Fuel," *Nucl. Sci. Eng.* **81** (1982) 540.

[113] G. K. Batchelor and R. W. O'Brien, "Thermal or Electrical Conduction Through a Granular Material," *Proc. R. Soc. London* **A355** (1977) 313.

[114] G. R. Hadley, "Thermal Conductivity of Packed Metal Powders," *Int. J. Heat Mass Transfer* **29** (1986) 909.

[115] D. R. Shonnard and S. Whitaker, "The Effective Thermal Conductivity for a Point-Contact Porous Medium: An Experimental Study," *Int. J. Heat Mass Transfer* **32** (1989) 503.

[116] M. A. Abdou, A. R. Raffray, Z. R. Gorbis, *et al.*, "A Helium-Cooled Solid Breeder Concept for the Tritium-Producing Blanket of the International Thermonuclear Experimental Reactor," *Fusion Technol.* **15** (1989) 166.

[117] P. Adnani, A. R. Raffray, M. A. Abdou, and I. Catton, "Modeling of Effective Thermal Conductivity for a Packed Bed," University of California Los Angeles report UCLA-FNT-29 (1989).

[118] E. H. Kennard, *Kinetic Theory of Gases,* 1st ed., McGraw-Hill, New York (1938) p. 311.

[119] A. Ullman, R. Acharya, D. R. Olander, *et al.*, "Thermal Accommodation Coefficients of Inert Gases on Stainless Steel and UO_2," *J. Nucl. Mater.* **51** (1974) 277.

[120] P. Gierszewski, Canadian Fusion Fuel Technology Program (CFFTP), Toronto, Canada, private communication (Feb. 1990).

[121] M. Z. Hasan, "Effects of Nonuniform Surface Heat Flux and Uniform Volumetric Heating on Blanket Design for Fusion Reactors," *Fusion Technol.* **16** (1989) 44.

[122] W. C. Reynolds, "Heat Transfer to Fully Developed Laminar Flow in Circular Tube with Arbitrary Circumferential Heat Flux," *Trans. ASME* (May 1960) 108.

[123] W. C. Reynolds, "Turbulent Heat Transfer in a Circular Tube with Variable Circumferential Heat Flux," *Int. J. Heat and Mass Transfer* **6** (1963) 445.

[124] T. Kunugi and M. Z. Hasan, "Heat Transfer with Nonuniform Surface Heat Flux and Thermal-Hydraulic Design of the Plasma-Facing Components of Fusion Reactors," *Proc. 16th Symp. Fusion Technology (SOFT),* London, United Kingdom (Sept. 1990), *Fusion Technology 90*, A. M. Van Ingen, A. Nijsen-Vis, H. T. Klippel, Eds., North-Holland, Amsterdam (1991) p. 973.

[125] T. Kunugi and M. Z. Hasan, "Entry-Length Effect on the Thermal-Hydraulic Design of Plasma-Facing Components of Fusion Reactors—Part I: Non-MHD Flow," *Proc. of ANS 9th Top. Mtg. Technol. of Fusion Energy,* Oak Brook, IL (Oct. 1990), *Fusion Technol.* **19** (1991) 1024.

[126] M. Z. Hasan and T. Kunugi, "Entry-Length Effect on the Thermal-Hydraulic Design of Plasma-Facing Components of Fusion Reactors—Part II: MHD Flow," *Proc. of ANS 9th Top. Mtg. Technol. of Fusion Energy,* Oak Brook, IL (Oct. 1990), *Fusion Technol.* **19** (1991) 1030.

[127] M. Z. Hasan and T. Kunugi, "Liquid-Metal Heat Transfer for the First Wall and Limiter/Divertor Plates of Fusion Reactors," *Proc. 27th Nat. Heat Transfer Conf.*, Minneapolis, MI (July 1991), *Heat Transfer—Minneapolis 1991*, S. B. Yilmay, B. G. Volintine, Eds., American Institute of Chemical Engineers Series 283, Vol. 87, New York (1991) p. 67.

[128] B. E. Launder and D. B. Spalding, *Mathematical Models of Turbulence, Lecture 5*, Academic Press, New York (1972).

[129] H. Schlichting, *Boundary-Layer Theory*, McGraw-Hill, New York (1987) p. 10.

[130] B. S. Petukhov, "Heat Transfer and Friction in Turbulent Pipe Flow With Variable Physical Properties," *Advances in Heat Transfer,* T. F. Irvine, Jr., J. P. Hartnett, Eds., Academic Press, New York (1970) Vol. 6, p. 503.

[131] T. Kunugi, M. Yokokawa, and T. Chiba, "Vectorization of a Three-Dimensional Thermal-Hydraulic Analysis Code, STREAM," Japan Atomic Energy Research Institute report JAERI-M 88-119 (1988) (in Japanese).

[132] T. Kunugi and M. Yokokawa, "Numerical Analysis for Lid-Driven Cavity Flow Using a CONDIF Approach," *Trans. JSME B* **55** (1989) 1823 (in Japanese).

[133] A. K. Runchal, "CONDIF: A Modified Central-Difference Scheme with Unconditional Stability and Very Low Numerical Diffusion," *Proc. Int. Heat Transfer Conf.* (1986) 403.

[134] T. Kunugi and H. Kawamura, *Transport Phenomena in Turbulent Flows: Theory, Experiment and Numerical Simulation*, M. Hirata and N. Kasagi, Eds., Hemisphere, New York (1988) p. 593.

[135] W. Rodi, *Turbulence Models and Their Applications in Hydraulics—A State of the Art Review,* International Association for Hydraulic Research, The Netherlands (1984).